2010-07-08

A New Eulerian-Based Double Continuity Model for Predicting the Evolution of Pair Correlation Statistics under Large Plastic Deformations

Sadegh Ahmadi
Brigham Young University - Provo

A New Eulerian-Based Double Continuity Model for Predicting the Evolution of Pair Correlation Statistics under Large Plastic Deformations

Sadegh Ahmadi

A thesis submitted to the faculty of
Brigham Young University
in partial fulfillment of the requirements for the degree of

Doctor of Philosophy

Brent L. Adams, Chair
David T. Fullwood
Carl D. Sorensen
Tracy W. Nelson
Branton J. Campbell

Department of Mechanical Engineering

Brigham Young University

August 2010

ABSTRACT

A New Eulerian-Based Double Continuity Model for Predicting the

Evolution of Pair Correlation Statistics under

Large Plastic Deformations

Sadegh Ahmadi

Department of Mechanical Engineering

Doctor of Philosophy

A new model using a double-continuity relation for predicting the evolution of pair-correlation functions (PCFs) is presented. The proposed model was developed using statistical continuum theory and is employed to predict the viscoplastic behavior of polycrystalline materials. This model was built based upon the continuity relations and a double divergence law that guarantees the conservation of both orientation and mass; and also satisfies the field equations (equilibrium, constitutive, and compatibility) at every point of the polycrystalline material throughout the deformation process. In the presented model, motion of particles in the real space and rotation of crystallographic orientations in the Euler angle space is monitored using an iterative process assuming that all the amount of deformation is applied uniformly without taking into account the localization effects. To study the accuracy of the proposed model, a commercially pure nickel material was rolled to different amounts of cold work. Texture and statistical analyses of the experimental and simulated microstructures were carried out. For the texture analysis, pole figures, ODF sections, and volume fractions of some ideal orientations of cold-rolling were studied. For the statistical analysis, pair correlation functions (PCFs) were employed and the correlations (auto- and anti-correlations) between ideal orientations and also the coherence length were studied. Simulated results captured from the implementation of the new model are in good agreement with the experimental ones at low and medium rolling deformations (0 to 50% rolling reductions); however, at large levels of deformations (above 70% reductions), because of the formation of cell blocks and relevant inhomogeneity, the occurrence of ideal orientations and their correlation properties in the experimental microstructure is affected by grain subdivision phenomena. This causes distortions in the shape of crystallographic grains at large rolling reductions, and accordingly we observe larger errors in comparison of simulated and experimental microstructures.

Keywords: Sadegh Ahmadi, microstructure, crystal plasticity, continuum mechanics, viscoplastic material, simulation

ACKNOWLEDGMENTS

"He who does not express gratitude to people does not express gratitude to God either"
Prophet Mohammad

Writing this dissertation and doing the necessary research for it was a collective endeavor. Many people have contributed to my success directly or indirectly. They may not expect to be mentioned here; however, I only name a few in order to keep the tradition of gratitude alive. I would like to thank all the members of my supervisory committee for all their help. A very special thanks is due to my supervisor, Professor Brent L. Adams, for the professionalism, experience, and immense knowledge that he brought to the team. He has been a source of moral and personal support which no other person could provide. Professor Adams' comprehensive knowledge in this field made me confident that I could explore this topic seriously because he not only would appreciate such an attempt but also would correct me if I err on some points. Also, the contribution of the members of my graduate committee, Professor David T. Fullwood, Carl D. Sorensen, Tracy W. Nelson, and Branton J. Campbell is gratefully acknowledged. Their knowledge and expertise in the field made me more comfortable dealing with this topic. The members of my research group have each in different ways been valuable resources in time and advice during this process. I would like to specially thank Jay Basinger, Stuart Rogers, Oliver Johnson, Josh Katcher, Ribeka Takahashi, C.J. Gardner, and Ali Khosrovani for all their help.

The contributions of my family members to my life and work are beyond my ability to recite. Without their love and labor I could not achieve what I have achieved. To my wife, Fatemeh, belongs the most beautiful praises that I can utter and deepest love of my heart. Her parents, Mohammad and Zahra, were also extremely supportive and helpful and I appreciate everything they have done for us. My parents, Jamshid and Meimanat, devoted themselves to raising me the best they could and I love them dearly.

TABLE OF CONTENTS

LIST OF TABLES

LIST OF FIGURES

NOMENCLATURE

BCC	Body-centered cubic material
DC	Double continuity
EAS	Euler angle space
FCC	Face-centered cubic material
FDM	Finite difference method
FEM	Finite element method
FFT	Fast Fourier transform
FZ	Fundamental zone
FZ_3	Fundamental zone for cubic materials that is three times larger than the ordinary cubic fundamental zone
$FZ_{3C/4}$	Cubic fundamental zone with orthorhombic sample symmetry for rolled materials
GA	Genetic algorithm
HCP	Hexagonal close-packed material
MC	Mass-based continuity
MF	Microstructure function
OC	Orientation-based continuity
ODF	Orientation distribution function
OIM	Orientation image microscopy
PCF	Pair-correlation function
RC	Relaxed constraint
RD	Rolling direction
RDF	Radial distribution Function
SFE	Stacking fault energy
TD	Transverse direction
TIP	Two isotropic phase material
TLVP	Taylor-like viscoplastic model
VF	Volume fraction
$\varphi_1, \Phi, \varphi_2$	Euler angles of the individual orientations
$\dot{\varphi}_1, \dot{\Phi}, \dot{\varphi}_2$	Lattice rotation rate
$g(\varphi_1, \Phi, \varphi_2)$	Orientation at a given Euler space
$\dot{g}(\varphi_1, \Phi, \varphi_2)$	Orientation change at a given Euler space
dg	Invariant volume element in the Euler angle space
$f(g)$	Orientation distribution function of orientation g
$f_2(g, g' \mid r)$	Two-point correlation function of orientations g and g' away by vector r
$\widetilde{f}_2(g, g' \mid r)$	Normalized two-point correlation function of orientations
$M(x, g)$	Microstructure function of orientation g at position x
C	Elastic stiffness tensor
C' or $\widetilde{C}$	Polarized elastic stiffness tensor
M	Plastic compliance tensor
N	Plastic secant modulus tensor
N' or $\widetilde{N}$	Polarized plastic secant modulus

Γ	Green's function
Ω	Region of interest
$\tau^{(s)}$	Resolved shear tensor for slip system s
$\dot{\gamma}^{(s)}$	Slip shear rate for slip system s
$\tau^{*(s)}$	Critical resolved shear stress for slip system s
m	Rate sensitivity parameter
σ	Deviatoric Cauchy stress
D^P	Plastic strain-rate tensor
L	Velocity gradient tensor
L^P	Plastic velocity gradient tensor
W^P	Plastic rotation tensor
W^L	Lattice spin tensor
t	Time
dt	Time step
$v(x)$	Mass velocity vector at position x
$\rho(x)$	Mass density at position x
$w(x,g)$	Orientation velocity vector of orientation g at position x
$\dot{\varpi}$	Lattice rotation vector
D/Dt	Material derivative

1 INTRODUCTION

Polycrystalline materials are aggregates of numerous crystallites or grains of various sizes and shapes. In order to study mechanical and metallurgical properties of polycrystalline materials one needs to know detailed information about the sizes, shapes and placement of these crystallites or grains. A grain in a polycrystalline material, by definition, is an aggregate of neighboring particles having similar crystallographic orientation with respect to the sample coordinate system. Study of the behavior of grains during deformation processes has been a pervasive subject of mechanical and materials sciences. Applying a plastic deformation causes particles of individual grains inside an examined polycrystalline material to move from their preliminary location to a new position in the space of material particles that is called the *real space* or *the mass space*. The deformation process, on the other hand, causes grains of the polycrystalline material to rotate around a specific rotation axis, to change their original orientation, and to take new configurations relative to the sample coordinate system. These changes are not random and involve rotations that are directly related to the crystallography of the deformation. As a consequence, the grains acquire a distinguishing pattern, or texture, which becomes stronger as deformation proceeds. These rotations take place in *the orientation space*, the space that includes all possible rotations of lattice orientation. There are many ways to show the continuous motion (or rotation) of orientations, among which the *Euler angle space (EAS)* (BUNGE 1993) and the Rodrigues vector representations (MORAWIEC and FIELD 1996) are more

common in microstructure simulations. In this research, the Bunge definition of Euler angles is selected as the working space for orientation rotations.

From the discussion above, it can be concluded that for any material point in the material, there are two spaces that should be considered during the evolution process: *the real space* and *the orientation space*. Conservation principles can be used to study the motion of material particles in the real space and lattice orientations in the orientation space. To study the movement of material particles and crystallographic orientations a proper reference system should be selected and these movements are compared based upon the original coordinates. There are two common types of coordinate systems that are used in the literature: the Lagrangian and the Eulerian. The definition of both systems can be found in continuum mechanics textbooks (IRGENS 2008; LAI *et al.* 2009; NAIR 2009; REDDY 2008). Basically, based upon the Lagrangian description of motion, material particles are studied with regard to the coordinate system at the reference configuration (at time zero). In this case, the coordinates are moving with the motion and the body of material can be reshaped (rotated and/or stretched) as the deformation proceeds. On the other hand, based on the Eulerian description, a fixed control volume is considered and the rate of change of any material property, e.g. the mass density or the *orientation distribution function (ODF)*, is studied in a permanent coordinate system. The Lagrangian and Eulerian descriptions can also be applied for studying rotations in the orientation space.

In the literature one can find many FEM models that take the Lagrangian coordinates as the working frame (KALIDINDI and ANAND 1992; KALIDINDI and ANAND 1994; KALIDINDI *et al.* 1992; KUMAR and DAWSON 1998; KUMAR and DAWSON 2009). In most of these models, only the evolution of crystallographic texture has been important and not much care has been devoted to simulate the evolution of shape and structure of deformed grains. In these models the initial

ODF is measured experimentally from the original microstructure, some plasticity-related models are exploited, and the final ODF is predicted by applying the plastic strain gradually. Lagrangian frame models have some benefits and limitations. The most serious limitation of using the Lagrangian system is that the shape and the size of the material volume element may change throughout the deformation process leading to a severely distorted mesh at the end of the process. Our preference here is to use an Eulerian framework to simulate the shape and orientation changes of grains in the microstructure.

The first approach to predict the evolution of the ODF in the Eulerian basis was proposed by Clement and Coulomb (CLEMENT 1982; COULOMB 1979). Their model predicts the texture evolution considering a continuity relation that is valid in the EAS and guarantees the conservation of orientation principle during the microstructure evolution. This continuity relation has been formulated from concepts commonly used in continuum mechanics to observe the rate of change of mass flowing in a continuous medium. Based on Clement's formalism and the continuity equation in the orientation space, many studies have investigated the evolution of crystallographic texture for various deformation processes, such as uniaxial tension (SAVOIE *et al.* 1996), plane strain compression (BUNGE *et al.* 1986), rolling (GILORMINI *et al.* 1990; MORAWIEC *et al.* 1991; WIERZBANOWSKI *et al.* 1986; ZHOU *et al.* 1992), simple shear or torsion (ARZAGHI *et al.* 2009; BEAUSIR *et al.* 2007; JONAS and BACZMANSKI 1996), and deep drawing (CHOI *et al.* 2000; ZHOU *et al.* 1996). A rate-dependent viscoplastic relation has been employed in most of these models to generate the rotation rate field in the EAS. The rotation rate field and the orientation-based continuity equation have then been used to study the orientation stability of specific texture components of various (mostly FCC and BCC) materials. In this body of work, the orientation-based continuity equation has been used only to predict the ODF of stable texture

components at the end of the process. Although the continuity equation has been used in the literature to study the stability of ideal orientations, it has not been employed to statistically study the microstructure of materials. Therefore, formulation of a new orientation-based continuity model in the Eulerian framework is selected to be the subject of this study. A discrete representation of mass- and orientation-based continuity equations in the basis of Eulerian coordinate system is introduced in this research. This is a new hypothesis that has not been studied in the past which can be exploited to study microstructure evolution of polycrystalline materials.

To build the Eulerian model, instead of the ODF, a statistical function, called the *microstructure function M(x,g)*, is used. The microstructure function (MF) is a function of position x (in the mass-space) and orientation g (in the EAS). The MF represents the ODF (volume fraction of orientation g) at position x in the microstructure. In this way one can consider a local ODF for any material point in the microstructure; and instead of texture evolution, the evolution of the MF can be studied locally. The MF is used in formulations of mass- and orientation-based continuity equations. In fact, the MF, by definition, links the two spaces and it tells us how the material particles are moving in the mass space and at the same time how the orientations of those specific material particles are changing during the evolution process. The MF, in addition with the 2-point correlation function, which is used in statistical continuum theory to study the local effects of one material point on the properties of the neighboring point, is introduced in Chapter 2.

To measure the rotation of a particular grain in the microstructure, an overall velocity gradient tensor is applied, local stress and strain fields are defined (using a crystal plasticity model), and the lattice rotation tensor is obtained. The velocity components in the EAS are also

obtained from the lattice rotation tensor. Chapter 3 provides some of the most widely used crystal plasticity models along with their advantages and disadvantages. In addition, a rate dependent Taylor-like model that is used in this research is also provided. In this model, a calibrated power-law viscoplastic relation with a specific rate-sensitivity parameter is used such that it can be applied to model the microstructure evolution of FCC materials. Our proposed crystal plasticity model can be used to simulate stress-strain relations of any FCC materials under any type of deformation processes. In this research, only cold rolling process is considered.

Basics of texture analysis of rolled FCC materials are described in Chapter 4. As the deformation continues, some particular orientations (ideal orientations) are developed in the rolling microtexture of FCC materials. The stability of these ideal orientations is an important concept. Some stability criteria are discussed in this chapter. Moreover, the textural properties of pure nickel and formations of cell blocks, deformation inhomogeneities, and grain subdivisions, which are produced under very large levels of rolling deformations, are also provided in Chapter 4.

In the second part of this thesis (Chapters 5, 6 and 7), development of the Eulerian-based *double continuity (DC) model* is discussed in detail. In Chapter 5, first, the conservation of mass principle is provided, a two-dimensional plane-compression test (e.g. simple rolling) is modeled, and the evolution of an idealized two-phase microstructure under this process is investigated. To model the rolling deformation in this research, all environmental effects such as friction forces, temperature variations, and the complicated boundary conditions that are observed in an empirical rolling process are neglected. Derivation of the *mass-based continuity (MC) model* in the Eulerian coordinate system is provided in detail in Appendix A. In Chapter 6, the conservation of orientation principle and the *orientation-based continuity (OC) model* are

provided. Additional information about the derivation of the OC model has also been provided in Appendix C. After designation of the OC model in Eulerian formulations, this model was validated by examining a randomly-textured microstructure with 1000 random orientations. This model was compared against a regular Lagrangian model to investigate the accuracy of this model on the prediction of final microstructure at very large amounts of cold rolling. After verifications of MC and OC models, the double continuity model which is the combination of the two models is explained in Chapter 7.

To corroborate the DC model, a polycrystalline nickel material with an initially random texture is selected. Because the DC model has been designed for 3D implementation, a 3D microstructure (developed by Prof. A.D. Rollett's group at Carnegie Mellon University) is chosen, and crystallographic orientations are assigned into grains of this microstructure such that it statistically represents the microstructure of the original nickel sample. A genetic-algorithm scheme is employed, and a statistical error function of the original 2D and 3D microstructures is minimized to obtain the best combination of grain-orientation assignment. The 3D microstructure is then placed under a variety of rolling reductions and its final microstructure is captured and compared to the experimental microstructures. Results from these simulations are provided in Chapter 7. Additionally, to make comparisons between experimental and simulated microstructures, textural and statistical analyses of the results are carried out. These results are also provided in Chapter 7. More detailed formulation of the orientation-based continuity equation can be found in Appendix C.

PART I:

BACKGROUND AND LITERATURE REVIEW

2 MICROSTRUCTURE DESIGN AND STATISTICAL ANALYSIS

2.1 Microstructure Sensitive Design

During the past ten years a methodology has emerged for systematic design of material microstructures – called *Microstructure Sensitive Design (MSD)*. MSD has recently been developed by Adams, Kalidindi and their collaborators (ADAMS *et al.* 2005a; ADAMS *et al.* 2001; ADAMS *et al.* 2004; KALIDINDI *et al.* 2004; LYONS and ADAMS 2004). In this type of design, we start with a statistical description of a material microstructure using orientation distribution functions. These distributions are then used to establish quantitative linkages between the microstructure and the estimates or bounds on effective properties using available homogenization theories. A special feature of MSD is that these linkages are transformed into Fourier space, and discrete methods can be used to compute and manipulate the Fourier coefficients.

The most important tools of the statistical theory are the *probability density functions* and *correlation functions*. These functions are used to provide the information needed to derive the quantities of interest. The definitions and relationship between the probability density and correlation functions have been defined in the literature (ADAMS *et al.* 1989; GARMESTANI *et al.* 2001; KRONER 1967). Basically, the correlation functions are the means through which the statistical concepts are incorporated into the model. The simplest form of the statistical functions used to quantify the microstructure are the one-point distributions, which essentially reflect the

probability density associated with realizing a specified orientation in the neighborhood of a point thrown randomly into the microstructure. Higher order correlation functions, also referred to as n-point spatial correlation functions, have been defined in a variety of ways. The focus in this chapter is to introduce the first and the second-order statistical functions. Higher order n-point statistics are neglected in this research (for more information about 3- and higher n-point correlation functions the reader is referred to (GARMESTANI *et al.* 2001; LIN *et al.* 2000).

2.2 Homogenization Relations

In microstructure design, a methodology to link properties to microstructure is necessary to develop a framework for material design. The link between structure of materials in any length scale and their properties (most importantly mechanical and metallurgical properties) is critical in every engineering discipline. For this purpose, this research is focused on the homogenization relationships based on two-point statistical information to correlate the microstructure of the materials to their mechanical properties. Statistical distribution functions are commonly used for the representation of microstructures and also for homogenization of materials properties. The use of statistical functions allows the materials designer to include the morphology and distribution in addition to the properties of the individual phases and components. We start with an example where the statistical correlation functions are exploited to find the effective elastic stiffness tensor, C^*, (ADAMS *et al.* 2005b; GARMESTANI *et al.* 2001):

$$C^* = \underset{\text{1-point}}{\langle C \rangle} - \underset{\text{2-point}}{\langle C' \Gamma C' \rangle} + \underset{\text{3-point statistics}}{\langle C' \Gamma C' \Gamma C' \rangle} - \ldots \tag{2-1}$$

where C is the elastic stiffness, Γ includes the Green's functions, and $\langle p \rangle$ denotes the macroscopic average of the property, p. C' is the polarized stiffness tensor relative to a reference

tensor and is obtained by $C' = C - C^r$, C^r is the reference stiffness tensor. In this example, the 1-, 2-, 3-, and higher order n-point correlation functions are used to find an exact value of the effective elastic stiffness tensor; however, in most of the investigations reported in the literature, only the 1-point statistics haves been used to find an approximation of the effective property. The reason is that 2-point and higher order statistics are costly and many calculations must be carried out to increase the accuracy of the results. In this case, the relation between calculation time and the accuracy is not linear, and calculations for manipulating 3-point and higher order correlation functions are not yet accessible for regular computers. A similar formulation can be derived for plasticity:

$$N^* = \underset{\text{1-point}}{\langle N \rangle} - \underset{\text{2-point}}{\langle N' \Gamma N' \rangle} + \underset{\text{3-point statistics}}{\langle N' \Gamma N' \Gamma N' \rangle} - \ldots \tag{2-2}$$

where N is the plastic secant modulus. Of course the Green's function solution for plasticity differs from the elastic solution since the statement of problem is different. But, it is evident how the 1-, 2-, and higher-point statistics are employed for both elasticity and plasticity problems. In this research, only 1- and 2-point correlation functions are considered and higher order terms are neglected.

2.2.1 One-Point Distribution Function

The 1-point distribution function, which is used to calculate the first term on the right-hand-side of Eq. (2-1) or Eq. (2-2), is also called *orientation distribution function (ODF)*. This function describes the *crystallographic texture* in a given microstructure. The ODF, *f(g)*, is defined as (BUNGE and ESLING 1984; FULLWOOD *et al.* 2009c; GARMESTANI *et al.* 2001):

$$f(g)dg = \frac{V(g)}{V};\ \int_{\varphi_1}\int_{\phi}\int_{\varphi_2} f(g)dg = 1 \qquad (2\text{-}3)$$

where *f(g)* is the probability density around orientation *g*, and $dg = (1/8\pi^2)\sin\Phi d\varphi_1 d\Phi d\varphi_2$ is the invariant volume element in the hyper-spherical coordinate system defined with the help of Euler angles, $g = (\varphi_1, \Phi, \varphi_2)$. *V(g)* denotes the volume of the material associated with the orientations in the range $d\varphi_1 d\Phi d\varphi_2$. Note that since calculations of *f(g)* do not depend on the coordinate system, the normalization condition remains true for any particular choice of orthonormal coordinate axes associated with the *Euler Angle Space (EAS)* or *Fundamental-Zone (FZ)*. The fundamental-zone, by definition, is the space of orientations describing the complete set of physically distinct orientations relevant to a selected crystallographic phase, with distinctive lattice symmetry subgroup. To find the ODF, these steps should be followed: (i) orientations of crystallographic grains in the microstructure are obtained; (ii) the FZ is tessellated into desired bins (with equivalent volumes of *dg*); (iii) after applying the crystal and sample symmetries, orientations are mapped into the FZ; (iv) for every bin in the FZ, all orientations belonging to the selected bin are counted, and the fraction of these orientations with respect to the total number of orientations is reported as the value of the ODF for this specific bin; (v) a similar scheme is proceeded for the rest of the bins and the final ODF is measured. As it can be noted from Eq. (2-3), sum of the ODFs for the entire FZ must be equivalent to one.

2.2.2 Two-Point Correlation Function

Pair correlation functions (PCFs) or two-point correlation functions are employed in calculation of the second term on the right-hand side of Eq. (2-1) or Eq. (2-2). For example the second term in equation (2-1) can be rewritten as (ADAMS *et al.* 2005b):

$$\left\langle C'\Gamma C'\right\rangle_{ijkl} = \int_{R(r)} \int_{FZ} \int_{FZ} C'_{ijmn}(g) C'_{opkl}(g') \Gamma_{mnop}(-x) f_2(g, g' \mid r) dg dg' dr \tag{2-4}$$

where $f_2(g, g' \mid r)$ denotes the 2-point correlation function that describes the conditional probability density of finding orientations g and g' in the immediate neighborhood of an ordered pair of points $(x, x' = x + r)$. FZ denotes the space of all orientations, and $R(r)$ denotes the space of all vectors r that can be accommodated in the domain of interest, Ω in the real space. Higher order correlation functions can be introduced in the same manner, but only the 1- and 2-point correlation functions will be integrated in this research.

2.2.3 Microstructure Function

Microstructure functions, as a tool, will be used to explore the evolution of correlation functions in this study. As it will be seen later, the 1- and 2-point correlation functions can be easily recovered from the microstructure functions. Formally, a microstructure function, $M(x, g)$, defines the probability density associated with finding orientation g in the neighborhood of a spatial location of interest x; it is expressed as (ADAMS *et al.* 2005b; FULLWOOD *et al.* 2009c):

$$M(x, g) dg = \frac{dV_g}{V} \tag{2-5}$$

In this definition, the orientation g is an element of the continuous space of orientations, *FZ*, with an associated invariant measure dg. dV_g is the aggregated volume of the parts of V (the volume of the neighborhood) that is associated with orientations that lie within an infinitesimal invariant measure dg of g. The microstructure function is defined to satisfy the following normalization relations:

$$\int_{FZ} M(x,g)dg = 1; \quad \int_{FZ} dg = 1 \tag{2-6}$$

One convenient approach to representing the microstructure is to tessellate (discretize) the physical volume of interest, Ω, and the *FZ* into individual bins. The microstructure function $M(x,g)$ can then be expressed in the *primitive basis* (also called *indicator functions*) as:

$$M(x,h) \approx \sum_{s=1}^{S}\sum_{n=1}^{N} D_{sn}\chi_s(x)\chi_n(g) \tag{2-7}$$

where D_{sn} are the Fourier coefficients of the microstructure function. $\chi_s(x)$ is the indicator function for the spatial cell enumerated by the index s, which takes the value 1 for all points x lying in the cell, and 0 for points lying outside of it; and $\chi_n(g)$ is the indicator function for the orientations in the *FZ*, which takes the value 1 if the orientation in the cell n is g, and 0 if it is not.

Obviously there exist many other spectral representations that might be better suited for a given problem. The reason that the tessellation technique involving the primitive basis will be used is that later on a spectral method of fast numerical calculations, *Fast Fourier Transforms (FFTs),* can be used to efficiently compute the 1- and 2- point correlation functions. If the primitive basis and FFTs are used, it can be seen, for example, that the 2-point correlation function introduced in the previous section can be represented as:

$$f_2(h,h' \mid r_t) \approx \sum_{s=1}^{S}\sum_{n=1}^{N}\sum_{n'=1}^{N} F_t^{nn'}\chi_s(r_t)\chi^n(h)\chi^{n'}(h') \tag{2-8}$$

where $F_t^{nn'}$ are the coefficients of the 2-point correlation functions. The same approach can be applied for higher order correlation functions. For more information regarding the

implementation of FFTs in manipulating the 1- and 2-point functions, the reader is referred to the work of Fullwood (FULLWOOD *et al.* 2008).

3 CRYSTAL PLASTICITY THEORIES

The formulation of the macroscopic mechanical response of polycrystalline medium has been the subject of many studies and approaches. Due to the great practical interest in a large deformation polycrystalline theory, a lot of effort has been devoted to different approximate theories. In this chapter, a comprehensive review of crystal plasticity models that have been used in the past to predict deformation textures is given. These models are generally classified into *Sachs-type*, *Taylor-type*, *Self-consistent*, and *FEM* models. Advantages and/or disadvantages of these models in texture predictions are also discussed in this chapter.

3.1 Crystal Plasticity Models

3.1.1 Sachs-Type Models

The classical simulation of the deformation textures of polycrystals may be mainly classified into Sachs and Taylor type models. The *Sachs model* (SACHS 1928) is the first ever used crystal plasticity model. According to this model, it is assumed that the resolved shear stress on the principal slip system is the same for all crystallographic grains, and is identical to the critical resolved shear stress. This hypothesis implies that the stress tensor in each grain is proportional to the macroscopic stress tensor. It is also assumed that grains deform by single slip and there is no kinematical constraint due to grain interactions. Under these assumptions, grains

having distinct crystallographic orientations are deformed by different activated slip systems leading to unlikely overlaps and gaps at grain boundaries. The Sachs model has been used in the literature as a lower bound in texture analysis (as a reference see the work of (GAMBIN and BARLAT 1997)). In addition to the original Sachs' model, there are also some modified Sachs-type models that overcome the deficiencies of the original Sachs model –i.e. (GAMBIN and BARLAT 1997; PEDERSEN and LEFFERS 1987). In the literature, the modified Sachs-type models have been mainly employed into modeling of brass-type textures –i.e. (HIRSCH and LUCKE 1988a; LEFFERS 2006; LEFFERS and RAY 2009).

There are at least two objections to the Sachs' approach. Firstly, it is not possible to maintain compatibility among the grains when all the grains are assumed to deform by single slip. Secondly, it is assumed that the equilibrium of stresses is valid inside grains; however, it cannot be established across grain boundaries. To overcome the compatibility problem, Taylor (TAYLOR 1938) proposed a model that strictly enforces the compatibility by imposing an overall applied strain which will be identical for all grains in the microstructure.

3.1.2 Taylor-Type Models

The *Taylor model*, proposed by Taylor (TAYLOR 1938) and developed by Bishop and Hill (BISHOP and HILL 1951), is the most applicable model of crystal plasticity. In this model, it is assumed that the microscopic plastic strain is equal to the macroscopic plastic strain, while elastic strains are neglected. One of the advantages of this model is that the compatibility equations are satisfied since it deals with a uniform strain field in the entire microstructure; as a result, all grains plastically deform in the same manner in accordance with the macroscopic strain. Taylor-type models are commonly classified into the following groups in the literature:

3.1.2.1 Full Constraints (FC) Model

The first edition of the Taylor model (TAYLOR 1938) is called the *full-constraints model (FC model)* or the *classical Taylor model* in the literature. As it was mentioned, based on the Taylor assumption, the compatibility equations are satisfied, homogeneity of plastic strain throughout the polycrystal is guaranteed, but stress equilibrium at grain boundaries is neglected. It is found that using the FC-Taylor model for texture prediction of high *stacking-fault energy (SFE)* FCC metals gives satisfying results; however, it does not perform well for low SFE metals (HIRSCH and LUCKE 1988a; LEFFERS and RAY 2009).

The general framework of the Taylor model was later modified by Bishop and Hill (BISHOP and HILL 1951) to resolve the main problem of Taylor's theory for FCC polycrystals, stating that there must be a state of stress that can activate at least five slip systems at the same time. They modified the Taylor theory for polycrystals based upon the *principle of maximum work*. The primary aim of the Bishop and Hill theory was the computation of single and polycrystal yield surfaces. In this model, it is assumed that the unspecified elastic deformations will satisfy the equilibrium conditions. The Taylor-Bishop-Hill theories have been used extensively and successfully for texture predictions of FCC metals (BISHOP and HILL 1951).

The modified model still has an ambiguity with respect to the choice of active systems. For example, there are twelve slip systems for FCC materials that under the Taylor assumption, more than five slip systems must be activated at the same time, and an ambiguity with selection of appropriate slip systems must be anticipated. To overcome this ambiguity, different approaches have been reported in the literature. Honneff and Mecking (HONNEFF and MECKING 1978), for example, took an average value of all possible activated slip systems. Later on, Asaro and Needleman (ASARO and NEEDLEMAN 1985) proposed a rate-dependent model within which

slip systems are activated when they reach to a critical shear stress. Slip system ambiguity is resolved within the Asaro-Needleman rate-dependent models.

3.1.2.2 Relaxed Constraints (RC) Model

In the literature, the Sachs model is used as a lower bound, and the FC-Taylor model is used as an upper bound. Both models have some deficiencies and benefits. They can be improved by using intermediate conditions, i.e. by relaxing the strict constraints imposed by each model. A modification of the Taylor model, the method of *relaxed-constraints*, was firstly suggested by Honneff and Mecking (HONNEFF and MECKING 1978) and developed by Canova et al. (CANOVA *et al.* 1984). The idea here is to assume that when grains reorient and change their shapes, it is possible to partially relax the strict compatibility requirements imposed in the Taylor model. Non-uniform deformations that may appear at grain boundaries are excluded in the method. Two examples of the RC model are the *lath* and the *pancake model*, which are designed for materials with flat and elongated grains (e.g. in rolling). In these models, one or two of the shear terms are relaxed: for the RC-lath model, the L_{13} shear term (where L is the velocity gradient tensor) is relaxed and $\sigma_{13} = 0$, while for the RC-pancake model L_{13} and L_{23} are relaxed and $\sigma_{13} = \sigma_{23} = 0$. The methodology of relaxed constraints has been used by many authors to analyze deformation texture following several strain histories, e.g. axisymmetric tension and compression along with large simple shears in FCC polycrystals (DELANNAY *et al.* 2002; VAN HOUTTE *et al.* 2002; ZHOU *et al.* 1992). A comparison of FC and RC models for predicting the development of rolling texture in FCC metals (HIRSCH and LUCKE 1988a) show that the best approximation is given by the FC model at low degrees, by the lath model at intermediate degrees, and by the pancake model at high degrees of rolling.

Another RC-type model is the *LAMEL model* that has been developed by Van Houtte (VAN HOUTTE *et al.* 1999; VAN HOUTTE *et al.* 2005). According to this model, the average shape change of a set of two stacked grains is taken to be equivalent to the average shape change of the polycrystal, but in each of the two grains, relaxation is allowed to take place. Compared to the FC model, it has been reported that RC models can give a better prediction of rolling textures under large plastic deformations; however, one of the drawbacks of allowing for these relaxation strains is that the deformations of adjacent grains are not necessarily compatible to each other, as they are according to the FC-Taylor model. The deformations of the two adjacent grains (one placed on top of the other) considered in the LAMEL model are compatible without guaranteeing for compatibility with other neighboring grains. *Grain Interaction (GIA)* and *Advanced LAMEL (ALAMEL)* (VANHOUTTE *et al.* 2006) models are two other RC models that include the interaction of neighboring grains in calculations.

3.1.3 Self-Consistent Model

All theories based upon strain uniformity (Taylor-type models) fulfill compatibility conditions but not equilibrium at grain boundaries. In 1987, Molinari et al. (MOLINARI *et al.* 1987) proposed a *self-consistent approach* for the large deformation of polycrystals. Their approach was based on a scheme developed by Dederichs and Zeller (DEDERICHS and ZELLER 1973) in heterogeneous elasticity. In this approach, equilibrium and incompressibility equations are used to arrive at an integral equation for the local velocity gradient. This integral equation can then be solved via different approximate schemes. The principle of the self-consistent scheme is that the interactions between a particular grain and all others are simulated by those between the grain considered and a *homogeneous equivalent medium (HEM)*. In the self-consistent model of Molinari (MOLINARI *et al.* 1987), the equilibrium and the incompressibility

conditions were solved using the traditional Green's function method. An important advantage of Molinari's Green's function approach is that it fits naturally with correlation functions.

The self-consistent model can be incorporated with a rate-dependent viscoplastic relation such that the viscoplastic compliance tensor of the polycrystal is determined in each strain increment in a self-consistent manner. The *viscoplastic self-consistent (VPSC) model* is well suited to model large strain behavior of polycrystals. It accounts for the plastic anisotropy of each grain, as well as that of the polycrystal. It neglects elasticity at large strains. Each grain is modeled as an ellipsoidal inclusion that is embedded into the HEM with the average properties of the whole polycrystal. In this model, with the help of the viscoplastic compliance tensor and by solution of the Eshelby inclusion problem, the stress and strain state of each individual crystal is determined. For self consistency, the macroscopic stress and strain rate of the HEM can be set equal to the average of the stresses and strain rates of all the individual grains. Unlike the FC-Taylor model, the stress and strain rate of each grain can deviate from the corresponding macroscopic quantities, as well as deviate from each other. One consequence is that each grain changes its form according to its local velocity gradient and deformation history. Another important consequence of the self-consistent formulation is that a grain no longer needs to have five independent slip systems to deform. This feature is especially important for non-cubic crystal structures (e.g. HCP materials), where the number of available slip systems could be less than five on the basal or prismatic slip planes. Most of modifications, developments, and implementation of self-consistent models can be found in the work of Molinari (MOLINARI 1999; MOLINARI *et al.* 1997; MOLINARI *et al.* 1987), Lebensohn (LEBENSOHN 1999; LEBENSOHN and LEFFERS 1999; LEBENSOHN *et al.* 2007; LEBENSOHN *et al.* 1998), and others (TOME 1999; WANG *et al.* 2010).

3.1.4 Statistical Models

A comprehensive work on the statistical theory has been developed primarily by Beran (BERAN 1968), Beran and Molyneux (BERAN and MOLYNEUX 1966), and Kroner (KRONER 1967; KRONER 1977; KRONER 1986). Their contribution produced a basis to apply the theory to heterogeneous materials. Later on, Adams (ADAMS *et al.* 1989) presented a statistical formulation of the viscoplastic behavior in heterogeneous polycrystals by taking an approach which incorporates the statistical formulation of Molinari (MOLINARI *et al.* 1987)) and the *2-point correlation function* of lattice orientations. The statistical theory of Adams (ADAMS *et al.* 1989) was first applied to the prediction of initial texture evolution in FCC polycrystals under uniaxial creep (ADAMS and FIELD 1991). Evolution of the correlation functions was not considered in this initial work. Afterwards, Adams et al. (ADAMS *et al.* 2005a) showed how the problem of r-interdependence of the 2-point correlation functions can be overcome, by introducing the texture function as an intermediate tool. This work also elaborated on how to expand the solution in terms of generalized Fourier series. Garmestani and Li (GARMESTANI *et al.* 2001; LI *et al.* 2003) also used an approach based upon the statistical continuum theory using polycrystalline texture representation to describe texture evolution. This approach established a linear relationship between the rate of change of the texture coefficients and the texture coefficients. Further progress was made in other studies by Li and Garmestani (LI and GARMESTANI 2004; LI *et al.* 2005; LI *et al.* 2003) to find a direct relationship between texture coefficients and deformation parameters. They proposed a processing path function to describe the evolution of correlation functions in an inelastically-deforming two phase medium. They used the 2- and 3-point correlation functions and predicted the evolution of these correlation functions for a two-phase model.

Further work on the development of Adams' statistical modeling approach (ADAMS *et al.* 1989) was done by Fullwood et al. (FULLWOOD *et al.* 2009b). In this research, localization effects that are observed in the microstructure (because of the variation of elastic stiffness) were studied by incorporating statistical modeling and homogenization relations. In addition, previous issues with the Green's function integrals were resolved, and the method was validated against finite element analysis. This model was formulated to only consider the elastic localization effects without taking into account the plasticity relations. Another recent work (FULLWOOD *et al.* 2009a), however, was done to express the localization relations of a rigidly-plastic material. Results from these investigations show that the new methodology of integrating statistical modeling and homogenization relations can be reasonably used to predict the evolution of the microstructure of materials under any mode of deformation. A rate-dependent viscoplastic model that has been introduced by Adams (ADAMS *et al.* 1989) and has been developed by Fullwood (FULLWOOD *et al.* 2009a) is expressed in Section 3.2.

3.1.5 FEM Models

In this type of models, the interaction of grains can be accounted for and can be implemented into polycrystal plasticity constitutive equations in a finite element code. Some of the FEM models that have been developed to predict the texture evolution are presented here. One of the first works that included the effects of hardening phenomena was carried out by Kalidindi et al. (KALIDINDI and ANAND 1992; KALIDINDI *et al.* 1992). They developed a Taylor-type anisotropic polycrystalline plasticity model, together with a fully-implicit time-integration scheme. This model was implemented in a finite element program to simulate the evolution of crystallographic texture during bulk deformation processing of FCC metals –especially OFHC copper. Their Taylor-type constitutive model was in reasonable first-order agreement with

experiments for the evolution of the texture. The first edition of this model was only used for texture prediction of *initially-isotropic* FCC materials. Afterwards, they employed their Taylor-type model to predict the evolution of crystallographic texture in *initially-anisotropic, pre-textured* FCC materials (KALIDINDI and ANAND 1994). They used a pre-textured OFHC copper material and included work hardening of the material. The numerical and experimental results of their work were in excellent agreement. Kalidindi and his co-workers also improved and used their Taylor-type model in many other investigations, e.g. (ANAND and KALIDINDI 1994; KALIDINDI 2001; KNEZEVIC *et al.* 2008). Other usages of FEM models have also been reported in the literature. For example, most of advanced models that include grain interactions are developed in FEM format –e.g. (KUMAR and DAWSON 1998; KUMAR and DAWSON 2009; RITZ and DAWSON 2009; SARMA and DAWSON 1996; VAN HOUTTE *et al.* 2002).

3.2 Rate-Dependent Viscoplastic Model

In this section, a model that includes the rate-dependency of polycrystalline materials is introduced. This model is expressed by incorporating crystal plasticity and statistical continuum theories. We start with the basics of crystal plasticity for FCC materials. Since in many applications of polycrystal plasticity, elastic strains are much smaller than their plastic ones, and for the sake of simplicity, elastic strains are neglected, and, accordingly, it is assume that the plastic deformation is dominant. At room temperature, pure FCC metals deform predominantly by dislocation slip along specific crystallographic planes and directions. Slip follows densely-packed *{111}* planes in close-packed *<110>* directions, defining 12 potential slip systems (GODFREY *et al.*). In FCC metals with low SFEs, twinning is a second important deformation mechanism. Such materials are, however, not considered in the present work.

We start with the *Schmidt law* in crystal plasticity. When a single crystal with an arbitrary lattice orientation is deformed in tension, dislocations move along only one slip system. It is the slip system with the largest *resolved shear stress*, $\tau^{(s)}$, that starts motion of dislocations by shear:

$$\tau^{(s)} = \sum_i \sum_j \left(M_{ij}^{(s)} + M_{ji}^{(s)} \right) \sigma_{ij} \tag{3-1}$$

where $M_{ij}^{(s)} = \hat{b}_i^{(s)} \otimes \hat{n}_j^{(s)}$ denotes *Schmidt tensor* representing the geometrical properties of slip system *s*; while $\hat{b}^{(s)}$ and $\hat{n}^{(s)}$ are unit vectors indicating slip direction and slip plane normal of slip system *s*, respectively. σ is the *deviatoric Cauchy stress* tensor.

Now when the deformation starts, by applying a particular velocity gradient tensor L, some of the slip systems are activated and multi-slip occurs. A slip shear rate $\dot{\gamma}^{(s)}$ on the s^{th} slip system contributes to the local velocity gradient L with a simple shear rate equal to $\sum_s M_{ij}^{(s)} \dot{\gamma}^{(s)}$. However, the velocity gradient L cannot be achieved by slip alone. When L is decomposed into its symmetrical D and rotational W parts, it can be seen that an extra term, W^L, appears. This term is called the *lattice spin tensor* and is responsible for texture development in polycrystals.

3.2.1 Lattice Spin Tensor

As discussed in the previous section, to find the evolution of orientations, the lattice spin tensor, W^L, is required. The overall applied velocity gradient tensor L, the plastic component of the strain-rate D^P, the spin due to plastic flow W^P, and the lattice spin W^L are inter-related by the following relations:

$$L_{ij} = D_{ij}^P + W_{ij}^P + W_{ij}^L \tag{3-2}$$

$$D_{ij}^{P} = \sum_{(s)} \frac{1}{2}\left(M_{ij}^{(s)} + M_{ji}^{(s)}\right)\dot{\gamma}^{(s)} \tag{3-3}$$

$$W_{ij}^{P} = \sum_{(s)} \frac{1}{2}\left(M_{ij}^{(s)} - M_{ji}^{(s)}\right)\dot{\gamma}^{(s)} \tag{3-4}$$

$$L_{ij}^{P} = \sum_{(s)} M_{ij}^{(s)}\dot{\gamma}^{(s)} = D_{ij}^{P} + W_{ij}^{P} \tag{3-5}$$

If one knows the applied velocity gradient tensor L, to recover the lattice spin tensor, L^p must be obtained. This is achieved by recovering D^p, and hence $\dot{\gamma}^{(s)}$ from Eqs. (3-3) and (3-4). Then, using Eq. (3-5), L^p is obtained. Finally, W^L is calculated from Eq. (3-2).

In order to specify the material behavior, the slip shear rate $\dot{\gamma}^{(s)}$ must be given. There are many ways of choosing the slip shear rate in polycrystal plasticity. For instance, one can use the FC-Taylor assumption and take a selection of five dominant slip systems that minimizes the internal plastic work required, or maximizes the external plastic work, for plastic deformation – here one needs to deal with the Taylor ambiguity with respect to the choice of active systems. Another example is using the classical rate-independent Bishop and Hill model (BISHOP and HILL 1951), where the five active slip system are chosen among a set of active stress corners that maximizes the external work. The choice of selection of active slip systems is still difficult. Another approach for selecting the active systems is the widely accepted power-law viscoplastic relation. The viscoplastic model is rate-dependent and all slip systems are activated simultaneously based on their Schmidt tensor and their critical resolved shear stress. We use the power-law relation in this work.

3.2.2 Power-Law Viscoplastic Relation

The viscoplastic relation introduced here is identical to that defined by Hutchinson (HUTCHINSON 1976) for power-law steady creep by slip. For a resolved shear stress, $\tau^{(s)}$, acting on the s^{th} slip system, the *slip shear rate*, $\dot{\gamma}^{(s)}$, is connected by the equation:

$$\tau^{(s)} / \tau^{*(s)} = \left(\dot{\gamma}^{(s)} / \dot{\gamma}_0 \right)^m \tag{3-6}$$

where m is the rate sensitivity parameter, $\tau^{*(s)}$ is called either the *critical resolved shear stress* or the *slip resistance*, and $\dot{\gamma}_0$ is an arbitrary reference slip rate. The reference shear stress can be obtained from ordinary tension or compression testing. To use the viscoplastic relation, it is necessary to calibrate the model with experiments (FROMM 2008; KALIDINDI *et al.* 2006; KNEZEVIC *et al.* 2008).

To link the power-law viscoplastic relation into the calculation of lattice spin tensor, the *creep compliance tensor*, M_{ijkl} is introduced here (ADAMS *et al.* 1989). Therefore, the total plastic strain-rate tensor, Eq. (3-3), can be rewritten as:

$$D_{ij}^{P} = \sum_{s} \mu_{ij}^{(s)} \dot{\gamma}^{(s)} = M_{ijkl} \sigma_{kl} \tag{3-7}$$

Since we have used M for both the compliance tensor and the Schmidt tensor, to avoid confusion, symmetric part of the Schmidt tensor is introduced and used here as:

$$\mu_{ij}^{(s)} = \frac{1}{2} \left(\hat{b}_i^{(s)} \otimes \hat{n}_j^{(s)} + \hat{n}_j^{(s)} \otimes \hat{b}_i^{(s)} \right) \tag{3-8}$$

Inserting the slip shear rate from the viscoplastic model into Eq. (3-8), and noting that $\tau^{(s)} = \sum_i \sum_j \mu_{ij}^{(s)} \sigma_{ij}$ the components of the fourth rank tensor of creep compliances, M_{ijkl}, can be written as:

$$M_{ijkl} = \sum_s \left(\gamma_0 / \tau^{*(s)}\right) \left| \mu_{rs}^{(s)} \sigma_{rs} / \tau^{*(s)} \right|^{1/m-1} \mu_{ij}^{(s)} \mu_{kl}^{(s)}. \tag{3-9}$$

M is positive definite, and thus the inverse relationship to Eq. (3-9) exists, and is given as:

$$\sigma_{ij} = N_{ijkl} D_{kl} \tag{3-10}$$

where $N = M^{-1}$ is the *secant modulus tensor* and presents the following symmetry properties:

$$N_{ijkl} = N_{jikl} = N_{ijlk} = N_{klij} \tag{3-11}$$

The secant modulus is the inverse of the compliance tensor, and since the compliance tensor is non-linear in the deviatoric Cauchy stress, calculation of stress is complicated. A Newton-Raphson scheme can be employed to solve this problem, as used in (FROMM 2008). Once the deviatoric Cauchy stress is obtained, the slip shear rate can be calculated for all slip systems using Eqs. (3-1) and (3-6). The slip shear rate, then, can be implemented into equations in Section 3.2.1 to obtain the lattice spin tensor for further orientation evolution studies.

3.2.3 Slip Hardening

In Eq. (3-6) the slip resistance can differ from one slip system to another. Since we are working on a pure FCC material, it can be assumed that the slip resistances of all slip systems at any given location in the polycrystalline material exhibit similar slip resistance. Then, a saturation-type hardening model (as it can be found in (BRONKHORST *et al.* 1992; KALIDINDI and ANAND 1992)) can be used to update the slip resistance:

$$\dot{\tau}^* = h_0 \left(1 - \frac{\tau^*}{s_s}\right)^a \sum_{(s)} \left|\dot{\gamma}^{(s)}\right| \tag{3-12}$$

where $\dot{\tau}^*$ is the rate of change of slip resistance at time *dt* of the evolution process. To update the slip resistance simply at the end of the current iteration the slip resistance is renewed such that:

$\tau^*|_{new} = \tau^*|_{old} + (\dot{\tau}^*)\Delta t$. h_0, s_s, and a are the slip hardening parameters and their values can be obtained by carrying out an experimental tensile test.

3.2.4 Adjustments of the Viscoplastic Model

The rate-dependent viscoplastic model can be adapted to include the statistical functions that were introduced in Section 2.2. For any domain of polycrystalline material, and at any time, the field equations (constitutive, equilibrium, and the compatibility equations) must be satisfied. Field equations and the formulations for obtaining the velocity gradient tensor can be found in the work of Adams (ADAMS *et al.* 1989). After satisfying all the field equations and applying the interaction laws at each position *x* of the domain of interest, the local velocity gradient tensor, *L(x)*, can be expressed as:

$$L_{kl}(x) = \bar{L}_{kl} - \int_{R(\Omega)} \Gamma_{klmn}(\tilde{x})\, \tilde{N}_{mnrs}\left(\mathbf{L}(x'), g(x')\right) L_{rs}(x')\, dx'^{3} \tag{3-13}$$

where $\Gamma(\tilde{x})$ is the Green's function term and $\tilde{N}$ is the polarized secant modulus tensor. Note that $\tilde{N}(L(x'), g(x'))$ at each point x' depends upon the velocity gradient *L* and orientation *g* at that position. The integration is over $R(\Omega)$ which represents the set of all possible vectors $\tilde{x}$ in the region Ω. Note that $\tilde{x} = x - x'$ where x and x' represent points in the infinite space.

The above equation, in fact, explains how the statistical theory can be used to find an exact solution for the velocity gradient tensor at specific position *x*. It includes the localization effects from neighboring orientations that are at distance $\tilde{x}$ from the original point *x*. Pair correlation functions that have been introduced in Section 2.2 can be hired to statistically compute the local value of *L*. For example, the first term in the right-hand side (RHS) of Eq. (3-13) can be computed using the 1-point distribution function. Also, 2-point and higher order

correlation functions can be employed to compute the integral in the RHS of the equation. To make this more clear, Eq. (3-13) is rewritten in reduced form (with ignoring the 3- and higher order statistics) using the convolution properties (FULLWOOD *et al.* 2009a):

$$L_{kl}(x) \approx \overline{L}_{kl} - \Gamma_{klij}(\tilde{x}) * \tilde{N}_{ijmn}\left(L(x'), g(x')\right)\overline{L}_{mn} \tag{3-14}$$

In this equation, the first and second terms on the RHS can be computed by 1- and 2-point correlation functions, respectively. A suitable Green's function solution that accounts the viscoplasticity must be supplied.

The velocity gradients can be computed using a brute-force technique by modifying the size and direction of vector $\tilde{x}$ in $R(\Omega)$ and measuring the localization terms. However, a rapid method of calculation, *Fast Fourier Transforms (FFTs)*, is available *(FULLWOOD et al. 2009b)*. Compared to the brute force method, using FFTs are computationally much faster; however, as we will see in Part II, because this viscoplastic model must be formulated in the Eulerian basis, if we include the localization effects (from the second term in Eq. (3-14)), we then need to update L at every increment of deformation and recalculate the velocity fields in the real and orientation spaces. As we will see, updating the velocity fields will take an enormous amount of calculation time and it was decided to neglect the localization effects in this work. Further investigations, perhaps, can be conducted in the future –with fast massively parallel computer systems- to study the localization effects by polycrystal plasticity.

By ignoring the localization effects, Eq. (3-14) is reduced to the final form of $L(x) = \overline{L}$, that is in definition identical to the classical Taylor model (Section 3.1.2). Taking the Taylor assumption simplifies the viscoplastic model and we can take the FC-Taylor model except that we use the viscoplastic model to resolve the Taylor ambiguity. We name this model as Taylor-like viscoplastic (TLVP) model.

Now by taking the TLVP model, it is only necessary to calculate the Eulerian-based velocity fields in both mass and orientation spaces once, without any need to update the fields as plastic deformation proceeds. For the case of cold rolling, which is the only studied deformation mode in this work, it can be found that when the width to thickness ratio is over 10, the rolling process will be empirically similar to plane strain compression test (LENARD 2007); and the macroscopic velocity gradient tensor can be expressed as:

$$L^{app} = L_0 \begin{bmatrix} 1 & 0 & 0 \\ 0 & 0 & 0 \\ 0 & 0 & -1 \end{bmatrix} \tag{3-15}$$

where L_0 for the case of rolling is called *the deformation strain* (the true strain in the rolling direction). L_0 is taken to be *0.001 sec*$^{-1}$ in our calculations. Here 1-, 2-, and 3- directions are considered to be rolling, transverse, and normal directions. Also, the material is assumed to experience no strain in the transverse direction.

To simulate the rolling process based on the TLVP model, the applied velocity gradient tensor is given, and as a result, the local velocity gradients are defined $L(x) = L^{app}$. The applied velocity gradient tensor has the following influences: (i) in the real space, which is studied in Chapter 5, the mass velocity field resulting from such velocity gradient is steady and the movement of material particles can be monitored under an isochoric-motion process. (ii) in the orientation space, which is studied in Chapter 6, the applied velocity gradient is implemented into the TLVP model, the lattice spin tensor is calculated from Eq. (3-2), and the orientation velocity field (or *lattice rotation rate field*) is obtained –see Section 4.3. Additional information regarding to the evolution process and updating position and orientation of grains under such velocity fields is supplied in Part II of this thesis.

4 BASICS OF TEXTURE ANALYSIS

In this chapter, the main mathematical and textural concepts that are used to describe an orientation are defined and explained briefly. In addition, deformation texture and stability of some ideal orientations of FCC metals (and more specifically nickel) is explained. Depending on their mechanical and metallurgical properties, FCC metals react differently under cold rolling. For example, high and medium SFE metals (i.e. nickel) exhibit copper texture in their final rolled microstructure, while low SFE metals develop a brass-type texture. High/medium SFE metals also show cell-structure, cell blocks, and subdivision of grains at very large levels of cold works which makes it very difficult to predict the final texture of the material. All relevant theories of grain fragmentation of FCC metals are also discussed in this chapter.

4.1 Orientations and Rotations

In order to specify an orientation, it is necessary to set up two Cartesian *reference coordinate systems*: one relating to the specimen and the other relating to the crystal. The axes of the *sample* or *specimen coordinate system* $S=\{s_1,s_2,s_3\}$ are chosen according to important surfaces or directions associated with the external shape of the specimen, i.e. rolling (RD), transverse (TD) and normal (ND) directions in rolling. The *crystal coordinate system* $C=\{c_1,c_2,c_3\}$ is specified by directions in the crystal. The choice of directions is arbitrary,

although it is convenient to adapt it to the crystal symmetry, i.e. for orthogonal symmetry (cubic, tetragonal, orthorhombic) the axes *[l00]*, *[010]*, *[001]* are taken as the crystal coordinate system.

Having specified the specimen and crystal coordinate systems, an orientation is then defined as the position of the crystal coordinate system with respect to the specimen coordinate system, i.e. *Cc*=*g*.*Cs*; where *Cc* and *Cs* are the crystal and specimen coordinate systems respectively, and *g* is an orthonormal matrix called the *orientation matrix*. The orientation matrix can be expressed in several different ways, among which the Bunge convention (BUNGE 1993) of Euler angles is more common in the literature. The elements of the orientation matrix in terms of the Euler angles are given by:

$$\overset{S\to C}{g} = \begin{bmatrix} \cos\varphi_1\cos\varphi_2 - \sin\varphi_1\sin\varphi_2\cos\Phi & \sin\varphi_1\cos\varphi_2 + \cos\varphi_1\sin\varphi_2\cos\Phi & \sin\varphi_2\sin\Phi \\ -\cos\varphi_1\sin\varphi_2 - \sin\varphi_1\cos\varphi_2\cos\Phi & -\sin\varphi_1\sin\varphi_2 + \cos\varphi_1\cos\varphi_2\cos\Phi & \cos\varphi_2\sin\Phi \\ \sin\varphi_1\sin\Phi & -\cos\varphi_1\sin\Phi & \cos\Phi \end{bmatrix} \quad (4\text{-}1)$$

where $(\varphi_1, \Phi, \varphi_2)$ are the three *Euler angles* used to rotate the sample coordinate system into the crystal coordinate system. Any orientation expressed in terms of its Euler angles can be represented as a point in the three-dimensional *Euler angle space (EAS)*. In the most general case of triclinic crystal symmetry and no sample symmetry, the Euler angles are defined in the range $0^o \le \varphi_1, \varphi_2 < 360^o$ and $0^o \le \Phi \le 180^o$, which in turn defines the maximum size of the Euler space, the so-called *asymmetric unit*, $SO(3)$. Symmetries of the crystal and/or the sample, however, result in different (but equivalent) descriptions of a given orientation. Such symmetries lead to a reduction in the size of the Euler space –see Table 4-1.

Table 4-1: Size of the Euler space necessary to represent unequivocally orientations for different sample and crystal symmetries

Crystal Structure	Crystal Symmetry		Sample Symmetry		
			Orthotropic	Monoclinic	Triclinic
	Φ	φ_2	φ_1	φ_1	φ_1
Cubic	90°	90°			
Tetragonal	90°	90°			
Orthorhombic	90°	180°			
Hexagonal	90°	60°	90°	180°	360°
Trigonal	90°	120°			
Monoclinic	90°	360°			
Triclinic	1800°	360°			

As it can be seen from the table, different sample symmetries affect the range of the angle φ_1. In samples deformed by rolling, it is usually assumed that there is a two-fold symmetry axis parallel to each of the three sample axes. This is the case of orthotropic or orthorhombic sample symmetry, and the range of the Euler angle φ_1 is reduced to $0^o \le \varphi_1 < 90^o$.

Crystal symmetry further reduces the size of the Euler space by affecting the range of the angles Φ and φ_2. For cubic crystal symmetry (FCC or BCC materials) there are 24 possibilities to describe one and the same orientation of a cube in any reference frame; therefore, the Euler space can be subdivided into 24 equivalent subspaces. This space is called the *cubic fundamental zone* (*FZ*$_C$.) and has a curvature at its boundaries along the Φ direction. This will cause problems in using FFTs (Section 3.2.4) because the FFT domain is required to be cubical or rectangular in shape. To overcome this problem, only the three 4-fold axes and the six 2-fold axes rotations of crystal symmetry are considered, and the FZ_C is reduced to the range $0^o \le \varphi_1 < 360^o$ and $0^o \le \Phi, \varphi_2 < 90^o$, which is called *FZ*$_{3C}$. If both sample and crystal symmetries are applied, this

space is reduced in φ_1 direction, represented in Fig. 4-1, that can be used to study the orientation of rolled FCC materials.

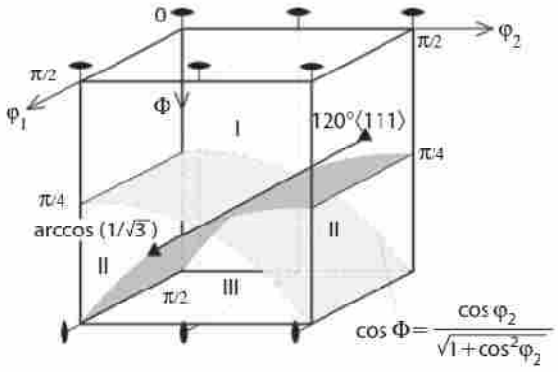

Fig. 4-1: Symmetry elements in the Euler space for cubic crystal symmetry and orthotropic sample symmetry

The orientation space that is shown in Fig. 4-1 include Euler angles of the range $0^o \le \varphi_1, \Phi, \varphi_2 < 90^o$. Because this space includes the orthorhombic sample symmetry and is four times smaller than the normal FZ_{3C}, we label it as $FZ_{3C/4}$ throughout this thesis. As we will see later, this space can be tessellated into small equivalent cubical bins and evolution of orientations in this space can be studied using the orientation-based continuity model to update the microstructure function and capture the final microstructure (Chapter 6).

4.2 Deformation Texture in FCC Materials

Pure FCC metals and alloys are known to exhibit two types of rolling textures, namely brass or alloy-type in materials of low SFE; and copper or pure metal-type in materials of medium or high SFE. A large number of investigations have been carried out to characterize the rolling texture of pure metals and a number of their alloys. In FCC metals, where slip and

twinning are the two major systems of deformation, SFE is the most significant material parameter that determines the mode of deformation. SFE, by definition, determines the extent to which unit dislocations dissociate into partial dislocations. Such dissociation, which happens in low SFE materials, hinders the climb and cross slip of dislocations; as a result, the ability of the material to change its shape during plastic deformation by slip alone is reduced, and therefore deformation twinning may occur. Examples of medium and high SFE metals are copper, nickel, and aluminum, while two examples of metals with low SFE are silver and gold. A reasonable value of the SFE of nickel as estimated from its coherent twin energy, is reported as *128 mJ/m^2 (HUMPHREYS and HATHERLY 2004)*. This places nickel in the medium SFE class between that of pure aluminum and pure copper.

Various observations have been reported on the formation of the brass and copper textures. As it has been reported in a review paper by Leffers and Ray (LEFFERS and RAY 2009) studies have shown different conclusions on the formation of these two types of textures. For example, early in 60s, Wassermann (WASSERMANN 1963) suggested that the brass-type texture is formed by a volume effect of deformation twins while the copper-type texture is generally formed by slip without twinning. Afterwards, Dillamore and Roberts (DILLAMORE and ROBERTS 1964) suggested that the copper-type texture is formed when there is extensive cross slip while the brass-type texture is formed when the cross-slip frequency is low (or zero). Later on, Hu and Cline (HU and CLINE 1966) suggested that the brass-type texture is produced by slip of partial dislocations combined with slip by perfect dislocations while the copper-type texture is produced by slip by perfect dislocations only. Concluding from most of the reviewed papers, it is obvious that copper type texture forms when slip (or cross-slip) is dominant, and brass texture forms when deformation twins (even with a small fraction) appear. Deformation twins, however, have

not been reported for commercially pure nickel (HORTON *et al.* 1995; PARK and PARKER 1989; RAY 1995), and it is expected to have a copper-type texture.

Prediction of brass- and copper-type textures by typical crystal plasticity models has also been reported in the literature. There are convincing evidences that the development of the copper-type texture can be explained by Taylor-type models with straight-forward *{111}<110>* slip. For example, Leffers (LEFFERS 1968) showed that the Taylor model and RC-Taylor models, leads to a copper-type texture. It is also found that the combination of the Taylor model with the formation of a large volume fraction of deformation twins provides reasonable simulations of the brass-type texture, but the volume fraction of twins implied is far greater than that observed experimentally. Additionally, works of Hirsch and Lucke (HIRSCH and LUCKE 1988c), Kallend and Davies (KALLEND and DAVIES 1972), Van Houtte (VAN HOUTTE 1978), and Kalidindi (BACHU and KALIDINDI 1998; KALIDINDI and ANAND 1992; KALIDINDI *et al.* 1992) show that Taylor-type models can predict a reasonable copper-type textures for FCC rolled metals. Sachs-type models, however, are used to predict the brass-type texture without overestimating the volume fraction of deformation twins. For instance, the modified Sachs model (LEFFERS 1979) gave simulated textures which approach quantitative agreement with the experimental brass-type texture at 50% and higher reductions.

To study the rolling texture of FCC materials, ideal components of the texture (see Table 4-2) can be used for further analysis. The copper-type texture is characterized by Copper, S, and Brass components, while the brass- or alloy-type texture has only the Brass component. As discussed earlier, copper-type texture is found in medium and high SFE metals; however, the texture that is seen in aluminum (high SFE) is taken as the aluminum-type texture distinguished from copper-type texture by having stronger S component (LEFFERS and RAY 2009).

Development of rolling texture in pure nickel, nickel-iron and nickel-cobalt alloys have been studied by Ray (RAY 1995). It has been reported that the rolling texture of pure nickel and the nickel-iron alloys are quite similar lying somewhere in between the deformation textures of pure copper and pure aluminum (more likely closer to the copper texture). However, in nickel-cobalt alloys, brass texture is dominantly observed by increasing the amount of cobalt.

The representation of rolling textures is by the system *{hkl}uvw>*, where *{hkl}* is the crystallographic plane parallel to the rolling plane, and *{uvw}* is the crystallographic direction parallel to the rolling direction. Ideal rolling texture components of FCC materials are presented in Table 4-2.

Table 4-2: Ideal texture components in rolled FCC metals

Texture Component	Miller indices		Euler angles		
	{hkl}	*<uvw>*	φ_1	Φ	φ_2
Cube	(1 0 0)	[0 $\bar{1}$ 0]	0	0	0
Goss (G)	(101)	[0 $\bar{1}$ 0]	0	45	90
Copper (C)	(112)	[$\bar{1}$ $\bar{1}$ 1]	90	35	45
Brass (Bs)	(101)	[$\bar{1}$ $\bar{2}$ 1]	35	45	90
Taylor (T) / Dillamore (D)	(4 4 11)	[$\bar{11}$ $\bar{11}$ 8]	90	27	45
S	(213)	[$\bar{3}$ $\bar{6}$ 4]	59	37	63

In addition to the texture components, texture fibres are also studied during texture analysis. There are three dominant texture fibres appearing in the rolling texture of FCC materials: α- and β-and γ-fibres. The α-fibre, which is parallel to the rolling direction

($\varphi_1 = 0^o, \varphi_2 = 45^o, \Phi = 0^o - 90^o$), connects brass and Goss components; the β-fibre runs from the Copper position through the S position and meets the α-fibre at the Brass position; and, the γ fibre has {111} parallel to the normal direction and runs in the φ_1 direction ($\Phi = 55^o, \varphi_2 = 45^o, \varphi_1 = 0^o - 90^o$). α- and β-fibres are observed in pure FCC metals while the γ-fibre is produced in the development of texture in FCC alloys (BUNGE and SCHWARZER). A schematic representation of the α- and β-fibres is given in Fig. 4-2, where one of the two branches has been omitted for the sake of clarity (HIRSCH and LUCKE 1988b; HUMPHREYS and HATHERLY 2004). The omitted branch is that observed in the section where $\varphi_2 = 45^o - 90^o$.

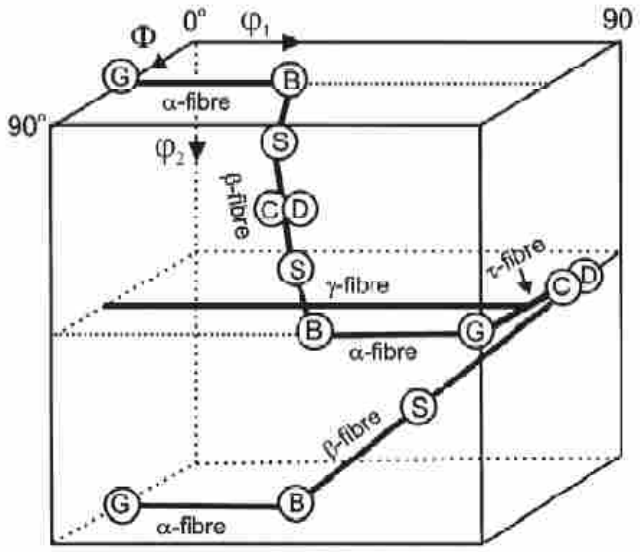

Fig. 4-2: A schematic representation of rolling fibres for FCC materials with orthorhombic sample symmetry.

The density of orientations along the fibres changes as the rolling process continues. One way to study the development of fibres is to find the density of orientations around each fibre

and depict the fibre-plots. In this research, in addition to pole figures and ODF section plots, plots that show the ODF intensities along the α- and β-fibres are also provided, Section 7.3.

An extensive work on the texture development of rolled FCC metals has been summarized by Hirsch and Lucke (HIRSCH and LUCKE 1988b). They rolled aluminum, copper and a series of copper-zinc alloys to different degrees of rolling reductions. The results of their investigations reveal that, at very low degrees of rolling, the orientation densities for these alloys are distributed homogeneously along the entire length of the α-and β-fibres. At intermediate degrees of rolling, they observed that the homogeneity of the tubes deteriorates, i.e. the density of Goss decreases in contrast to the continuous increases at the Brass orientation and along the entire β-fibre. For example, for aluminum and copper (high SFE), the α-fibre almost disappears (except for Brass) at 96% reduction, while the β-fibre is still quite pronounced. At very high degrees of rolling, the intensity of Copper and Brass components increases with deformation. At this stage, the intensity of the S component, however, increases dramatically and it becomes the strongest maximum.

4.3 Lattice Rotation Rate Field

The lattice spin causes the orientation changes in the microstructure. These changes are finite and can be obtained once W^L is available for every point in the orientation space. Basically, to obtain the lattice rotation rate field, the cubic-orthorhombic fundamental zone ($FZ_{3C/4}$) that was expressed in Section 3.2.4 is selected, and these steps are followed: (i) $FZ_{3C/4}$ is tessellated into small cubes (bins) with equivalent volumes; (ii) using the Taylor-like viscoplastic (TLVP) model, local values of W^L for the center point of bins in the $FZ_{3C/4}$ are obtained; (iii) for every bin in the space, the infinitesimal lattice rotation vector which is defined as

$\dot{\varpi}_i = -1/2\varepsilon_{ijk}W_{jk}^L$ is computed; (iv) finally, the increments of Euler angles or the velocity components of orientation changes in the Euler space $\dot{g} = (\dot{\varphi}_1, \dot{\Phi}, \dot{\varphi}_2)$ is obtained by:

$$\begin{aligned}
\dot{\varphi}_1 &= -\cot\Phi\sin\varphi_1\dot{\varpi}_1 + \cot\Phi\cos\varphi_1\dot{\varpi}_2 + \dot{\varpi}_3 \\
\dot{\Phi} &= \cos\varphi_1\dot{\varpi}_1 + \sin\varphi_1\dot{\varpi}_2 \\
\dot{\varphi}_2 &= \csc\Phi\sin\varphi_1\dot{\varpi}_1 - \csc\Phi\cos\varphi_1\dot{\varpi}_2
\end{aligned} \tag{4-2}$$

Note that W^L is an anti-symmetric tensor and has this property $W_{ij}^L = -W_{ji}^L$; thus, the lattice rotation vector can be expressed as $\dot{\varpi}_i = (W_{32}^L, W_{13}^L, W_{21}^L)$. The vectors $\dot{\varpi}$ and $\dot{g}$ physically have similar meaning, but they show the orientation changes in different spaces. $\dot{\varpi}$ represents the orientation changes in a Cartesian coordinates, while $\dot{g}$ shows these changes in the (curved) Euler space. The vector $\dot{g}$ can, therefore, be treated here as an orientation velocity vector that indicates how orientation *g*, which has been located at a specific position in the Euler space ($FZ_{3C/4}$), is moved in the orientation field. After obtaining all velocity vectors, $\dot{g}$, for the entire $FZ_{3C/4}$, the velocity rotation field (orientation flow field) can be constructed. It is difficult to illustrate a 3D plot of the orientation field; therefore, a simple 2D section of the orientation field is shown in Fig. 4-3.

As it can be seen in Fig. 4-3, there are some regions where the flow is accumulating toward certain points. These points correspond to crystallographic grains that deform without orientation change. In other words, if, in the vicinity of *g**, the flow field is oriented towards *g**, then it is considered to be a stable end-orientation of the deformation process and we will have $\dot{g}_i(g^*) = 0$; if the flow is oriented away from *g** then it will be an unstable orientation; and finally meta-stability may occur when there are partly stable and partly unstable orientations around *g**. To study the flow field and find the places of stable end-orientations, there are several stability tests that will be introduced in the next section.

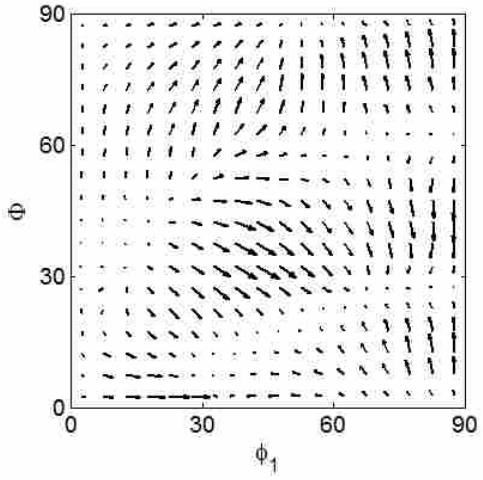

Fig. 4-3: A 2D section plot of the conventional cubic FZ_{3C} indicating the lattice rotation rate field of orientations in the $\varphi_2 = 45^o$ section.

4.4 Stable Orientations and Stability Criteria

There are several ways to examine the stability of orientations based on their lattice rotations. According to Clement (CLEMENT 1982), an orientation *g* is considered to be a stable-end orientation when the three components of $\dot{g}$ are equal to zero and their first-order partial derivatives are negative:

$$\dot{\varphi}_1 = \dot{\Phi} = \dot{\varphi}_2 = 0 \quad and \quad \frac{\partial \dot{\varphi}_1}{\partial \varphi_1} < 0, \frac{\partial \dot{\Phi}}{\partial \Phi} < 0, \frac{\partial \dot{\varphi}_2}{\partial \varphi_2} < 0 \tag{4-3}$$

When the velocity terms are zero, it represents that the location of those particular grains are not changing throughout the deformation process; furthermore, the negativity of partial derivatives of velocity terms indicates that in the vicinity of the orientation there are more grains rotating towards it than rotating away from it.

For most of plastic deformation processes, the above criterion is not valid for the entire Euler space; additionally, it is often of interest to evaluate the relative stability of orientations.

Therefore, Toth (TOTH *et al.* 1988) proposed an alternative stability criterion in which the amount of stability is expressed by a stability parameter *P*:

$$P = \ln\left(\frac{\bar{\dot{\varepsilon}}}{|\dot{g}|}\right) \tag{4-4}$$

where $\bar{\dot{\varepsilon}}$ is the von Mises equivalent strain rate, and $|\dot{g}|$ is the length of the lattice rotation vector. Based upon this criterion, the highest stability of an orientation is obtained when the norm of the velocity vector is very small, and when *P* is relatively large. The only difficulty with this parameter is that it becomes infinity when $|\dot{g}| = 0$, which can happen more specifically for deformation modes such as rolling (TOTH *et al.* 1990). $|\dot{g}|$ in this stability criterion is defined as:

$$|\dot{g}| = \sqrt{\dot{\varphi}_1^{\,2} + \dot{\Phi}^2 + \dot{\varphi}_2^{\,2} + 2\dot{\varphi}_1\dot{\varphi}_2\cos\Phi} \tag{4-5}$$

Lately, Arzaghi (ARZAGHI *et al.* 2009) proposed a new stability parameter that can be used for any deformation mode:

$$P = 1 - \left(\frac{|\dot{g}|}{G_{max}}\right) \tag{4-6}$$

where $G_{\max}$ is the maximum value of $|\dot{g}|$, and *P* varies between 0 and 1.

Another stability criterion that can be used to assess the relative orientation stability is the divergence of the rotation velocity field, $div\dot{g}$. The divergence of the orientation flow density is derived in Appendix C as:

$$div\dot{g} = \frac{\partial\dot{\varphi}_1}{\partial\varphi_1} + \frac{\partial\dot{\Phi}}{\partial\Phi} + \frac{\partial\dot{\varphi}_2}{\partial\varphi_2} + \dot{\Phi}\cot\Phi \tag{4-7}$$

While Eq. (4-3) requires the flow field to be convergent along all the three axes, $div\dot{g} < 0$ signifies an overall convergent orientation flow. All stability criteria mentioned in this section,

Eqs. (4-3), (4-6), and (4-7), are used in this research to examine the stability of ideal rolling orientations.

4.5 Grain Fragmentation and Formation of Microbands in Cold-Rolled Nickel

Metals of high or moderate SFE typically deform by slip. At low degrees of deformation, the deformation is homogeneous; but, for large levels of deformation, by increasing the density of dislocations, regions of dislocation pileup develop within the original grains. It is found that at large levels of deformation, an individual grain, particularly in coarse-grained materials, subdivides (on a large scale) into different regions with various orientations. Grain subdivision is caused by either inhomogeneous stresses transmitted by neighboring grains, or by the intrinsic instability of the grain during plastic deformation. Resulting fragmentation of grains can be studied macroscopically or microscopically.

On the macroscopic scale, the developed regions of inhomogeneity are called *deformation bands*. These bands deform on different slip systems and may develop separate regions with clearly different orientations. Between the deformation bands there are narrower regions termed *transition bands*. Another type of larger-scale bands is termed *shear bands*, which are non-crystallographic in nature and may pass through several grains. Deformation, transition and shear bands can be developed in large plastic deformations of most common metals.

On the microscopic scale, subdivision of grains may result into creation of *cells* and *cell-blocks*. Many studies (HANSEN and JENSEN 1999; HANSEN *et al.* 1987; HIRSCH *et al.* 1988; HUGHES and HANSEN 1993; HUGHES and HANSEN 1995; HUGHES and HANSEN 2000) have shown that for medium and high SFE metals: (i) at low and medium degrees of rolling, highly inclined boundaries are arranged and form *dense dislocation walls (DDWs)* and *microbands*

(MBs); (ii) as the level of deformation is increased, cell boundaries become nearly parallel to the rolling direction and *lamellar boundaries (LBs)* are developed; (iii) at larger levels of strain, most of the boundaries become lamellar boundaries.

To study the development of microscopic cell-blocks (DDs, MBs, and LBs) we need to classify the dislocation boundaries based on their formation and their structural properties. Basically, dislocation boundaries are divided into *geometrically necessary boundaries (GNBs)* and *incidental dislocation boundaries (IDBs)*. The extended cell-block boundaries (DDWs/MBs and LBs) are GNBs which separate regions that deform by different slip system combinations, strain amplitudes, and strain. On the other hand, the ordinary cell boundaries are IDBs that form by trapping of glide dislocations. To visualize the formation of cell-blocks and cells in the microstructure of FCC metals, a 3D schematic of a heavily-rolled microstructure (extracted from (HUGHES and HANSEN 2000)) is illustrated in Fig. 4-4.

In this figure, LBs are shown as nearly horizontal sheets in the rolling plane. The narrow channels between the LBs are bridged by cell boundaries, forming a bamboo structure. For most medium and high SFE metals, the majority of the DDWs/MBs, LBs and subgrains are medium (3-15^{o}) and high angle boundaries (>15^{o}), whereas the cell boundaries are predominately low angle boundaries (<3^{o}).

Subdivision of grains in the microstructure of heavily-deformed nickel has been studied by Hughes and Hansen (HUGHES and HANSEN 1993; HUGHES and HANSEN 2000) and lately by Chen et al. (CHEN *et al.* 2008). Fig. 4-5 demonstrates TEM micrographs of a pure nickel (99.99%) rolled to reductions of 70, 90, and 98%. This figure is extracted from the work of Hughes and Hansen (HUGHES and HANSEN 2000).

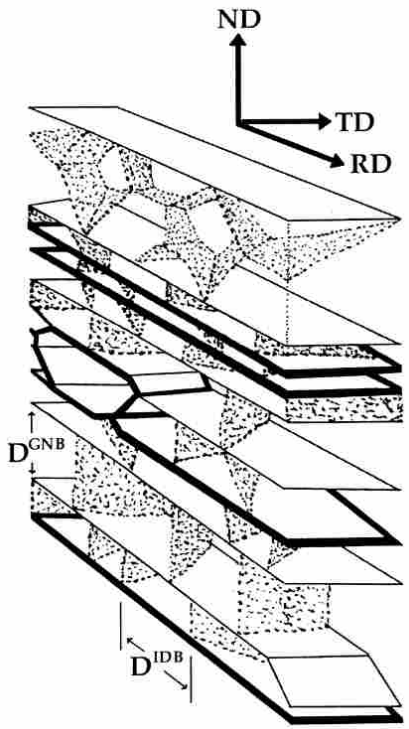

Fig. 4-4: Schematic representation of a large strain dislocation structure demonstrating sheets of extended LBs with IDBs bridging between them. High LBs are represented by heavy line weight. (extracted from HUGHES and HANSEN 2000)

Comparison of all three micrographs in Fig. 4-5 shows a structural transition that occurs in the microstructure of most heavily-deformed high SFE metals. In this transition, extended boundaries that are inclined to the rolling plane rotate and develop a structure dominated by boundaries almost parallel to the rolling plane. For example, Fig. 4-5 (a) shows this transition clearly. The more highly inclined boundaries are DDWs and MBs, whereas the boundaries nearly parallel to the rolling direction are LBs. The transition from DDWs and MBs into LBs is facilitated by the intense coarse slip of S-bands marked as S in micrographs. As the level of strain is increased, Fig. 4-5 (b,c), most of the boundaries rotate and become LBs. Both the

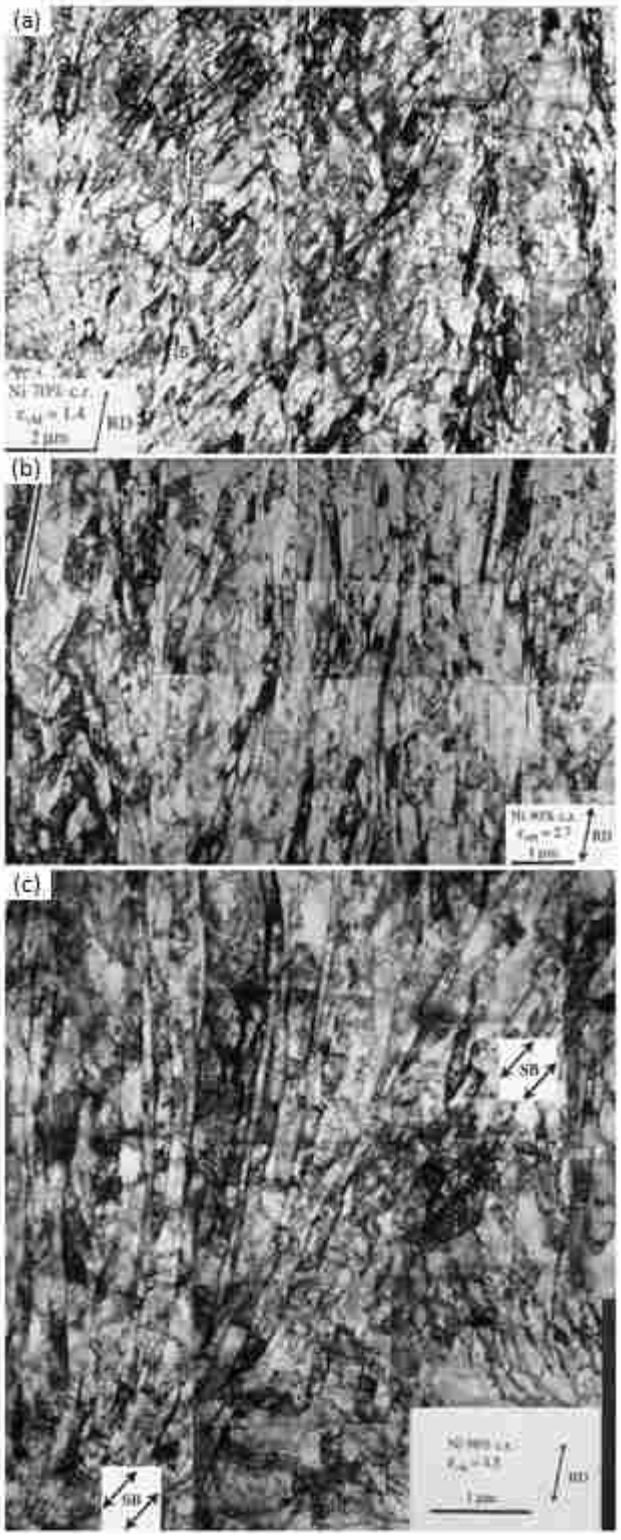

Fig. 4-5: TEM micrographs of the dislocation microstructure developed during cold rolling of nickel after (a) 70%, (b) 90% , and (c) 98% cold roll. Studied plane is the TD section (extracted from HUGHES and HANSEN 2000).

DDWs/MBs and LBs delineate cell-blocks which are subdivided by cell boundaries. Accordingly, by increasing the number of LBs, grain subdivision occurs and layers with similar orientations are developed in the microstructure.

Modeling fragmentation of grains and development of cell-blocks has been the subject of many studies –e.g. (BEAUDOIN *et al.* 1996; BECKER and PANCHANADEESWARAN 1995; LEFFERS 2001; MIKA and DAWSON 1998; MIKA and DAWSON 1999). In most of these studies, FEM models were developed and used to examine the interactions of a few grains, and predict the place where fragmentation is occurred.

The aim of this section was to provide a brief literature review on the theory of the formation of inhomogeneous regions in the microstructure of nickel, and explore problems that may affect the outcome of the proposed continuity model. Subdivision of grains is the most serious concern as it occurs in the experimental microstructure, because the proposed continuity model does not include this phenomenon in simulations. It is possible to develop an Eulerian continuity model that incorporates the grain fragmentation, but, as it was found in most of FEM models, this requires major computational resources, and it was decided for this work to exclude the effects of inhomogeneity and grain subdivisions in the continuity model. In comparing simulations with experimental characterizations, as will be presented in Chapter 7, it is found that above ~50% rolling reduction there are clear indications of the influence of fragmentation on microstructure development.

PART II:

DEVELOPMENT OF THE EULERIAN-BASED DOUBLE CONTINUITY MODEL

Formulations of a new model, which can be used to study the microstructure evolution of any type of polycrystalline material under any deformation mode, are developed and results are discussed. Since at every point in the microstructure, two important features of the microstructure (position and orientation of grains) must be considered in any simulation method, evolution of the MF, which represents the distribution of the examined orientation within a small neighborhood of the examined particle, is generally studied in this research. Although most other models have used the Lagrangian system, it was decided to use the Eulerian coordinate system. The reason for choosing the Eulerian system is that for the validation of the new model, the 2- point statistics of the microstructure must be manipulated using FFTs. To use FFTs a rectangular grid must be selected, and, as discussed earlier, the shape of the Lagrangian mesh becomes distorted by deformation. Another reason is that, as we will see, calculations by the Eulerian continuity model are computationally faster as compared to the Lagrangian model. In this part of the thesis, concepts of mass- and orientation- conservation are expressed and validated in Chapters 5 and 6, respectively. Thereafter, the linkage of mass- and orientation-based continuity equations (the double continuity relation) is introduced and corroborated against experimental results in Chapter 7.

5 KINEMATICS AND THE MASS EVOLUTION

In Continuum Mechanics, *Dynamics*, which is the science of motion of bodies, is often subdivided into *Kinematics* and *Kinetics*. Kinematics deals with the motion of material particles in a continuous body with velocity and acceleration as the most important concepts. In the material (or real) space, the motion of material particles is monitored by the mass-based continuity equation, which is derived based upon the conservation of mass principle. The main application of this continuity equation is in finding the solution to Navier-Stokes equations in fluid mechanics (KREISS and LORENZ 2004). In the derivation of Navier-Stokes equation, the continuity equation can be expressed in either material (Lagrangian) or spatial (Eulerian) framework; and it can be used to monitor the motion of particles for a compressible or an incompressible fluid. The continuity equation has been applied mostly for linearly viscous fluids in the literature (IRGENS 2008; KREISS and LORENZ 2004; LAI *et al.* 1993); and its application for solid materials is not common. In this chapter, we will introduce the mass-based continuity equation and will show how it can be employed to model changes in the microstructure that occur with large deformations.

5.1 Conservation of Mass Principle

The principle of conservation of mass states that the total mass of any part of a body does not change with any motion. The mathematical form of this principle is different in material and

spatial descriptions of motion. One benefit of using the Eulerian coordinate system for computations is that one can discretize the volume of interest using square-shaped, evenly-spaced grids, facilitating the use of FFTs for economical calculations (FULLWOOD *et al.* 2008). Another benefit is that we can use the *finite difference method (FDM)* to approximate first-order partial derivatives that appear in the continuity equation.

The derivation of the *mass-based continuity (MC) equation* for the spatial description is shown in Appendix A. Using the definition of the material time derivative *D/Dt*, and taking a control volume in the Eulerian coordinates, the MC equation is expressed as (Eq. (A-5) in Appendix A):

$$\frac{\partial \rho(x)}{\partial t} + div\big(\rho(x)v(x)\big) = 0 \tag{5-1}$$

where $\rho(x)$ is the mass density and $v(x)$ is the velocity of the material point x in the mass flow field. Using the divergence law the continuity equation becomes:

$$\frac{\partial \rho(x)}{\partial t} + \rho(x)\frac{dv_i(x)}{dx_i} + v_i(x)\frac{d\rho(x)}{dx_i} = 0 \tag{5-2}$$

In fluid mechanics, the fluid comprises material particles that can be compressible or incompressible. However, in solid materials, to a very good approximation, the polycrystalline material can be considered to be an incompressible material, and hence the term $v_{ii} = dv_i / dx_i$ approaches zero; thus we have:

$$\frac{\partial \rho(x)}{\partial t} = -v_i(x)\frac{d\rho(x)}{dx_i} \tag{5-3}$$

This equation is the final form of the MC equation for an incompressible material, and is employed to the mass evolution process for further microstructure analysis.

5.2 Application to a Two-Phase Material

The continuity equation formulated in the previous section can be used to predict the evolution of the MF for a *two-isotropic-phase (TIP)* material. Results of application of the mass-based continuity equation into modeling the microstructure of the TIP material can be found in one of the author's papers (AHMADI *et al.* 2009). As it has been mentioned in this paper, to build a model based upon the continuity equation for the TIP material, the following assumptions must be made: (i) the material under deformation acts like an incompressible media; (ii) the phases do not change from one to the other during the deformation process; (iii) the phases have isotropic properties; and (iv) the motion of phase particles is a continuous process. Following these assumptions, the continuity equation is readily extended from Eq. (5-3) to apply to the MF:

$$\frac{\partial M(x,g^*)}{\partial t} = -v_i(x)\frac{dM(x,g^*)}{dx_i} \tag{5-4}$$

where g^* shows that we have derived the equation for a particular orientation (or phase here). If phase change does not occur during deformation, the MC equation can be expressed for each phase individually. It is assumed that the microstructure is composed of two regions each representing a phase. We will hereafter focus on the continuity equation for the second phase expressed in Cartesian coordinates.

The TIP model is constructed for a plane-strain compression test (similar to rolling). A plane-strain compression test has two planes of symmetry and four distinct regions wherein material particles are symmetrically moving. In this study, the upper right corner of a plane-strain test is sampled. Accordingly, since the plane-strain condition is applied, plastic strain in the 2-direction is assumed to be zero ($\varepsilon_2 = 0$) and based upon the incompressibility condition we will have $\varepsilon_1 = -\varepsilon_3$. Assuming that the macroscopic motion conditions also apply locally

(following the familiar Taylor hypothesis), the equations of motion throughout the material are then simplified to $x_1 = X_1 \exp(\dot{\varepsilon}t)$, $x_2 = X_2$, and $x_3 = X_3 \exp(-\dot{\varepsilon}t)$. Here $\dot{\varepsilon}$ is the applied strain rate, x represents the position of a material particle with respect to a pre-defined Eulerian coordinate system at time t, and X shows the position of that particular material particle at the reference configuration ($t = 0$). Additional information regarding selection of desired boundary conditions is also discussed in (AHMADI *et al.* 2009).

To build the TIP model, (i) the real space is tessellated into small bins (Eulerian system); (ii) the velocity vector is calculated for each Eulerian point for a strain rate of $\dot{\varepsilon} = 0.001 s^{-1}$; (iii) an iteration scheme is designed to monitor the evolution process and obtain the final microstructure. If the plastic deformation is applied in small steps of time we can rewrite the continuity equation as:

$$\frac{\Delta M(x)|_2}{\Delta t} = -v_1(x)\frac{dM(x)|_2}{dx_1} - v_3(x)\frac{dM(x)|_2}{dx_3} \tag{5-5}$$

where the index $|_2$ indicates that we are modeling the evolution of the MF for the second phase. This choice is arbitrary.

In the above equation the only unknown terms are the partial derivatives. To compute these derivatives a *finite difference method (FDM)* is used. It was found that among all the finite difference schemes, forward and backward differences were the best choices. Distinguishing between the usages of forward or backward methods depends upon the sign of the velocity component: if the velocity is positive, the backward difference is preferred; and if it is negative, the forward difference method should be used. An example that can clarify the reasons of choosing this finite difference scheme is provided in Appendix B. When all terms are calculated, the change of the microstructure function at one time step can be calculated from Eq.

(5-5), and the microstructure function at the end of the iteration is calculated by $M_f = M_i + \Delta M$ where ΔM is calculated from Eq. (5-5), assuming that $\Delta t = 1$. For simplicity, it was assumed that the deformation is a steady process with a uniform velocity field that does not change as deformation proceeds. Then, to obtain an exact amount of strain this process is iterated until the total strain is reached. For instance, if we assume that the strain rate is $\dot{\varepsilon} = 0.001$ s^{-1}, to apply a total plastic strain of 10%, the number of iterations will be 100. The final microstructure function is eventually captured from the last iteration.

Results for the MF evolution of the TIP model are demonstrated in Fig. 5-1. Micrograph (a) shows an area (15×15 μm^2) taken from the original microstructure. The microstructure is tessellated into equally-spaced bins with 0.3 μm grid size. The MF at every bin is set to 0 if occupied by phase 1, and 1 if phase 2 fills the bin (if the bin contains a fraction of phase 1 and 2, its MF takes a value based on the fraction of phase 2). MF evolution is progressed using Eq. (5-5) and the iteration scheme just described. The evolution of microstructure for different amounts of total strain is shown in subplots (c-e). It can be seen that as the deformation proceeds, the MF becomes more diffuse near interfaces.

To validate our model for predicting MF evolution, another model can be established that will provide the final microstructure without applying any iteration technique. For this model, which has a Lagrangian basis, about 100 points were thrown randomly into every bin in the initial microstructure. These points are labeled as phase 1 or 2 based on their original location. If the final amount of applied strain is known, the number of total iterations is also determined; then, the final location of points can be determined using the equations of motion. For example, if we take a point at position $(2,0,2)$ and if it is desired to apply 10% strain at the rate of $\dot{\varepsilon} = 0.001 s^{-1}$, 100 iterations are required. Based upon the equations of motion, this point at the

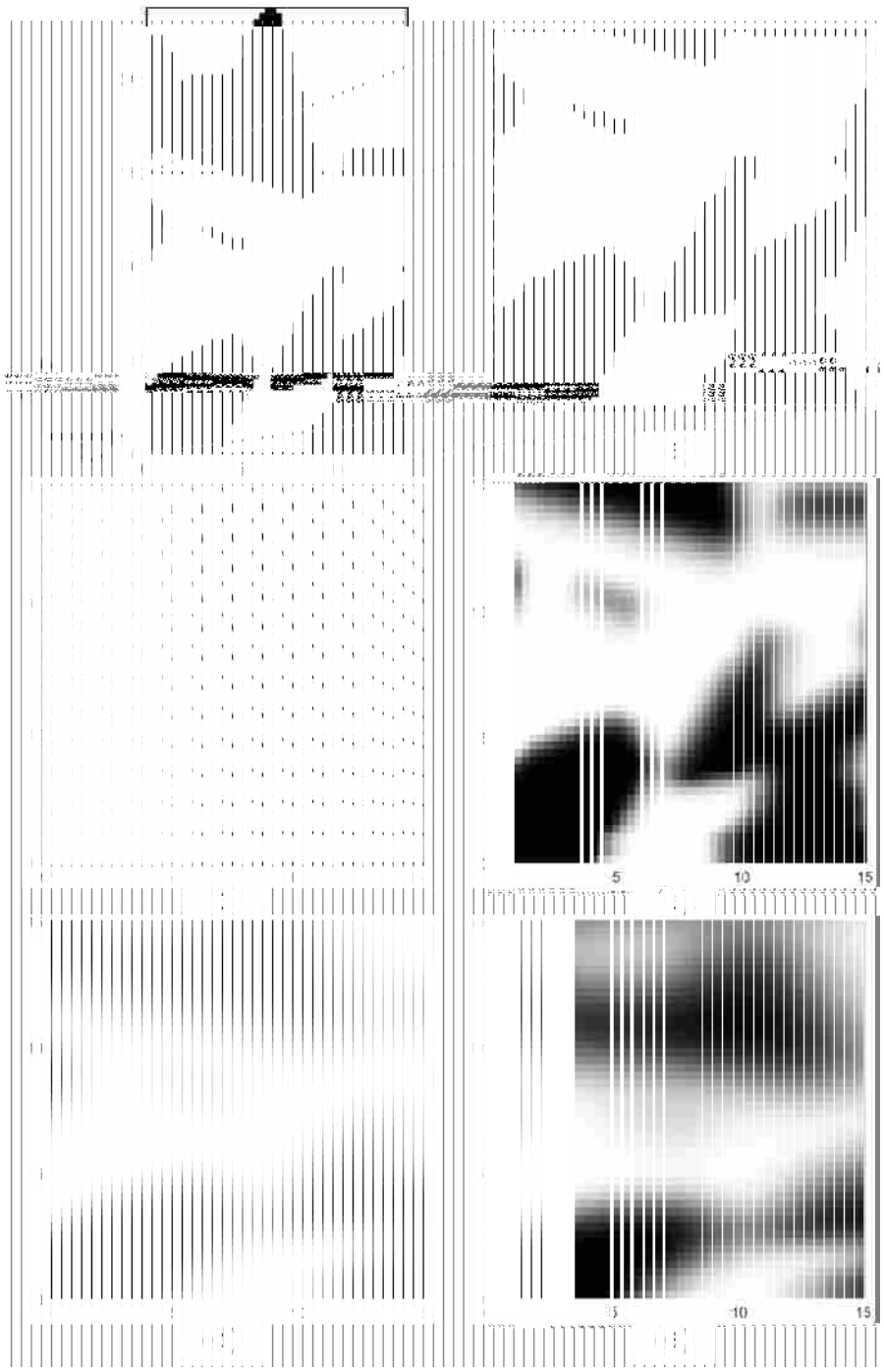

Fig. 5-1: MF evolution under plane strain conditions for the two phase model (white: phase 1; black: phase 2). (a) initial MF; (b) velocity field for the plane strain condition; (c, d, and e) MF evolution after 10%, 30%, and 50% total strain.

end of process is located at $(2.21,0,1.81)$, because e.g. $x_1 = 2\exp(0.001 \times 100) = 2.21$. The labeled points were forced to move directly using the equations of motion. The final MF then was calculated for each Eulerian bin by finding the fraction of the number of points belonging to phase 2 relative to the number of all points occupying that bin. A comparison of final microstructure predicted by the continuity relations and the second (direct) model, is illustrated in Fig. 5-2 (a and b).

The 2-point correlation function between phase 1 and 2, $f_2(1,2|\vec{r})$ was also computed using FFTs; for more information regarding the implementation of FFTs in manipulating the 2-point functions the reader is referred to the work of Fullwood et al. (FULLWOOD *et al.* 2008). The f_2 plots for both models are shown in Fig. 5-2 (c and d). For better visualization, the f_2 plots are centered throughout this thesis. The origin of the vector $\vec{r}$ is, therefore, placed at the center of f_2 plots. As an example, in Fig. 5-2 (c and d), the value of $f_2(1,2|\vec{r})$ when $\vec{r}$ is small is very small, this means that the correlation between the two phases at distance and direction of $\vec{r} \approx \vec{0}$ is very low. Or, in another word, the probability of finding the two phases at $\vec{r} \approx \vec{0}$ from each other is very low. This is true because at very small $\vec{r}$, most of the vectors land in the same phase and the correlation of phase 1 and phase 2 is very low, or as $\vec{r} \to \vec{0}$, $f_2(1,2|\vec{r}) \to 0$.

In the microstructure predicted by the continuity relations, some spreading of the second phase (similar to a diffusion phenomenon) can be seen on the boundaries. The smearing happens during the iteration scheme. It initiates from the use of finite difference methods. This is because there is not an explicit way to calculate partial derivatives in Eq. (5-5), and using first-order finite differences gives an error of the order of the bin size at every step of deformation. This error accumulates with the number of calculation steps, and results in a thicker smeared boundary layer as a function of the number of iterations. The extent of these errors depends upon the

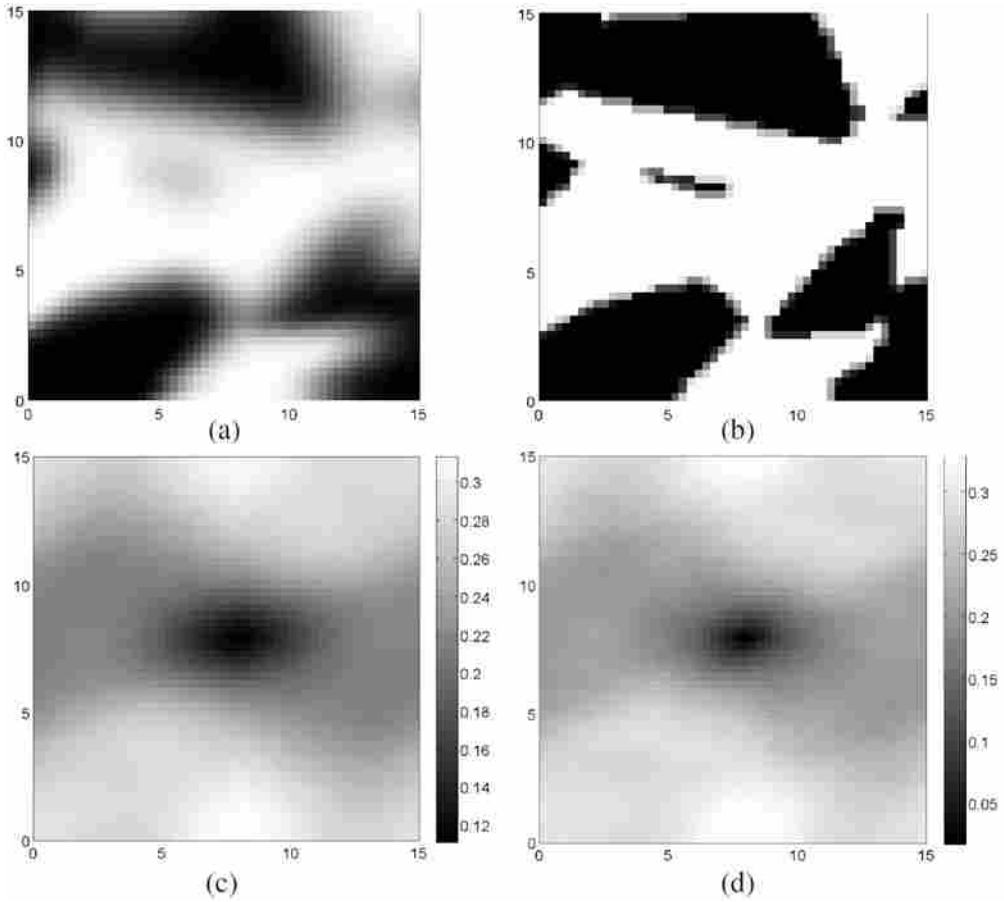

Fig. 5-2: MF evolution for 30% total plastic strain predicted by (a) continuity relations; (b) the direct (Taylor) model. 2-point correlation function plots for (a) continuity relations (b) the direct model.

number of iterations and the bin size. This smearing effect is quite obvious in Fig. 5-1(c-e) where different amounts of strain are applied.

The effect of binning size on the accuracy of the continuity model was also studied, Fig. 5-3. A variety of grid sizes were chosen from 0.3 to 0.0375 microns, and the original microstructure was placed under total strain of 30% in 300 iterations. One can see that choosing smaller grids will help to enhance the resolution and reduce the effect of boundary spreading.

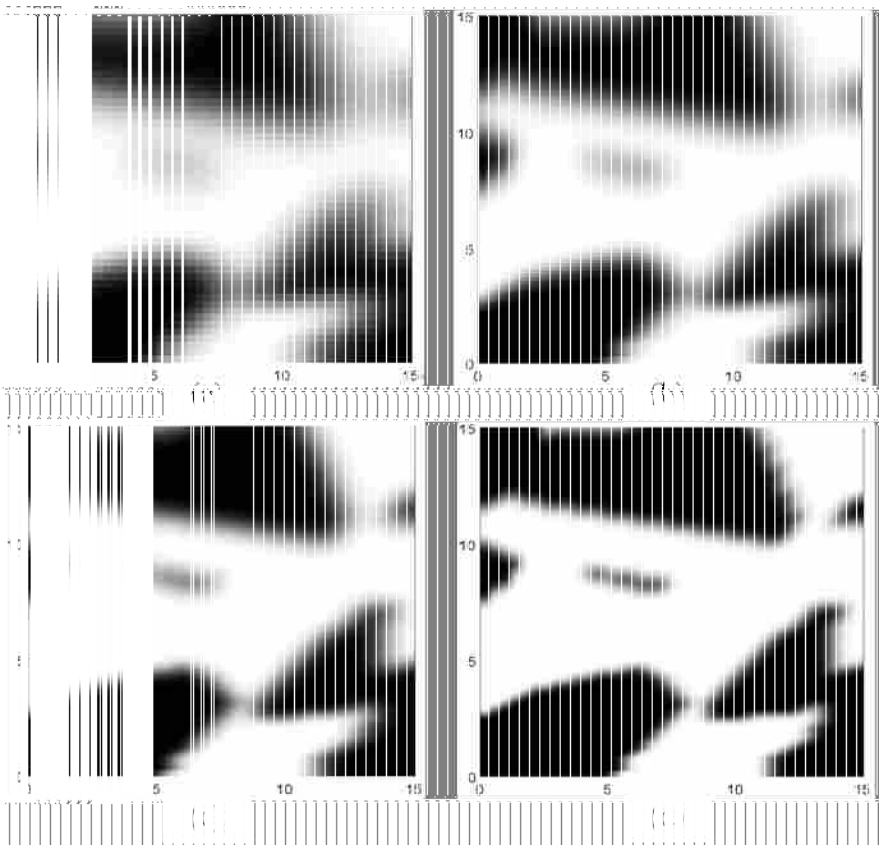

Fig. 5-3: MF after 30% total plastic strain with different grid sizes: (a) 0.3; (b) 0.15; (c) 0.075; (d) 0.0375 microns.

Fig. 5-4 shows error plots (for two different mesh sizes) representing the absolute error between the f_2 obtained from the continuity-based and the direct models. From Fig. 5-4 (a), which illustrates the error plot for operating the continuity model with 0.3 micron bin size, it can be observed that the maximum absolute error for 30% total strain is about 9.4 %. This maximum error occurs for small vectors r which samples the area between the two phases, or the boundaries. If we neglect the smearing effect on the boundaries, the mean absolute errors is about 0.8% which is reasonably acceptable. The second micrograph in Fig. 5-4 demonstrates the error plot for when the continuity model operates with grid sizes of 0.075 microns. Evidently, smaller grid size minimizes the spreading effect, obtaining a maximum absolute error of ~5.6%

which is smaller by a factor of two as compared to subplot (a). Therefore, it is concluded that if the effect of boundary spreading somehow is resolved, the continuity model can provide precise predictions of MF evolution under large deformations. Control of boundary layer thickness can be addressed by either choosing a smaller grid size or applying fewer iterations (with larger strain applied in each step). On the other hand, there is a limit on the maximum amount of strain that can be applied in one time step. It can be shown that the maximum strain needs to be consistent with the limit that $V_i \Delta t \le d$ where d is the bin size. The velocity field in this study is steady; hence it can be shown that as the time step increases, the binning size has to increase as well. Therefore, only one parameter remains that can control the process, which is the bin size.

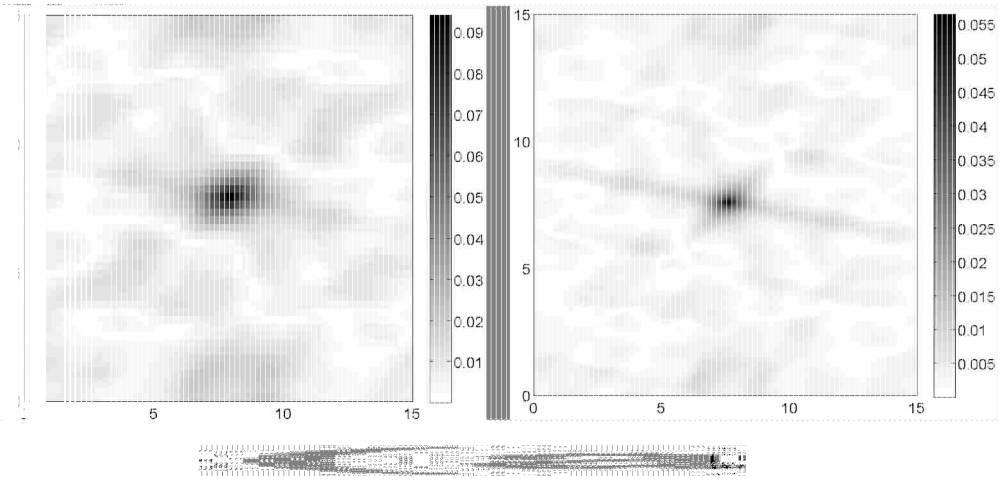

Fig. 5-4: Error plot showing the absolute error of the 2-point correlation functions. The continuity model with (a) 0.3 and (b) 0.075 micron grid size is compared against the direct model.

Table 5-1 also shows the binning effect on the resolution and the time of process. Calculations were conducted on a standard PC. Taking smaller grid size increases processing time dramatically, but produces less error. The times shown in here are for a 2-D model; it is

anticipated that a 3D model would demonstrate a significant amplification of the trend in calculation times.

Table 5-1: Effect of binning size on the accuracy of the proposed model.

Mesh size (μm)	0.3	0.15	0.075	0.0375
Maximum Absolute Error (%)	9.39	7.49	5.64	4.01
Mean Absolute Error (%)	0.79	0.48	0.27	0.13
Calculation Time (s)	3	8	19	52

A desired case of selection of bin size should be taken to achieve good resolution with a reasonable error and an acceptable processing time. From Table 5-1, it can be observed that selecting a grid size of about 0.075 microns results in an appropriate simulation time with ~0.27% mean error.

The MC model that was formulated and verified in this chapter will be used later in Chapter 7 to model the microstructure changes of a nickel polycrystal. Results from this chapter suggest that to use the Eulerian format of the MC model, special care should be dedicated to selecting a preferred Eulerian mesh size whereby less computational error and shorter calculation time are achieved. A reasonably suitable mesh size was determined to be 0.075 microns.

6 ROTATIONS AND THE ORIENTATION EVOLUTION

In the orientation space, we deal with rotations and lattice orientations. There have been many investigations on the evolution of grain orientations or the texture evolution of polycrystalline materials. The main tool that has been used in the literature to quantify the crystallographic texture of material points in the microstructure, as discussed in Section 2.2, is the ODF. In this chapter, first, the principles of the conservation of orientations and the orientation-based continuity (OC) equation is provided, and secondly, an example of employing the OC equation, that has been formulated in the Eulerian framework, into texture predictions of a randomly textured FCC material is given.

6.1 Conservation of Orientation Principle

Similar to the conservation of mass principle in the real space, the conservation of orientation is also suitable in the orientation space. The continuity equation for orientations was first proposed by Clement and Coulomb (CLEMENT 1982; COULOMB 1979):

$$\frac{\partial f}{\partial t} + div(fw) = 0 \tag{6-1}$$

where f is the ODF and w is the velocity vector in the orientation space. This equation is similar to the continuity equation in the mass space (Eq. (5-1)), and it guarantees the principle of conservation of orientations, meaning that crystallite orientations are neither created nor

destroyed during plastic deformation of polycrystals. An Eulerian representation of the OC equation is presented in Appendix C assuming that the working space is the EAS. This derivation is proposed based on presuming the EAS to be a Riemannian Manifold (In fact, the EAS can be expressed in either a Euclidean space or a Riemannian Manifold. A Riemannian manifold is a differential manifold on which a smooth field of symmetric and positive definite metric tensor is specified (HICKS 1965; MORAWIEC 2004)). The divergence in the continuity equation can be formulated using the covariant derivative and Christoffel symbols. The final form of the continuity equation can be expressed for the EAS as (Eq. (C-9) in Appendix C):

$$\frac{\partial f(g)}{\partial t} = -f(g)\frac{\partial w_i(g)}{\partial g_i} - w_i(g)\frac{\partial f(g)}{\partial g_i} - f(g)\cot\Phi w_2(g) \tag{6-2}$$

The first term on the right hand side represents the rate of change of the velocity vector in the EAS. Although we have an incompressible material in the real space and this term in the formulation of MC equation was zero, the flow of orientations in the EAS is compressible and we should treat rotations of orientations as a compressible fluid process. Similar to the continuity equation in the mass space, finite difference methods can be used to compute the partial derivatives in Eq. (6-2). To find the velocity vector, w , and the rotation rate field in the EAS, various plasticity models can be used. The binning process is similar to the discertization scheme applied to the mass space. The EAS is tessellated into a small size Eulerian grid. The center point of each bin is then taken as the Eulerian point and the velocity vector is calculated for all bins in the Euler angle domain.

The OC equation, Eq. (6-2), has been used to find the evolution of the ODF, *f(g)*. Following a process similar to our formulation in the mass space, Eq. (6-2) can be rearranged to describe the evolution of the MF for a specific material point x:

$$\frac{\partial M(g)}{\partial t}|_x = -M(g)|_x \frac{\partial w_i(g)|_x}{\partial g_i} - w_i(g)|_x \frac{\partial M(g)|_x}{\partial g_i} - M(g)|_x \cot \Phi w_2(g)|_x \qquad (6\text{-}3)$$

This equation can be used to find the evolution of the MF at every material point x.

6.2 Application to a Randomly Textured Material

The Eulerian formulation of the continuity equation in the EAS was presented in the previous section. In this section, an example of obtaining the lattice rotation field (see Section 4.3) and rotation of orientations under this field is explained. To find the velocity terms presented in Eq. (6-3), the TLVP crystal plasticity model (explained in Section 3.2.4) was used to find the lattice spin tensor. The parameters appearing in the TLVP model are taken as: $\dot{\gamma}_0 = 0.001 \sec^{-1}$, $m = 0.012$, and $\tau^* = 35 MPa$. For simplicity, it is further assumed (i) that the critical resolved shear stress is identical for all slip systems; and (ii) that the material is deformed under a rigid-perfectly-plastic condition without taking into account any slip hardening effects (slip hardening parameters are specified from mechanical testing and the effects of slip hardening on the orientation changes are studied in the next chapter).

Simplified rolling process (e.g. taking a plane-strain compression condition) was modeled to find the evolution of orientations in a randomly textured microstructure. Two different models were studied: (1) A Lagrangian model with an iteration scheme was constructed such that orientations at the end of each iteration were updated simply by summing up the amount of rotation caused by the lattice spins (Section 3.2.1). In this way if we take the original orientation as g_i then the final orientation at the end of current iteration is obtained by $g_f = g_i + w.\Delta t$; (2) An Eulerian formulation that was expressed in the previous section, along with the iteration scheme that was introduced for the mass-based continuity equation was also examined. In this

case, to obtain the velocity field the cubic-orthorhombic fundamental zone, $FZ_{3C/4}$, which was described in Section 4.1 was tessellated into small cubic bins. Lattice rotations were calculated for centers of bins. After obtaining the velocity field, every orientation of the microstructure was placed into this field and the movement of the orientation was monitored by an iteration scheme (similar to the mass-based iteration scheme).

To validate the Eulerian model, a comparison against a Lagrangian model was performed. The comparison model selected is that used in most crystal-plastic FEM analyses – e.g. (KALIDINDI and ANAND 1992; KALIDINDI and ANAND 1994; KALIDINDI *et al.* 1992). Evolution of the texture of a randomly textured microstructure with 1000 random orientations is studied with both models. These orientations are randomly taken from $FZ_{3C/4}$. The chosen microstructure was assumed to be rolled to a final reduction of 70%. Using the Lagrangian model, as it was explained, is straight forward. To employ the Eulerian model these steps were followed:

1- One orientation is studied at a time. The selected orientation is located in the conventional $FZ_{3C/4}$ and a cubical region of 20×20×20 degrees is taken around the chosen orientation. The MF for this cube is set at 1 for the bin that contains the orientation and 0 everywhere else.

2- In addition to the velocity field, partial derivatives and all the terms presented in Eq. (6-3) are determined for the surrounding cube. A finite difference scheme similar to the one introduced for the mass space is also employed here to find the evolution of the microstructure function.

3- To have an efficient model, the deformation process is subdivided into small increments in which 5% strain is applied in 500 time steps. At every time step, 0.1% true strain is

applied; then, the rate change of the MF is calculated and added up to the current value of the MF. This iterative process continues until it reaches the limit of 5%. This gives one increment of the deformation equivalent to a true strain of 5%. Because we use FDM in the iterative scheme, similar to the mass problem, smearing of the MF will occur; therefore, a cleaning process was designed such that the bin having the maximum value of MF is taken as the final rotated orientation after 5% strain.

4- To apply further amounts of rolling deformation a new cube is taken around the updated orientation and previous steps (step 1-3) are repeated until the desired amount of deformation is reached. The final strain for applying 70% rolling reduction is ~120%; this amount of deformation is applied in 24 deformation increments. During this iterative process it must be anticipated that some of the orientations fall out of $FZ_{3C/4}$, for such cases the related crystal- and sample-symmetry operators are used to map the orientation back into $FZ_{3C/4}$ after which the process continues on.

To statistically analyze results from Lagrangian and Eulerian models (200) and (111) pole figures were constructed. A Gaussian distribution with a half-scatter width of 5°, and orthorhombic sample symmetry was used in calculations of pole plots. All pole figures presented here are equal area projections of the specified crystallographic poles. Fig. 6-1 shows the pole figures calculated for the randomly textured microstructure. Weak intensities in the pole plots verify that the microstructure is randomly textured.

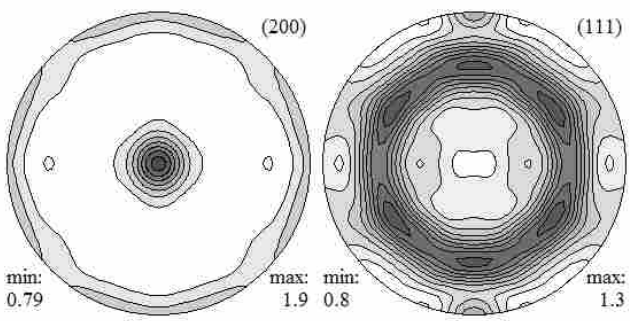

Fig. 6-1: (200) and (111) pole plots calculated for the randomly textured microstructure

The Lagrangian and Eulerian models were later used to predict the evolution of the texture of this microstructure. The pole figures predicted by the Lagrangian model are illustrated in Fig. 6-2 (a). To study the effect of binning size, the Eulerian continuity model with three different grid sizes was used. Fig. 6-2 (subplots b-d) is showing the binning effects for bin sizes of 1, 0.5, and 0.25 degrees, respectively.

From Fig. 6-2, it obviously can be seen that the Eulerian model can quantitatively give reasonable predictions of texture evolution (it can predict the locations of the high intensity peaks); however, because the pole plots predicted by larger mesh sizes show lower intensities compared to the ones predicted by the Lagrangian model, we suspect that the application of the Eulerian continuity model with too large mesh sizes may not adequately predict the quantitative details of texture evolution. Conversely, by decreasing the mesh size and taking smaller bins in $FZ_{3C/4}$, the resolution of the continuity model is increased.

In addition to the resolution effect, the computation time is also an important consideration. It can be shown that the algorithms of the Eulerian continuity model are more time-efficient. The total time spent for employing the Lagrangian model to simulate the 70% rolled macrostructure was ~7.5 hours on a standard PC. This time is mostly spent to find a

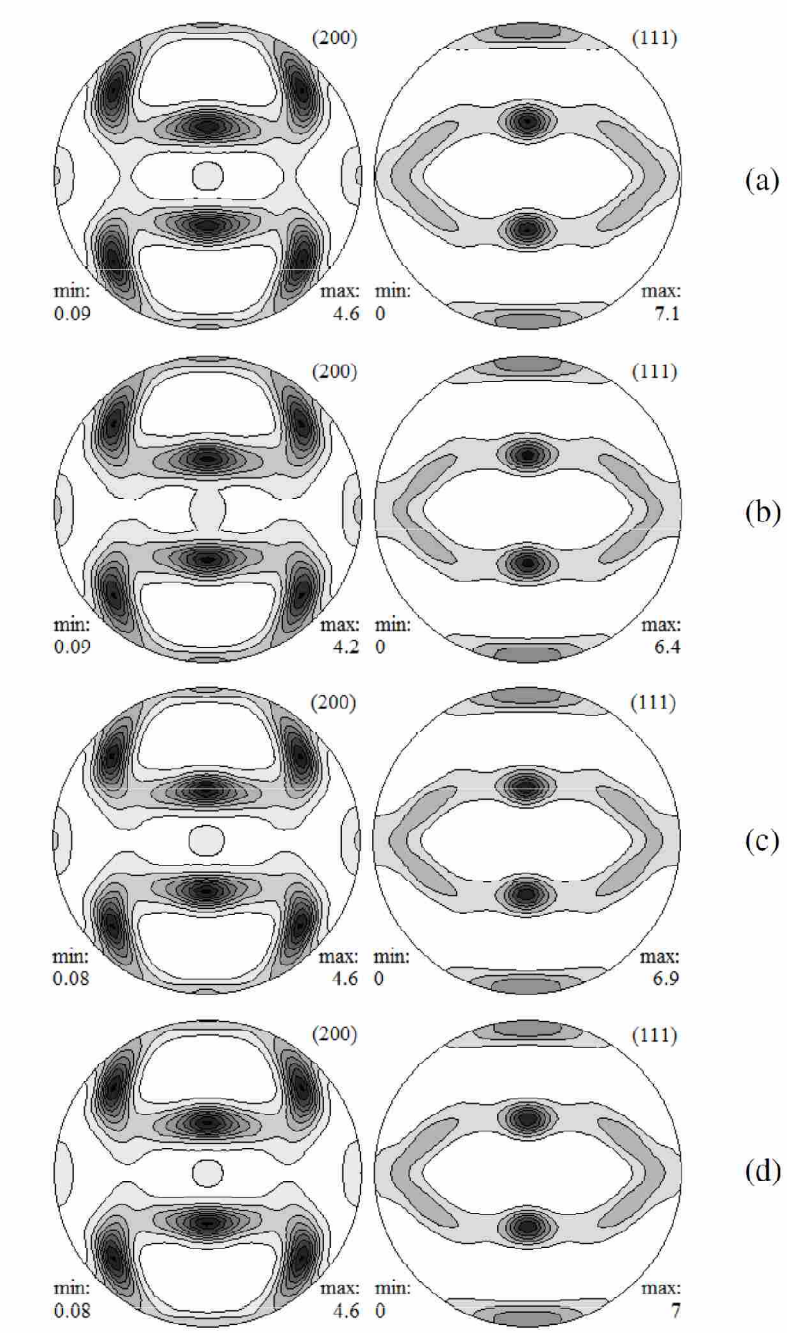

Fig. 6-2: (200) and (111) pole plots predicted by: (a) Lagrangian model; Eulerian model with binning sizes of (b) 1 degree; (c) 0.5 degrees, and (d) 0.25 degrees.

solution for the nonlinear power-law equation (Eq. (3-9)) using a Newton-Raphson scheme (e.g. (FROMM *et al.* 2009)) and to calculate the lattice spins. At each iteration, 0.1% strain is applied;

therefore, there are 1000 orientations and 1.2/0.001=1200 iterations, which means that this nonlinear equation must be solved 1,200,000 times for this particular microstructure (if another microstructure is modeled all these calculations must be retaken). However, in using the Eulerian continuity model to build the rotation rate field, $FZ_{3C/4}$ is tessellated into 2 degree bins and the nonlinear equation is generally calculated 45×45×45=91,125 times. If taking a smaller mesh size is desired, due to the fact that the rotation rate field is a continuous field and velocity terms are gradually changing from one bin to the other, we can take the midpoint of two adjacent grid points as the new point and the average velocities of the adjacent points can be assigned as its velocity. Total calculation time to construct the velocity field with 2 degree mesh size is ~36 minutes. This calculation is carried out only once and the velocity field is valid for simulating cold rolling of all types of FCC materials. In addition to this calculation time we should also include the time that is needed to update the MF by the iteration scheme, as explained earlier. Table 6-1, shows this calculation time and the amount of error that appeared from using the Eulerian continuity model compared to the Lagrangian model.

Table 6-1: Effects of binning size on the accuracy and calculation time of the OC model

Mesh size (degree)	1	0.5	0.25
Maximum Absolute Error (degree)	11.31	6.43	4.79
Mean Absolute Error (degree)	1.78	0.97	0.83
Calculation Time (min)	8	46	115

From Fig. 6-2 and Table 6-1, it can be concluded that a mesh size of 0.5 degrees is acceptable since the average absolute error is less than 1 degree and the overall time (including the time required to compute the rotation rate field) is reasonable: ~82 minutes. This

computational time is a factor of ~5.5 less than the time spent in calculations by the Lagrangian model.

Now that the Eulerian format of the OC equation has been modeled and also corroborated against the familiar Lagrangian models, and reasonable results were obtained, we can go one step further and by linking the MC and OC models; then, the evolution of the microstructure of polycrystalline nickel can be examined. The accuracy of the coupled model can be confirmed when this model is compared against experimental testing, as it will be the aim in the next chapter.

7 EULERIAN-BASED DOUBLE CONTINUITY MODEL AND ITS APPLICATIONS

To model the evolution of the MF throughout a plastic deformation process, the evolution of position and orientation of crystallographic grains is considered. As discussed in Chapters 5 and 6, the movement of mass particles of grains is monitored by the MC model in the mass space, and the orientation change of grains is monitored by the OC model in the EAS. The aim of this chapter is to link the MC and OC models and develop a coupled model that can be used to examine the microstructure evolution of real polycrystalline materials. A fully annealed polycrystalline nickel sample is, additionally, used to validate the numerical results from the simulation of the rolling process by the coupled model. Moreover, textural and statistical comparisons of experimental and simulated microstructures are considered. For the textural analyses, ideal orientations of rolling for both empirical and numerical microstructures are studied with pole figures, ODF sections, and fibre plots. On the statistical analyses, correlations of ideal orientations are examined using the 2-point correlation functions. In addition, coherence and anti-coherence lengths are measured, and their relationship to the amount of cold work is examined.

7.1 Experimental Procedures and Results

In order to validate the numerical approach, some experimental tests were performed. A commercial purity nickel (99.9 %wt) was used in this investigation. Reasons for selecting nickel

as the working material are: (i) nickel is an FCC material having a sufficient number of potentially active slip systems (12 possible slip systems) to readily accommodate an arbitrary state of local plastic strain; (ii) nickel has a medium SFE, $128\ mJm^{-2}$, and as it can be found in the literature, deformation twinning does not occur in FCC materials with medium or high SFE, making the texture prediction of these materials much simpler. (iii) Taylor-type models can qualitatively predict the texture of medium and high SFE materials.

7.1.1 Tensile Testing

In the development of our new Eulerian model in Section 3.2, it was mentioned that the TLVP model is chosen to obtain the lattice rotation rate field. To calibrate the TLVP model and also to obtain the slip hardening parameters tensile tests with different conditions were conducted.

First, to calculate the mechanical properties of the material three medium-size tensile samples were cut and prepared based on the ASTM E8/E8M standard (ASTM 2003). Samples were then pulled using a MTS-661 machine at a strain rate of $0.001\ sec^{-1}$. Stress-strain curves were depicted and mechanical properties of the material were obtained by conventional analysis (Table 7-1).

Table 7-1: Mechanical properties measured from tensile testing of commercially pure Nickel

Young's Modulus	Yield Strength	Ultimate Tensile Strength	Total Elongation
201 GPa	245 MPa	414 MPa	62.3 %

Furthermore, to obtain the rate sensitivity parameter, m, which is used in the power-law viscoplasticity relation, Eq. (3-6), three additional samples were pulled at the faster 0.01 sec^{-1}

strain rate. Thus, a total of six samples were strained under two different strain rates. Averaged engineering stress-strain curves for each set of samples were measured and plotted in Fig. 7-1.

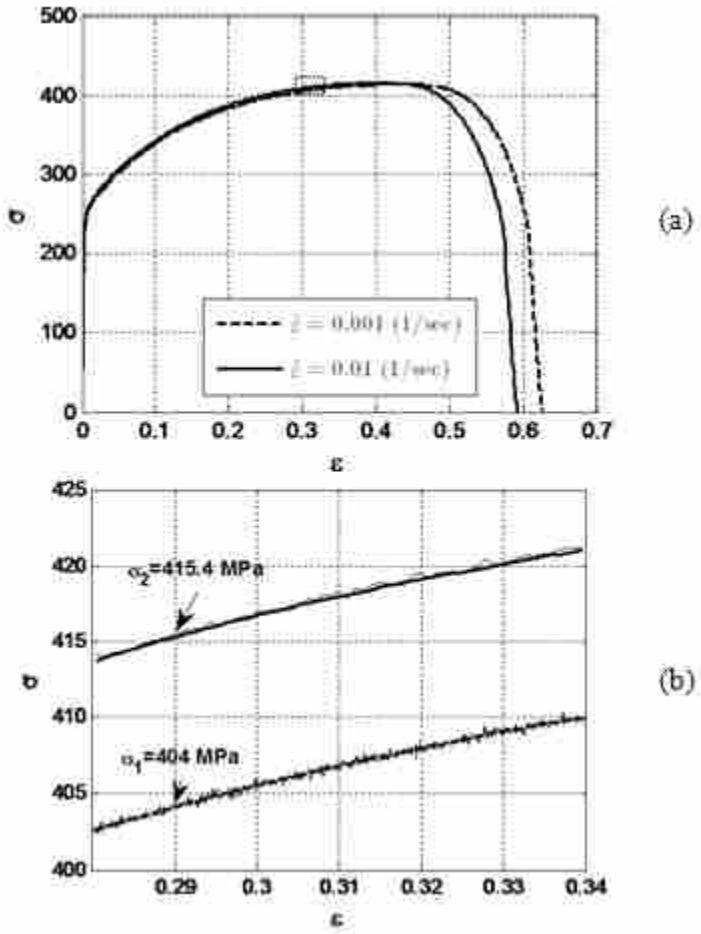

Fig. 7-1: (a) two sets of stress-strain curves with different strain rates; (b) magnified area selected to find the rate sensitivity parameter.

The rate sensitivity parameter was calculated from the difference of the curves by fitting the best curve for each set of samples, finding the stress differences in the entire selected area, and using the following equation (HOSFORD and CADDELL 2007):

$$m = \ln(\sigma_2 / \sigma_1) / \ln(\dot{\varepsilon}_2 / \dot{\varepsilon}_1) \tag{7-1}$$

The rate sensitivity parameter, *m*, was calculated for a range of strain, 0.15-0.35, with a strain increment of 0.02. An example of calculating *m* is shown in Fig. 7-1 (b) for a strain value of 0.29. If Eq. (7-1) is used at this point, the rate sensitivity parameter is measured as 0.0121. By averaging the calculated *m* for the entire range, the average *m* is measured as *0.012*.

Slip hardening parameters can be calculated from the stress-strain data as well. If we take the original microstructure of the material and use the TLVP model, the stress-strain curve can be predicted by updating the slip resistance in Eq. (3-9) using the saturation-type slip hardening model discussed in Section 3.2.3, Eq. (3-12). The four slip hardening parameters that are used in Eq. (3-12), can be chosen such that the predicted stress-strain curve is well fitted to the experimentally measured one. The measured slip hardening parameters are: $\tau_0^* = 83\,MPa$, $h_0 = 445$, $s_s = 134$, $a = 1.08$. Fig. 7-2 also shows the predicted curve that has been calculated to the maximum strain of 0.4 for the original microstructure including 746 grains. A Lagrangian model was used to update the slip resistance at every level of strain.

7.1.2 Rolling Process

To validate the numerical model that we have developed in this research a specific mechanical process should be chosen such that it enables us to study large levels of plastic deformations. Among all deformation processes, rolling is a process by which a wide range of strain can be applied incrementally (mathematically strain can even approach infinity when the final thickness of the sheet approaches zero). Also, modeling the rolling process is very straightforward, since it is well-approximated to be simple plane-strain compression. In this research, sample sheets of pure nickel with initial thickness of 9.9mm, were rolled down to

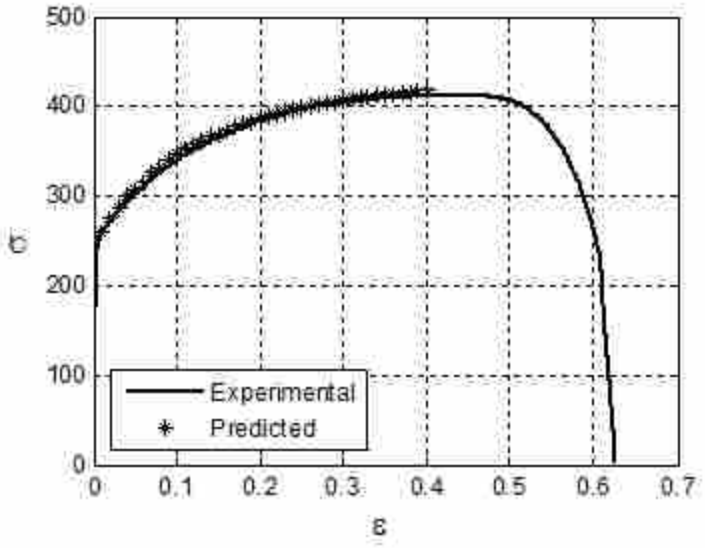

Fig. 7-2: Experimental and simulated stress-strain curves for pure nickel

several different thicknesses. Table 7-2 shows the property of these samples labeled based on the amount of their rolling reductions. The rolling reduction, R, can be calculated from the initial, t_0, and the final, t, thicknesses: $R = 1 - t/t_0$. This table also provides the amount of the rolling deformation, $\varepsilon_0 = \ln(t_0/t)$, and the equivalent von Mises strain, $\varepsilon_{vM} = {}^{2}/_{\sqrt{3}}\,\varepsilon_0$.

Table 7-2: Rolled samples labeled based on the amount of cold work (%)

Label	0%	30%	50%	70%	85%	92%
Rolling reduction (%)		30.3	50.4	70.0	84.8	92.3
Rolling deformation	As received	0.36	0.70	1.20	1.88	2.53
von Mises strain		0.42	0.81	1.39	2.18	2.92

After the samples were cold rolled and sized to proper reductions, an oblique sectioning technique was used to sample the microstructures in a statistically-unbiased way. From each set

of labeled material, three samples with different sample plane-normals (sections with plane-normals parallel to the ND, TD, and RD directions) were cut and prepared for the microscopy examination.

Orientation image microscopy (OIM) was used to scan the samples and recover the microstructure. To scan the samples, a Philips XL30 S-FEG scanning electron microscope (SEM) equipped with a fully automated electron backscatter diffraction (EBSD) analysis system, was used. Orientation maps were obtained for areas 700×700 μm^2 using a step size of 2 microns. Inverse pole figure maps of samples with different amounts of cold-rolling are illustrated in Fig. 7-3. These micrographs are taken from sections that have their normal vectors parallel to the ND of the rolled sample.

7.1.3 Reconstruction Process

The inverse pole figure maps that were illustrated in the previous section are two-dimensional OIM maps. In order to get a statistically reasonable microstructure that can be used to sample the entire microstructure we need a 3D microstructure that shows the statistics and complete shape of grains in the microstructure. A 3D simulated microstructure that has been developed using the Potts model, provided by Prof. A.D. Rollett's group at Carnegie Mellon University, is used in this research. Grains in this microstructure are identified by their ID number. To use the 3D microstructure in the simulations, for every grain in the microstructure a desired orientation must be assigned such that the 3D microstructure becomes statistically equivalent to the original microstructure of as-received material. The orientation distribution function and the 2-point correlation function that were introduced in Section 2.2 can be used to capture the statistics of both microstructures.

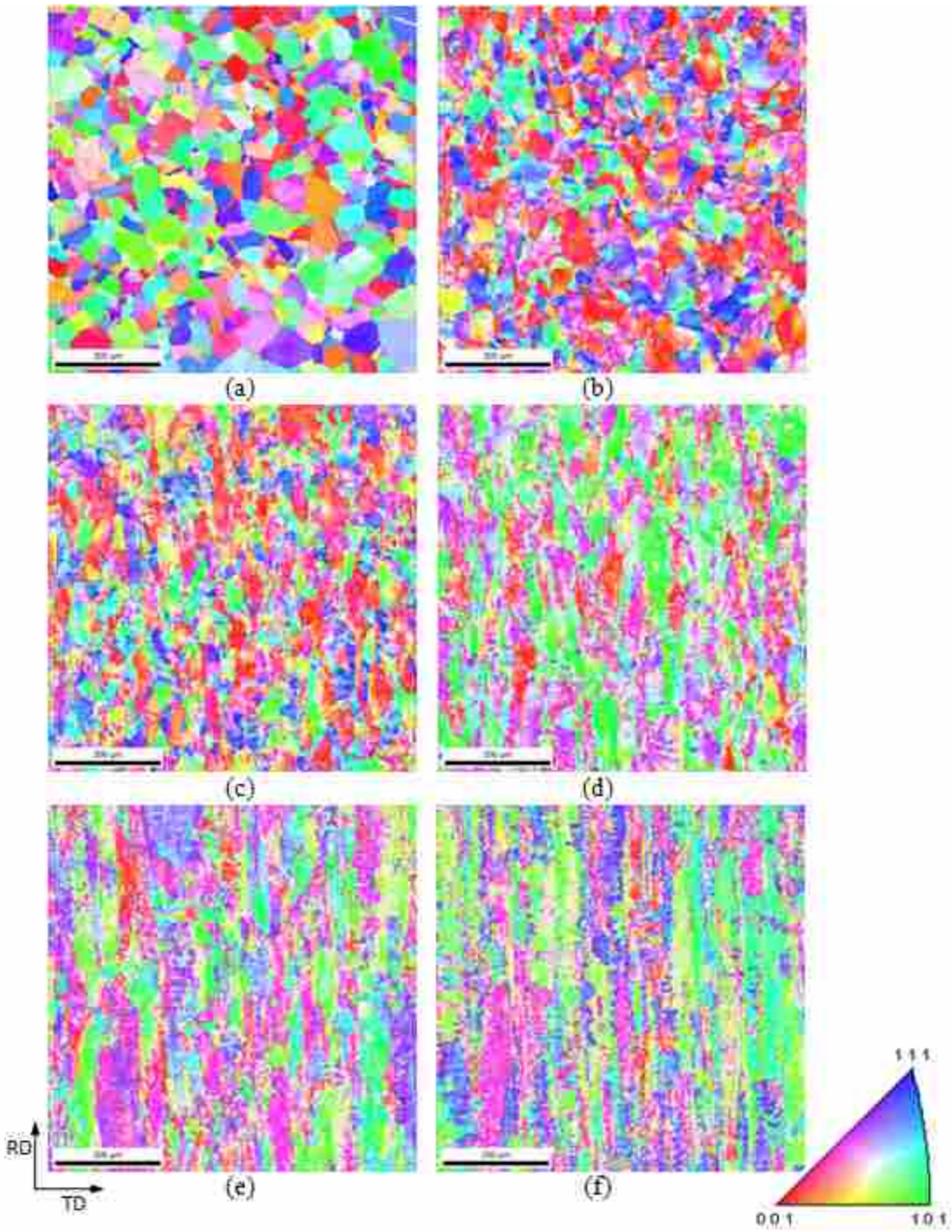

Fig. 7-3: Inverse pole figure maps for (a) as-received sample; and (b-f) samples cold-rolled to reductions of 30, 50, 70, 85, and 92 %, respectively. Samples are cut from the ND plane.

To assign orientations into grains in the simulated 3D microstructure two possible methods can be selected: (i) Randomly assign orientations into grains, obtain the 1- and 2 point statistics of the microstructure, and find out how close the current configuration predicts the statistics of the empirical microstructure (an error function, which can be considerably minimized, is used to obtain more accurate results). Since we are dealing with a large number of grains (1712 grains in the 3D microstructure) there are many possible permutations (1712!) and the probability of finding a reasonable solution is very low for this method; (ii) A second process of finding statistical functions is similar to method (i) except that a preferred minimization technique (e.g. *simulated annealing* or *genetic algorithm*) is used to minimize the error function. To technically reconstruct the 3D microstructure, a genetic algorithm (GA) scheme was used in this research. Therefore, to reconstruct the microstructure, based on the GA method, the following steps were taken:

- Three sections (RD, TD, and ND planes) of the original material were scanned. Orientation maps and grains information were obtained using the OIM software. Orientation maps were placed in the proper global coordinate system (see Section 4.1), and orientations were recalculated based on the current system. Additionally, using the mean linear intercept method, the average grain size in different sections was measured as: 18.42, 17.86, and 20.30 microns for RD, TD, and ND sections, respectively. Also, the overall average grain size, which is the mean value of grain sizes in all three sections, was measured as of $Avgd1=18.86\ \mu m$. This value was used later to scale the 3D microstructure.

- It was found that the as-received material has a texture exhibiting orthorhombic sample symmetry. Thus, orientations were mapped into the reduced $FZ_{3C/4}$. The reduced $FZ_{3C/4}$ was tessellated (5 degree resolution) and the ODF was then calculated.
- Five orientations that have the highest intensities in the ODF were chosen and the 2-point correlation function between each pair of these orientations (i.e. $f_{12}, f_{13}, \ldots, f_{23}, \ldots$) was calculated. Note that f_{11} is the ODF of orientation 1.
- Average grain size for the 3D microstructure was measured in ten slices of three different sections. The average grain size in RD, TD, and ND sections were measured as 14.96, 15.12, and 14.91, respectively. The overall average grain size was also measured as *Avgd2=15 μm*, and compared with the one obtained for the original microstructure. A scaling factor was defined as *Avgd1/Avgd2=1.257* to scale the 3D microstructure. The 3D reconstructed microstructure was then scaled to have similar average grain size for both empirical and reconstructed microstructures.
- The ODF and 2-point correlation functions calculated from both microstructures should then be compared, and an error function should be provided to find the accuracy of the reconstruction process. This error function was defined to be:

$$f_{error} = \sum_{i=1}^{5}\sum_{j=1}^{5}(f_{ij}|_{exp.} - f_{ij}|_{guess})^2 + \sum_{i}(f_{ii}|_{exp.} - f_{ii}|_{guess})^2 \qquad (7\text{-}2)$$

- To start the reconstruction process using the GA method, a random permutation of the microstructure was initially selected, and afterwards, the GA method was used to find a solution by which the error function is minimized considerably. The process was stopped when the mean error was less than 1% or when the number of generations exceeded

200,000 iterations. Fig. 7-4 is a flowchart demonstrating how the GA algorithm can be used in the reconstruction process.

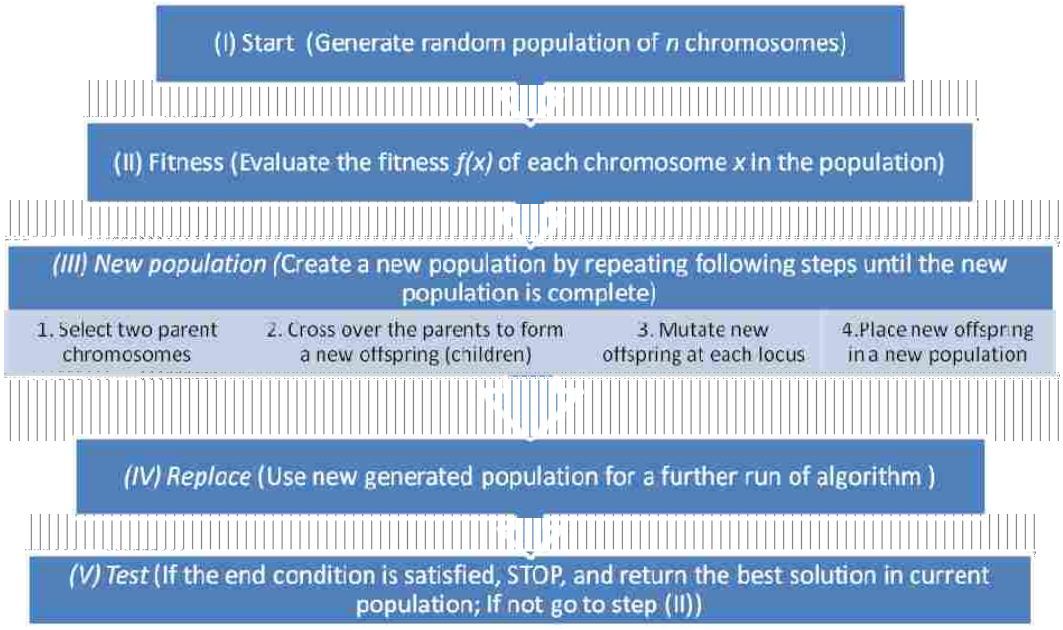

Fig. 7-4: Outline of the Basic Genetic Algorithm

As illustrated above, the fitness function in the GA algorithm is the error function that we are trying to minimize here. Other parameters that were used in the GA method are as follows: (1) *Search space*, which was selected to be a vector of ID numbers of all grains in the 3D microstructure in this research; (2) *Crossover probability*, which quantifies how often crossover (switching of a portion of two parent chromosomes to generate new offspring) will be performed. In this optimization process, this parameter was selected to be 70%. If there is no crossover, the offspring are an exact copy of the parents. If the crossover probability is 100%, then all offspring are altered by crossover; (3) *Mutation probability*, which represents how often

the chromosome is mutated. If there is no mutation (0%), the offspring are taken after crossover (or copy) without any change. If mutation is performed, part of the chromosome is changed. In our minimization scheme, a mutation probability of 3% was chosen; (4) *Population size*, which tells us the number of chromosomes in the population (in one generation). This parameter was selected to be 50 chromosomes for an optimum instance. It is reported that if there are too few chromosomes in the population, GA has a few possibilities to perform crossover and only a small part of search space is explored. On the other hand, if there are too many chromosomes, the GA slows down. Additional information regarding the usage of GA can be found in (MITCHELL 1996).

The GA minimization method was run to 200,000 iterations and the minimized error function is shown in Fig. 7-5. Based on this figure, the mean absolute error at the starting point is ~78%, while as the reconstruction process continues the mean absolute error decreases to ~58% after 1000 generations and to ~6% after 100,000 iterations. However, from 100,000 to 200,000 iterations, the mean absolute error changes by only ~1.5%; thus, the reconstruction process can be stopped at any point in this range.

As it was mentioned in the reconstruction process, the ODF and the 2-point statistics of both empirical and simulated microstructures are quantitatively compared using an error function (Eq. (7-2)). The differences between the ODFs of both microstructures are represented in Fig. 7-6. The solid line in these plots indicates the ODF (volume fraction of grains having similar orientations within a 5-degree bin in the $FZ_{3C/4}$) of the experimental microstructure, and the markers deviating around the solid line represents the ODF fraction of the simulated microstructure with different grain-orientation assignments.

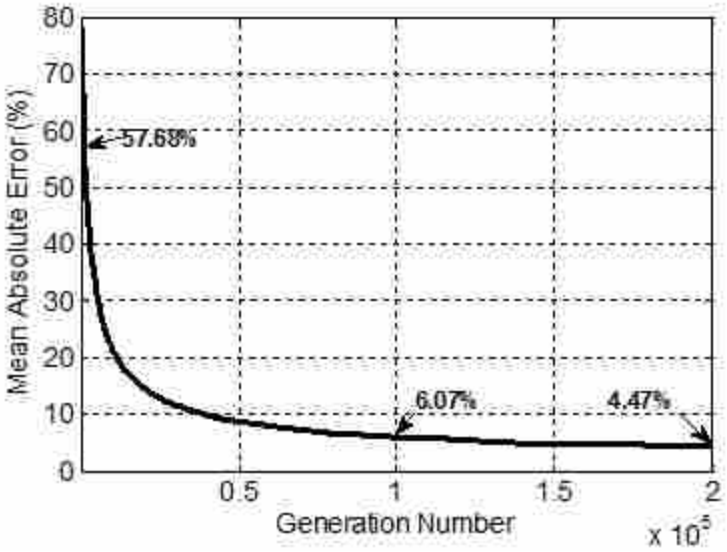

Fig. 7-5: An Error plot indicating the mean absolute error between the empirical and the reconstructed microstructures.

Subplot (a) in Fig. 7-6 illustrates the relatively large variations of the ODF (volume fraction) of the reconstructed microstructure. This subplot was depicted after 1000 generations of the GA scheme. Subplots (b) and (c) demonstrate similar ODF information but for different amounts of GA generations (100,000 and 200,000 generations, respectively). As expected, the deviation of the ODF of the reconstructed microstructure from the ODF of the empirical microstructure decreases as the GA minimization process continues (i.e. larger number of generations). The 2-point statistics measured for the top five highest ODFs are also showing similar trend meaning that by increasing the number of GA iterations, the 2-point statistics manipulated from both empirical and reconstructed microstructures become more analogous (Fig. 7-7).

The GA minimization process that was used in this research to find an optimum reconstructed microstructure took ~43 hours on a standard PC, and was terminated after 200,000 generations, leaving a final mean absolute error of ~4.5% between the 3D reconstructed and the

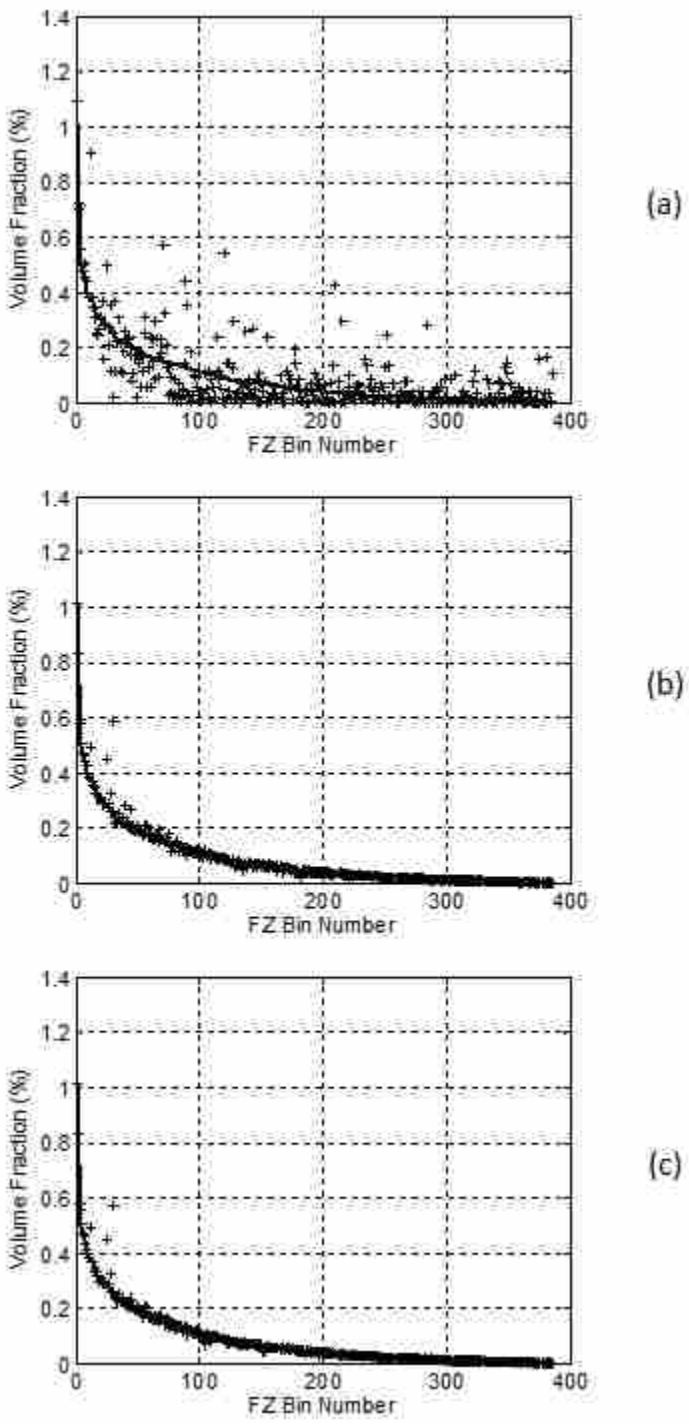

Fig. 7-6: The ODF (volume fraction) plots indicating the amounts of error using the GA method after: (a) 1000; (b) 100,000; and (c) 200,000 generations. The solid line indicates the ODF calculated from the empirical microstructure, while the markers indicate the variation of the ODF calculated from the reconstructed microstructure.

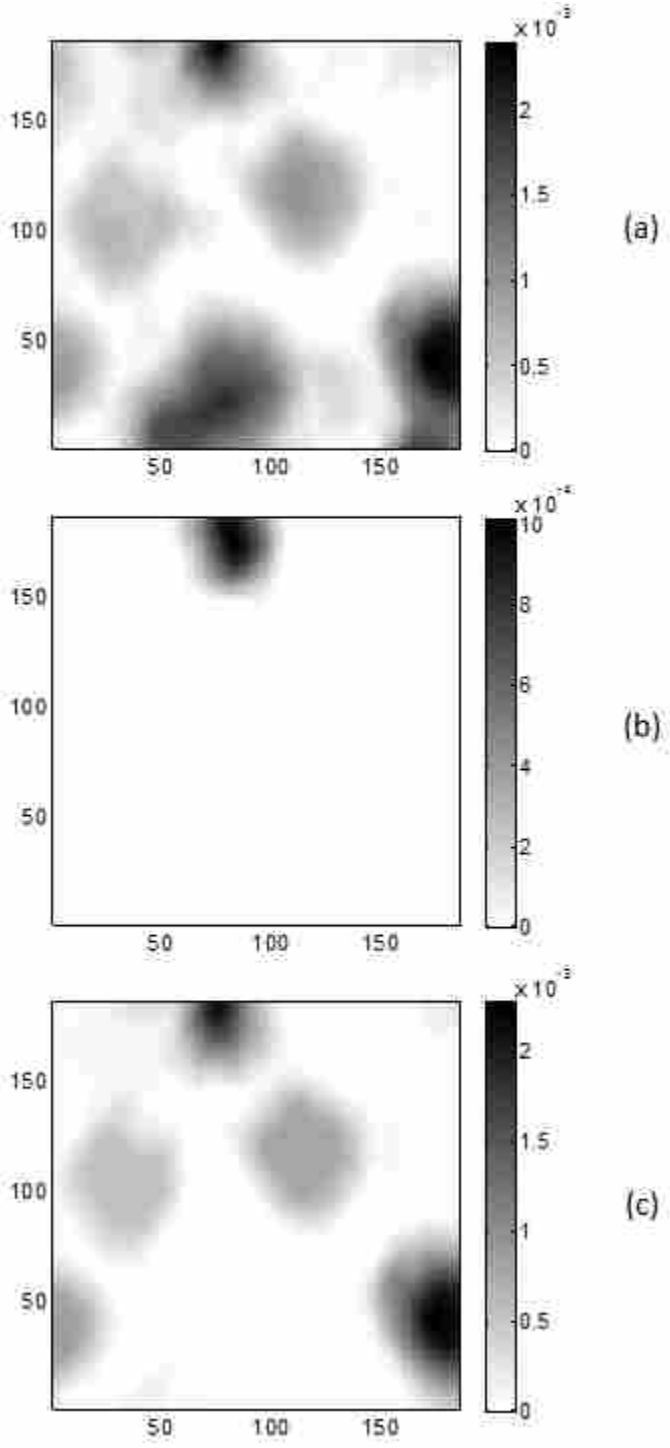

Fig. 7-7: A comparison of 2-point statistics of (a) the original microstructure, and the reconstructed microstructure (b) after 1000 and (c) 200,000 generations of GA

2D original microstructures. The 3D reconstructed microstructure can later be used in validation of the new Eulerian-based double continuity model. Schematic representations of the 3D reconstructed microstructure and an original 2D OIM section are shown in Fig. 7-8. To facilitate a comparison between the ODFs of the two microstructures, the same grayscale color map was selected.

7.2 Development and Application of the Double Continuity (DC) Model

In this section, a methodology to couple the mass- and orientation- continuity (MC and OC) models, which were formulated and validated in Chapters 5 and 6, is developed. This model is later applied to the 3D microstructure, and development of texture and statistical features in its microstructure is studied.

The MC and OC models were rearranged in previous chapters to take into account the evolution of the MF. According to the definition of the MF, Section 2.2.3, it can be seen that the MF can be expressed in many different spectral representations, among which the primitive basis was selected in this research. To express the MF based on the primitive representation, the spaces of interest in the mass and orientation space are tessellated, and bins in these spaces are enumerated. Then, indicator functions are used to specify which particular bin, here x^* in the mass and g^* in the orientation space, is being processed and how the MF changes for this bin. Previously, in the MC model, a TIP material was studied without taking into account the phase (or orientation) changes, and also in the OC model, orientations of a random texture was studied without taking into account the shape change of grains. In the double continuity (DC) model, however, changes in the shape of grains (in the mass space) and changes in the orientation of grains (in the orientation space) must be studied simultaneously. More clearly, the MC and OC equations are, respectively, rewritten here:

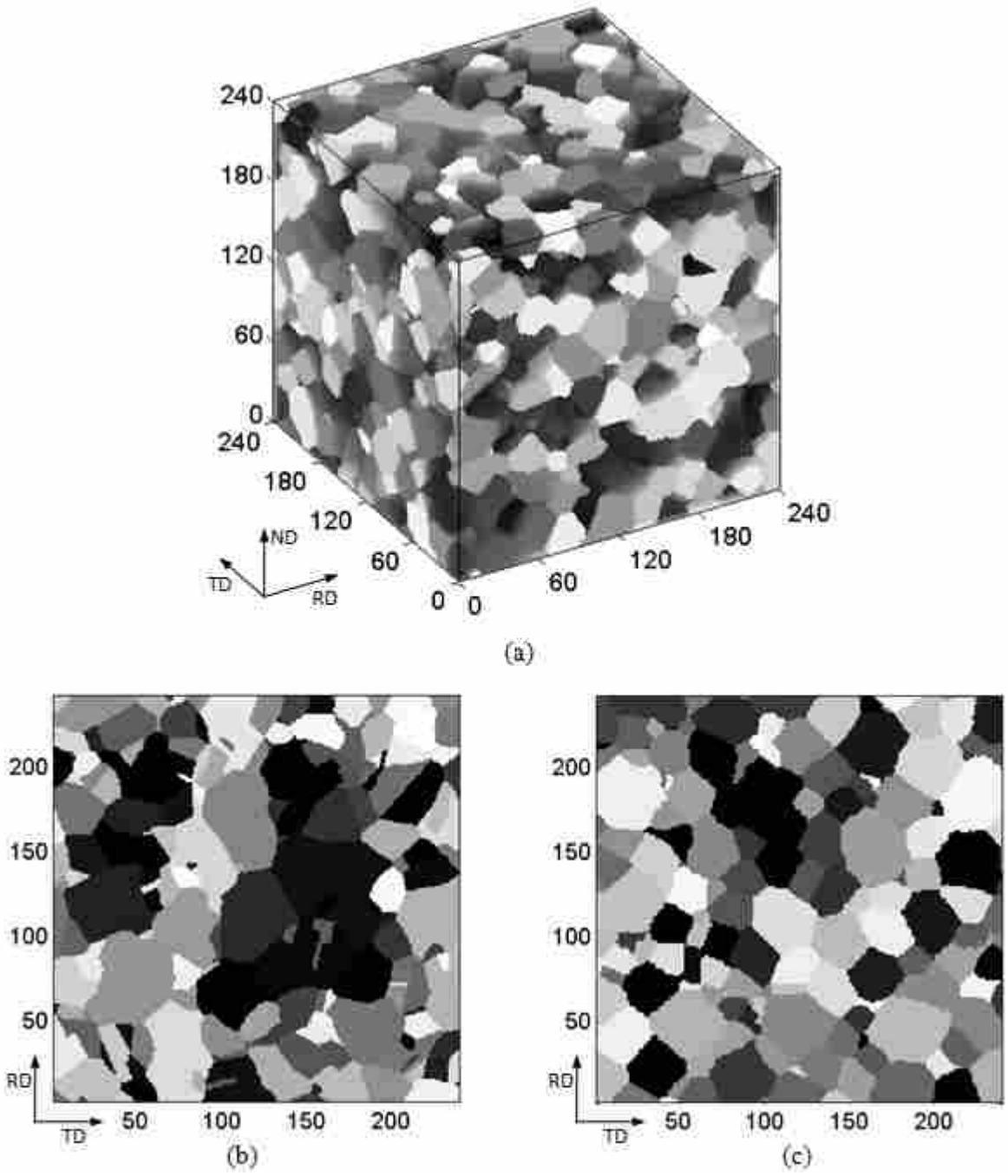

Fig. 7-8: Schematic representations of (a) the 3D reconstructed microstructure; (b) sample cut from the ND plane of the original microstructure; (c) an ND slice of the 3D reconstructed microstructure. All micrographs have similar color maps relative to the volume fractions of orientations in the tessellated $FZ_{3c/4}$.

$$\frac{\partial M(x,g^*)}{\partial t} = -v_i(x)\frac{\partial M(x,g^*)}{\partial x_i}$$

$$\frac{\partial M(x^*,g)}{\partial t} = -M(x^*,g)\frac{\partial w_i(x^*,g)}{\partial g_i} - w_i(x^*,g)\frac{\partial M(x^*,g)}{\partial g_i} - M(x^*,g)\cot\Phi w_2(x^*,g) \quad (7\text{-}3)$$

In the MC equation, orientation changes are neglected and the evolution of M is studied for a specific orientation g^*, while in the OC equation, evolution of orientations at a specific position x^* is studied. Now the question may be raised to how actually the evolution of a specific orientation g^* at a specific position x^* is studied, or in another word, how the evolution of $M(x^*, g^*)$ is to be examined. To answer this question, a very small time step is considered. At this period of time, as discussed in the MC model, some of the mass particles that have orientation g* come in/out of the bin located at position x* in the mass space; additionally, some of the grains that have orientations similar to g* may rotate and get in/out of the bin g* in the orientation space. As a result, to monitor these changes, these steps should be followed in the DC model: (i) a very small time step is selected; (ii) to have a better accuracy, the OC equation is firstly considered, orientations are updated in this time step and final orientation of all grains are obtained; (iii) grains that have orientations similar to g* and locate inside bin g^* are selected in the microstructure; (iv) evolution of these grains in the mass space is monitored and final configuration of grains is defined at the end of the time step; (v) the volume fraction of mass particles in bin x^* that have orientation g^* is finally reported as the updated $M(x^*, g^*)$. Afterwards, to obtain the overall microstructure evolution for all grains in the microstructure, same procedure (steps i-v) must be carried out for the rest of bins in both spaces.

The DC model can be employed to investigate the evolution of the 3D reconstructed microstructure. Selection of bin sizes for the mass and orientation spaces is very important. As discussed in Chapters 5 and 6, to avoid smearing problems and to minimize calculation errors,

the acceptable tessellation sizes for the mass and the orientation spaces were 0.075 microns and 0.5 degrees, respectively. By taking these tessellation sizes, there will be ~33 billion bins in the 3D mass space and ~5.8 million bins in the $FZ_{3C/4}$, although most of these bins are empty throughout the entire deformation process. Therefore, to avoid extensive and un-necessary calculations, an optimized DC model was considered. In this DC model, grains are deformed individually. In another words, instead of selecting grains with nearly the same orientation as a batch, we work on one grain at a time and separately monitor where it goes in the mass space and how its orientation changes in the orientation space. In this way, grains are studied in a small region in the mass space (depending on the volume of the grain) and it is not required to update the MF in the entire mass space.

The optimized DC model for the 3D microstructure has theses steps: (i) information about location and orientation of all grains are specified; (ii) for every grain, location of the grain in the mass space is found and depending on the velocity field, a box with an appropriate size is taken around the grain, as it has been shown in Fig. 7-9. Evolution of the MF for this grain in this box is monitored (similar in the MC model) and after some amount of strain (5%) the location of the grain is updated and a new appropriate box is selected around the grain. This process is continued until desired amount of strain is achieved; (iii) for every grain, position of its orientation in the $FZ_{3C/4}$ is obtained, and similar to Section 6.2, a cube with the size of 20×20×20 degrees is taken around the orientations. This evolution process is quite similar to that described in Section 6.2, where the OC model is employed and position of the orientation is updated after every 5% strain; (iv) the final configuration of all grains in the mass space is obtained. Because the MC model is developed for an incompressible material, no overlaps of grains should be detected. However, a small clean up effect occurs because of the smearing effect. To make a

comparison of simulated grains with their experimentally deformed ones, ND sections of the experimental an simulated microstructure are illustrated in Fig. 7-10; (v) final positions of grain orientations in $FZ_{3C/4}$ are also measured and stored to be used in obtaining the ODF and other textural and statistical analyses.

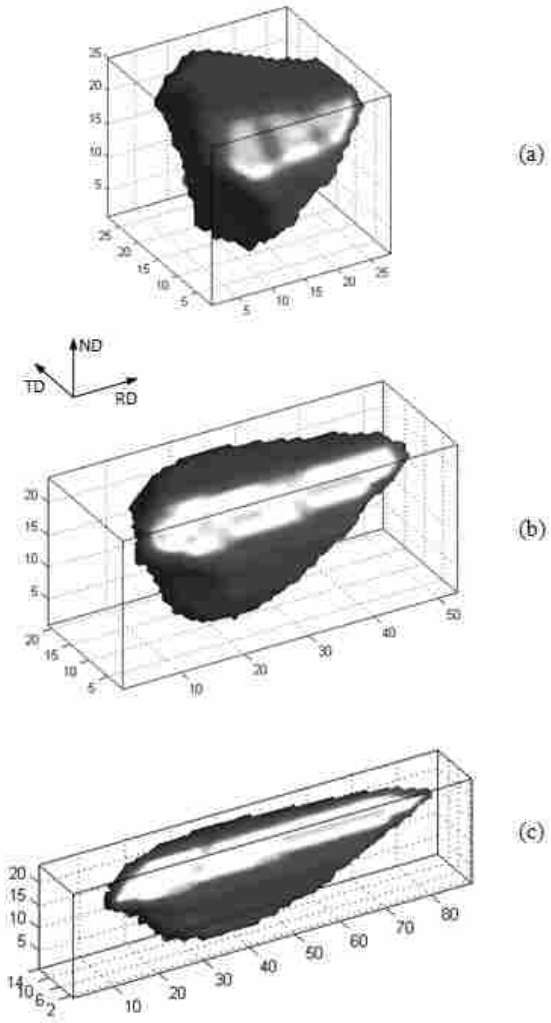

Fig. 7-9: A schematic of the evolution of an arbitrary grain in the microstructure under plane-strain compression (a) before applying any deformation, (b) compressed after 0.5 true strain, (c) compressed after true strain of 1.

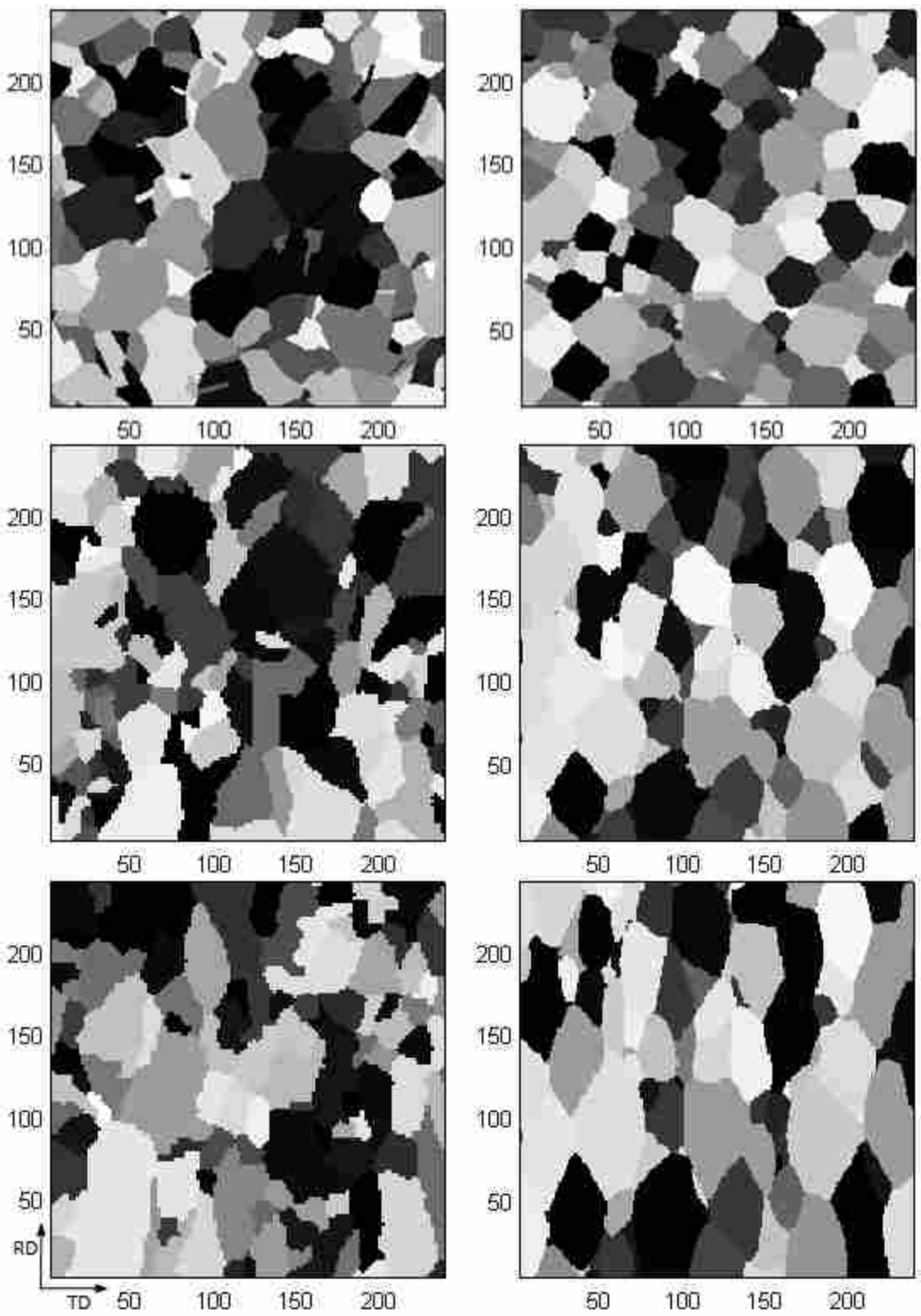

Fig. 7-10: Schematic micrographs of (left column) experimental ND-plane microstructures and (right column) the simulated microstructure predicted by the DCE model. Micrographs from top to bottom indicate rolling reductions of 0, 30, and 50%, respectively.

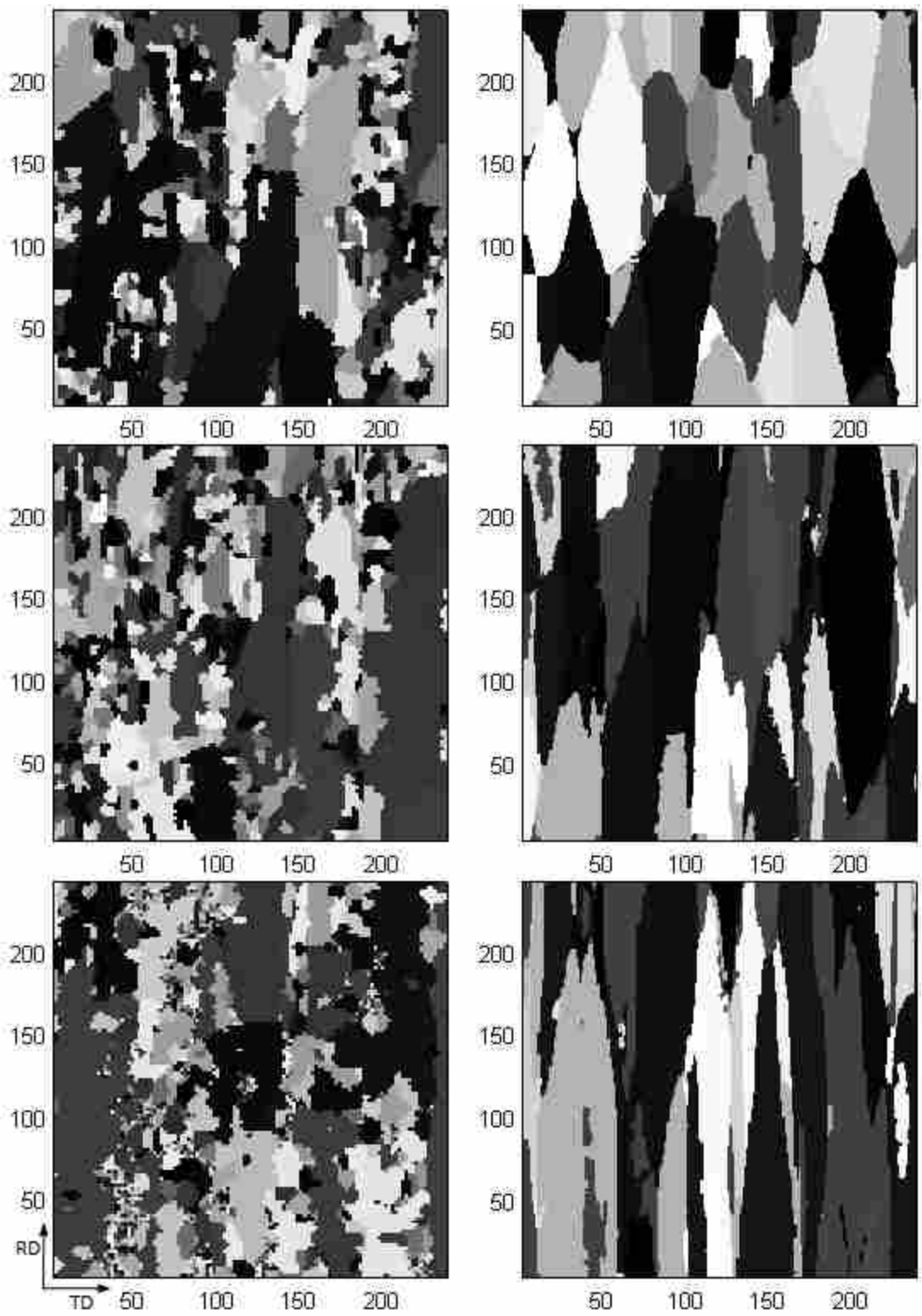

Fig. 7-11: Schematic micrographs of (left column) experimental ND-plane microstructures and (right column) the simulated microstructure predicted by the DCE model. Micrographs from top to bottom indicate rolling reductions of 70, 85, and 92%, respectively.

7.3 Texture Analysis Results

To analyze the experimental and numerical textures, three detailed methods of texture analysis were used in this research. Firstly, stability of ideal orientations developed in the rolling texture of FCC metals with medium/high SFEs is studied. Secondly, using pole figures a quantitative decomposition of the ODF into components with Gaussian scattering is developed. A Gaussian distribution with a half-scatter width of 5°, and orthorhombic sample symmetry is used, in connection with (200) and (111) planes are constructed.. All pole figures presented here are equal area projections of the specified crystallographic poles. And thirdly, to quantify the intensity of texture components, ODF sections and plots of α- and β- fibres are provided. OIM software (OIM-TSL 2007) was used to clean up the data, and plot the inverse pole figure (IPF) maps, ODF sections, and texture fibers; while, MTex software (HIELSCHER and SCHAEBEN 2008) was used to calculate and plot the pole figures.

7.3.1 Stability of Ideal Orientations

The stability of the ideal orientations of rolling textures for FCC metals (cube, Goss, brass, copper, Taylor and S) and their influence on texture formation are investigated in this section. The characteristics of the three-dimensional lattice rotation fields at and in the vicinity of these orientations, as well as the development of preferred orientations during deformation, are simulated numerically using the TLVP crystal plasticity model. The selected boundary condition is plane-strain compression (i.e. rolling process).

To explore the neighborhood of a particular ideal orientation, a mesh grid with the size of 2 degrees was selected in the range 20°×20°×20° around the orientation. The lattice rotation rates were then calculated (see Section 4.3), and the local orientation velocity fields around ideal orientations were demonstrated in Fig. 7-12. In this figure, the divergence of the lattice rotation

vector, $div\dot{g}$, is also shown as a grayscale map. According to this map, orientations are accumulated toward a point if the divergence is negative and they diverge if the divergence is positive.

From subplot (a) in Fig. 7-12, which represents the rotation fields around the Cube orientation, it can be seen that the field is symmetrical with respect to all three axes. During rolling, orientations rotate toward the Cube along the direction of the φ_1 axis, but move away along the Φ axis. This implies that orientations cannot reach the Φ axis (through cube) during rolling. The further an orientation is away from Cube, the faster it rotates. The change in φ_2 is rather small compared to the other directions. Similarly, rotation fields around Goss and Brass can also be examined. From the divergence maps in subplots (a-c), it is seen that the divergence of all three components (Cube, Goss, and Brass) is theoretically either zero or negative, and they are expected to be stable orientations. However, they are not stable in all three Euler directions. For example, Cube is not stable in the Φ axis, Goss diverges in the φ_1 and φ_2 axes, and Brass is roughly unstable along the φ_2 axis. Comparison of the Copper and Taylor orientations in subplot (d) also suggest that since the divergence around these two orientations is negative, they are also expected to mathematically be stable. The rotation field around these orientations, however, suggest that both orientations are almost unstable along the φ_1 and φ_2 directions (divergence rate is very small and negligible), and also, along the Φ axis for the Copper component. Therefore, these results (obtained by the TLVP model) suggest that Taylor is more stable that Copper and we must observe a larger fraction of grains to rotate to the Taylor end position. By way of contrast, it has been reported in the literature that Copper is the most stable component of rolling texture of FCC materials (HIRSCH and LUCKE 1988b; HUMPHREYS and HATHERLY 2004; LEFFERS and RAY 2009). Two types of S components are also studied, subplot (e). The S_3 is the

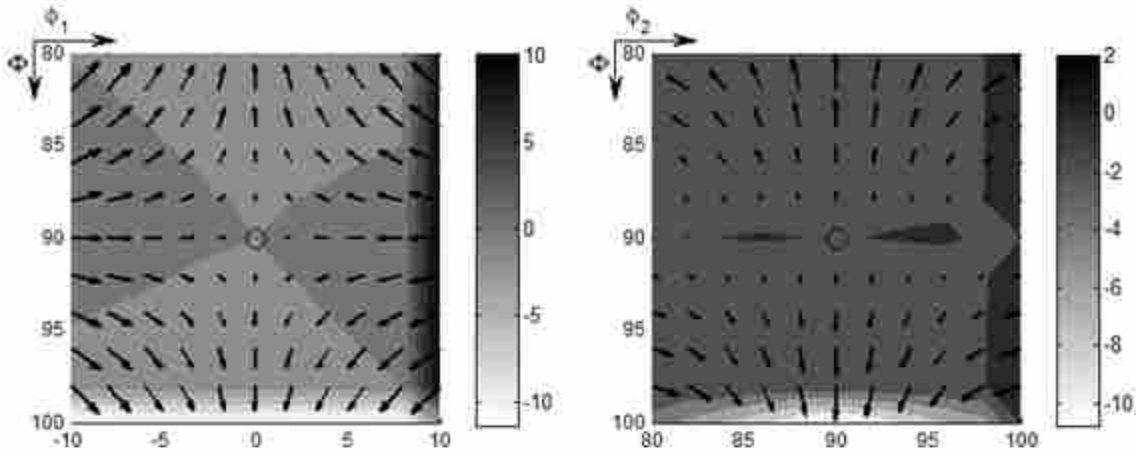
Φ1
Φ
80
85
90
95
100
-10
-5
0
5
10
10
5
0
-5
-10
Φ2
80
85
90
95
100
2
0
-2
-4
-6
-8
-10

(a)

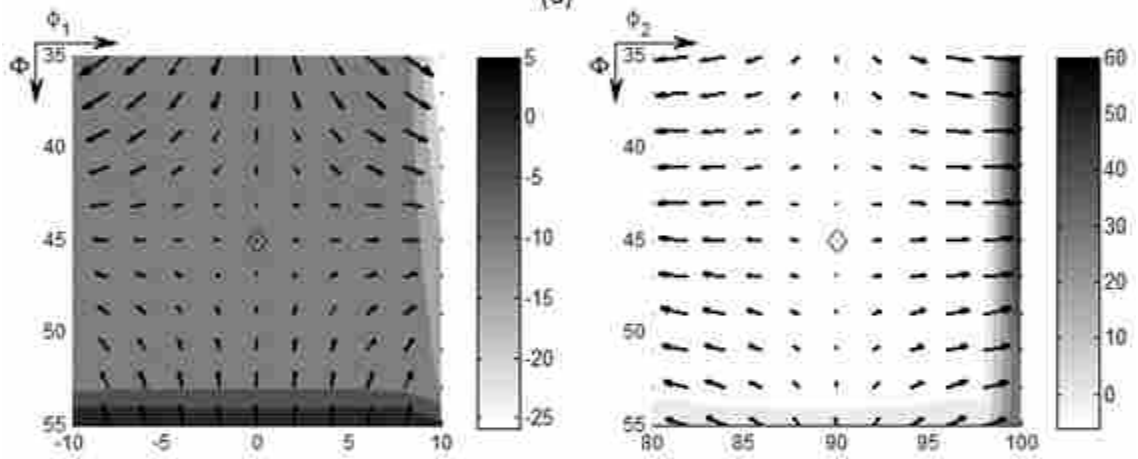
Φ1
Φ
35
40
45
50
55
-10
-5
0
5
10
5
0
-5
-10
-15
-20
-25
Φ2
35
40
45
50
55
80
85
90
95
100
60
50
40
30
20
10
0

(b)

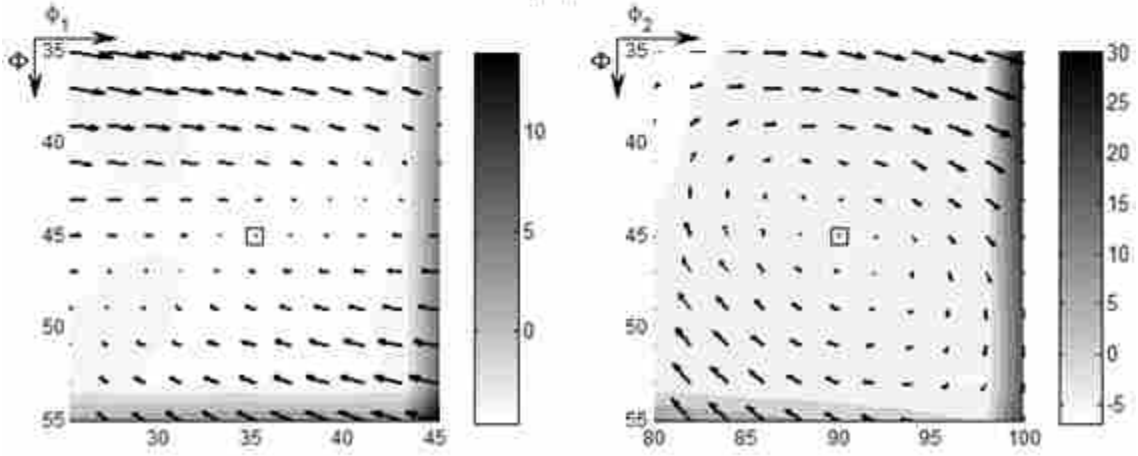
Φ1
Φ
35
40
45
50
55
30
35
40
45
10
5
0
Φ2
35
40
45
50
55
80
85
90
95
100
30
25
20
15
10
5
0
-5

(c)

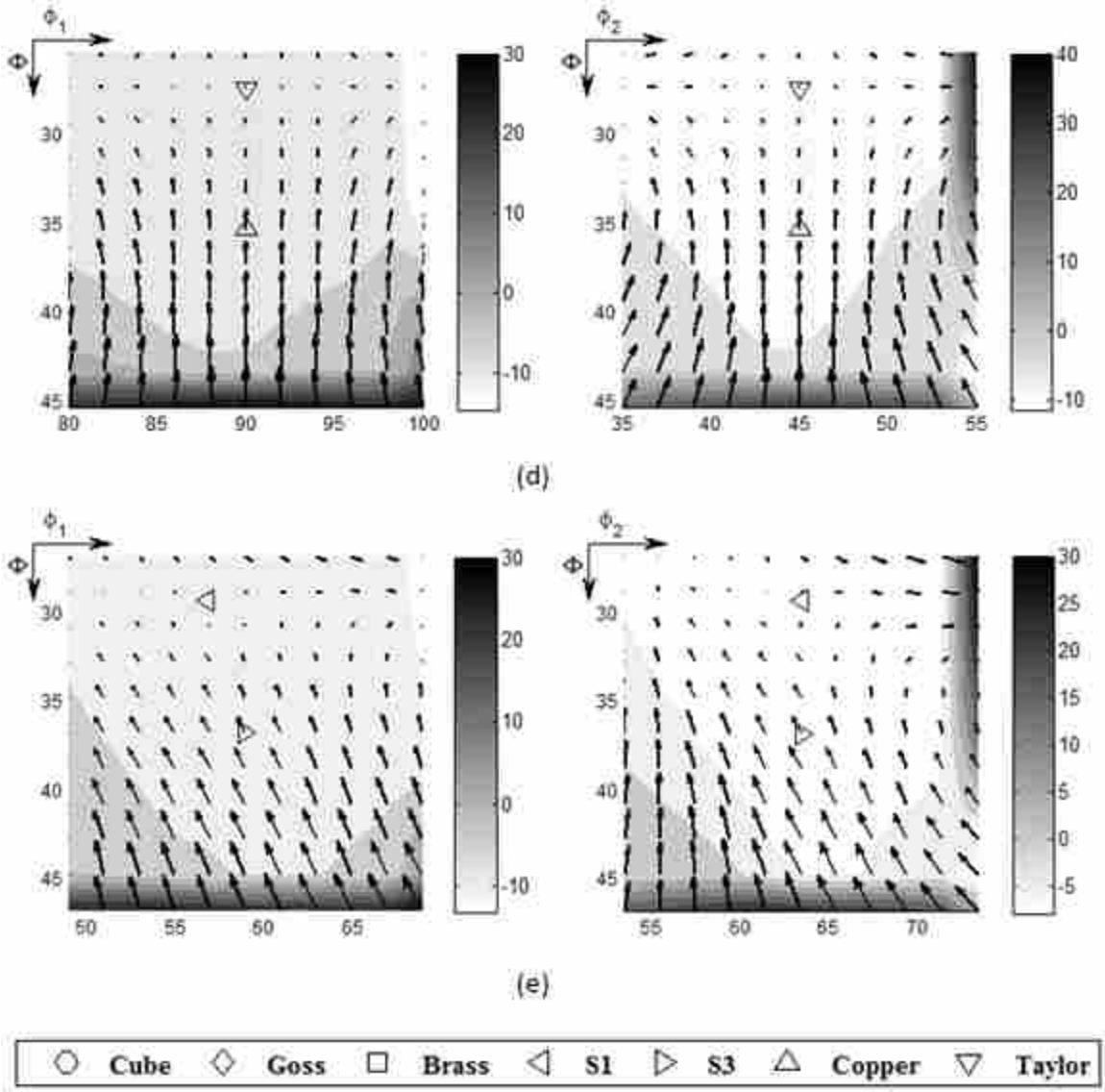

Fig. 7-12: Schematic representations of (a) the original microstructure (sample cut from the ND plane); (b) the 3D reconstructed microstructure.

component that is more distinguishable in the experimental texture maps; but, depending on the material and mechanical conditions, S_1 may become more stable (ZHOU *et al.* 1992). According to the TLVP model, the S_1 component is more stable (because orientations are converging toward S_1 in subplot (e)); however, since in the experimental texture plots, as we will see, the S_3

component has higher intensity, to be consistent with experiments, S_3 is considered for further analysis. To avoid confusion, S_3, from this point, is labeled and used as the S component.

After obtaining the orientation velocity field, the stability criteria (Section 4.4) were applied to examine the persistency of ideal orientations during the evolution process. Results are provided in Table 7-3.

Table 7-3: Rates of change ($\dot{g}$), gradients ($\partial\dot{g}/\partial g$), and stability parameters for some ideal orientations appearing in rolling textures.

	Cube	Goss	Copper	Brass	Taylor	S
$\dot{\varphi}_1$	0.00	0.00	0.00	0.00	0.00	-0.19
$\dot{\Phi}$	0.00	0.00	-0.47	0.00	0.00	-0.37
$\dot{\varphi}_2$	0.00	0.00	0.00	0.00	0.00	0.45
$\partial\dot{\varphi}_1/\partial\varphi_1$	-1.00	1.00	1.00	-1.01	1.00	0.57
$\partial\dot{\Phi}/\partial\Phi$	1.00	-1.00	-3.30	-0.67	-3.47	-2.70
$\partial\dot{\varphi}_2/\partial\varphi_2$	0.00	-6.00	-3.65	-2.43	-4.46	-3.71
$sum(\partial\dot{\varphi}_i/\partial\varphi_i)$	0.00	-6.00	-5.97	-4.11	-6.93	-5.84
$\dot{\Phi}\cot\Phi$	0.00	0.00	-0.67	0.00	0.00	-0.50
$div\dot{g}$	0.00	-6.00	-6.64	-4.11	-6.93	-6.34
Stability (Eq. 4-6)	1.00	1.00	0.37	1.00	1.00	0.43

The results show that the values of $\dot{g} = (\dot{\varphi}_1, \dot{\Phi}, \dot{\varphi}_2)$ are zero at the Cube, Goss, Brass, and Taylor orientations. Based on the stability criterion expressed in Eq. (4-3), an orientation is stable when generally $\dot{g} = 0$ and $\partial\dot{g}/\partial g$. According to this criterion, Brass is the only orientation that is fully stable and other orientations are partially stable. If negativity of $div\dot{g}$ is selected as the stability criterion, it is found that all the ideal orientations (except Cube) will become stable

end-orientations. Based on this criterion, Taylor has the most negative value $div\dot{g}$ and therefore it is the most stable orientation of simulated rolling textures predicted by the TLVP model. Additionally, results from the stability equation (Eq. (4-6)) reveal that all studied orientations are fully stable except S and Copper. The stability value, however, is not low, and based on this equation, it is expected to see an increase in the amount of S and Copper in the simulated rolled microstructure.

7.3.2 Pole Figures

For FCC metals it is common to calculate and plot (200) and (111) poles. As the level of deformation strain is increased, volume fraction of orientations (and the ODF) is changed. One way to monitor these changes is tracking the evolution of pole figures. Pole figures of experimental and simulated microstructures are illustrated in Fig. 7-13. It is seen that as the amount of cold roll is increased, a specific texture starts to form. This form of texture is the copper texture that is the dominant texture of medium and high SFE metals. Comparisons of experimental and simulated pole figures reveal that: (i) the undeformed pole figures are similar - which confirms that the GA model has predicted a good final reconstructed microstructure; (ii) as the amount of deformation is increased, the difference between the maximum intensity of experimental and numerical pole figures are increased. For example, for the 92% reduction, maximum intensity for experimental and simulated (111) pole figures are 7.2 and 14 times random. Thus, it is concluded that the DC model overestimates texture strength – which is a common weakness of Taylor-like models. This can perhaps be addressed with greater precision by the stability examination of ideal orientations. Fig. 7-14 shows the (200) and (111) pole figures of experimental and simulated microstructures, overlapped to find the location of the

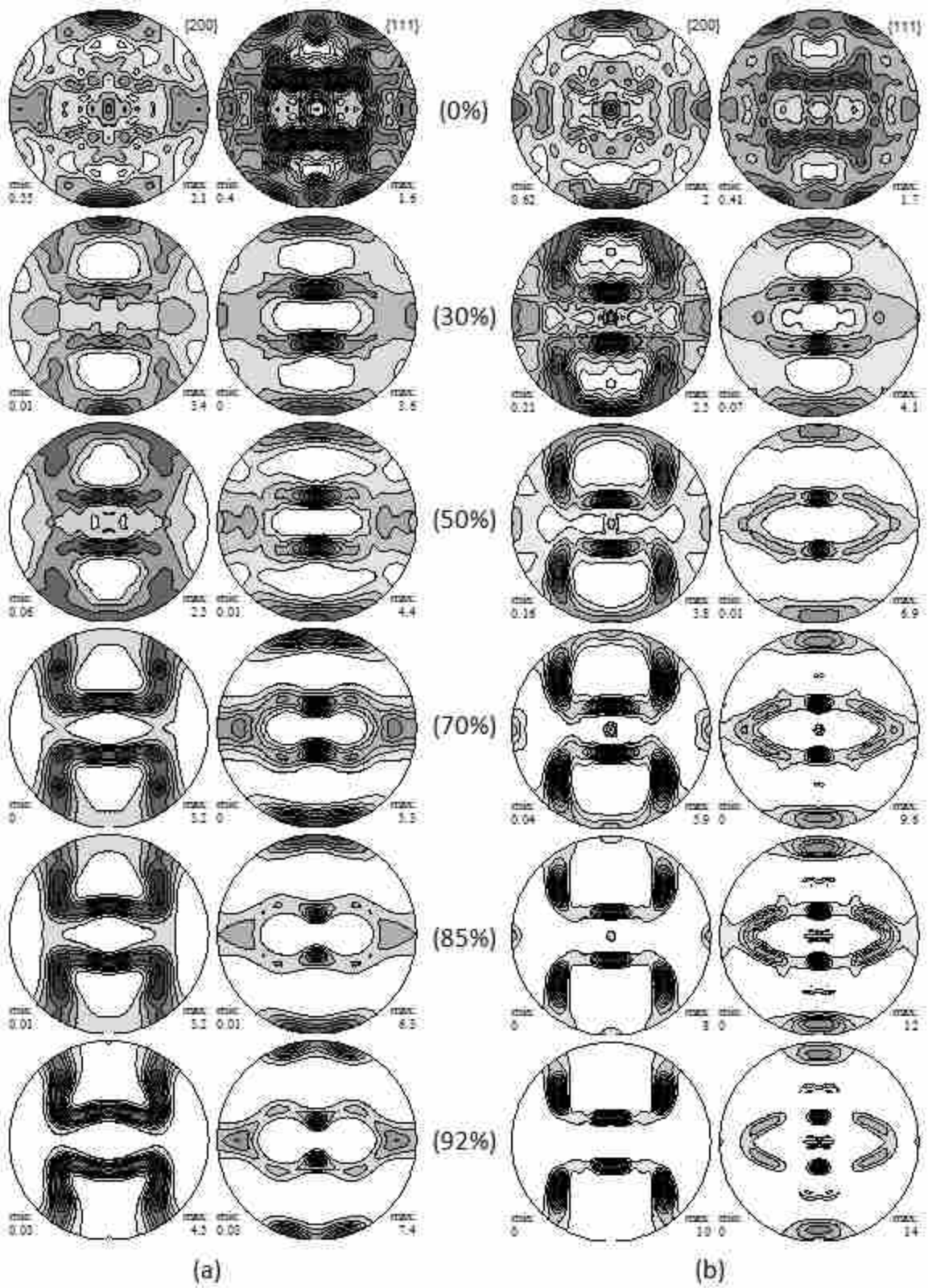

Fig. 7-13: {200} and {111} pole figures (a) measured from experimentally rolled samples; and (b) predicted by the Eulerian model. Pole plots have been sorted for different amounts of cold work –top to bottom: 0, 30, 50, 70, 85, and 90% cold reductions.

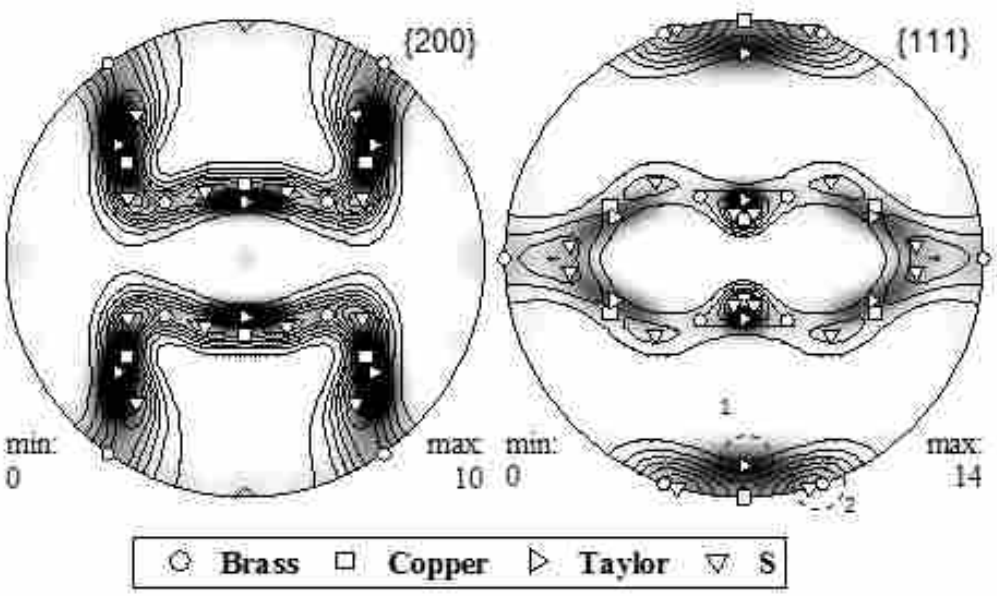

Fig. 7-14: {100} and {111} pole figures measured from experimental and simulated data for the 92% cold rolled material. Skeletons indicate the experimental texture, while the grayscale contour shows the simulated texture.

highest intensities. The skeleton lines demonstrate the experimental texture, and grayscale contours indicate the simulated texture.

From Fig. 7-14, it is seen that the intensity of Taylor component (circle 1 in the figure) is exaggerated in the simulated pole figure. Also, it can be seen that the intensity of Copper and S components may be underestimated. However, this may not be clear in the pole figure and it can be studied precisely by the ODF section plots.

7.3.3 ODF Analysis

As discussed in Section 4.2, α- and β-fibres are two dominant texture fibres found in the microstructure of FCC rolled materials. Fig. 7-15 demonstrates the α- and β-fibre plots for the experimental and simulated microstructures. Goss and Brass components are the two ideal

orientations that are placed in the α-fibre. Comparisons of orientation densities along the α-fibre show (i) that the density of Goss does not change during the deformation and the TLVP model can provide a reasonable prediction for this orientation, (ii) that by increasing the level of deformation, the density of Brass is generally increased and the accuracy of the TLVP model is decreased. Along the β-fibre, densities of Copper and S are studied. Results from comparing β-fibres show that the TLVP model cannot give a good prediction for both Copper and S components. For example, the density of Copper in the experimental microstructure is about 30 times random, but this value in the simulated microstructure is 60 times random. Also, the density of S in the experimental and the simulated microstructures are about 46 and 74 times random, respectively. The density of Cube and Taylor, however, cannot be obtained from the fibre analysis. To examine the development of these two orientations, the ODF was sliced at certain places (where $\varphi_2 = 0, 45, 65^o$) and ODF section plots were illustrated in Fig. 7-16.

From the comparison of ODF section plots in Fig. 7-16, it is observed that as the deformation process continues, the density of Brass, Copper, Taylor and S in both experimental and simulated microstructures is increased. The development of the Taylor component is more obvious in the simulated microstructure because the level of the intensity peak in the $\varphi_2 = 45^o$ section is shifted up as it compared with the similar section in the experimental microstructure. The location of Taylor $(90^o, 27^o, 45^o)$ is shown in the key plot provided at the top of Fig. 7-16. Another comparison show that the maximum density observed in the experimental and simulated microstructures is 10 and 38 times random, respectively. This implies that the TLVP model employed to examine the texture of polycrystalline nickel overestimates the density of some (not all) of the orientations. The rate of this overestimation is 3.8.

Concluding from comparisons of pole figures, fibre-plots, and ODF section plots, it was generally found that the TLVP model overestimates the density of Brass, Copper, Taylor and S

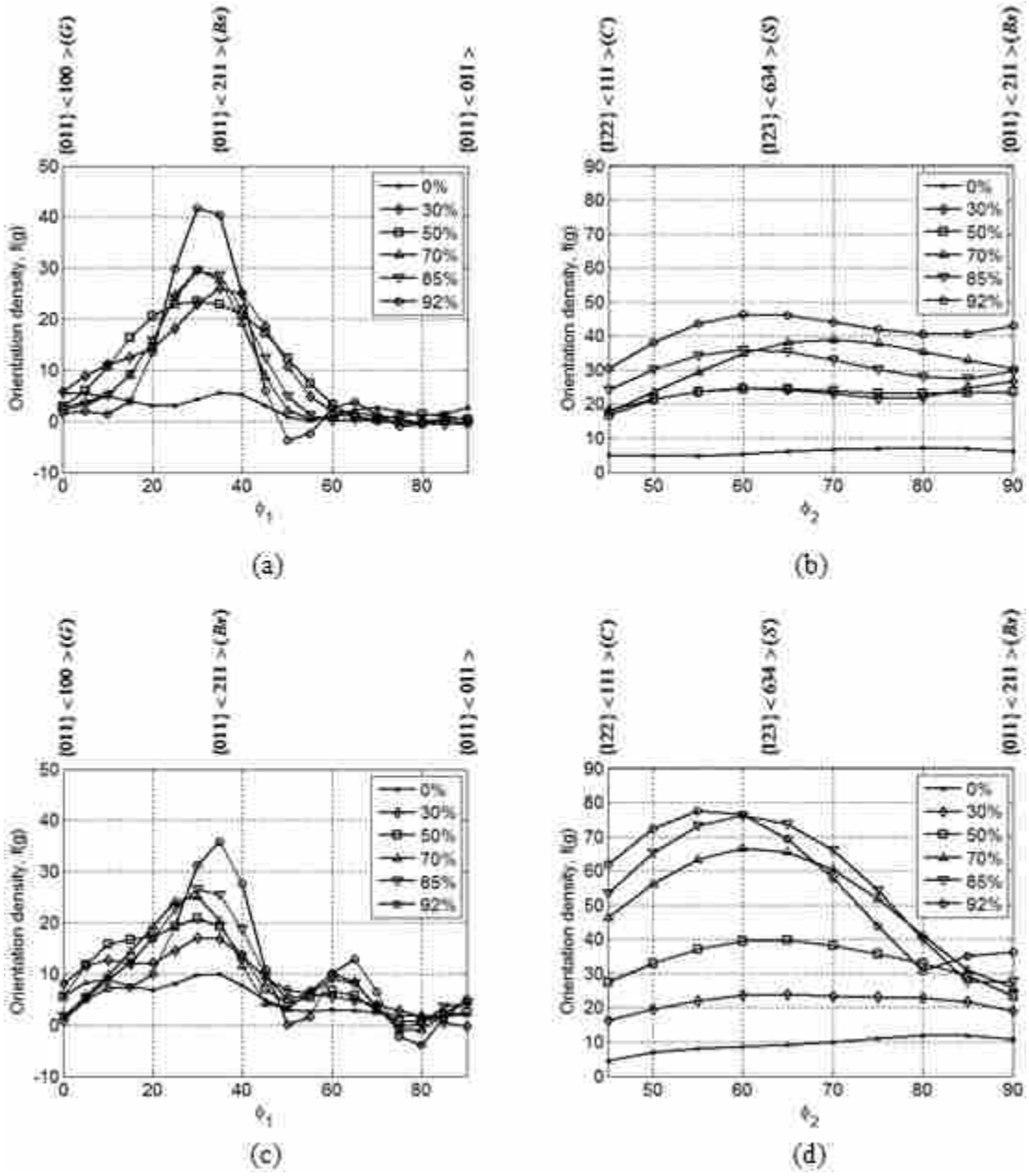

Fig. 7-15: Orientation density of orientations along (a) α-fibre and (b) β-fibre for the experimental microstructure; (c) α-fibre and (d) β-fibre for the simulated microstructure. Some of the ideal orientations are labeled on the fibre plots.

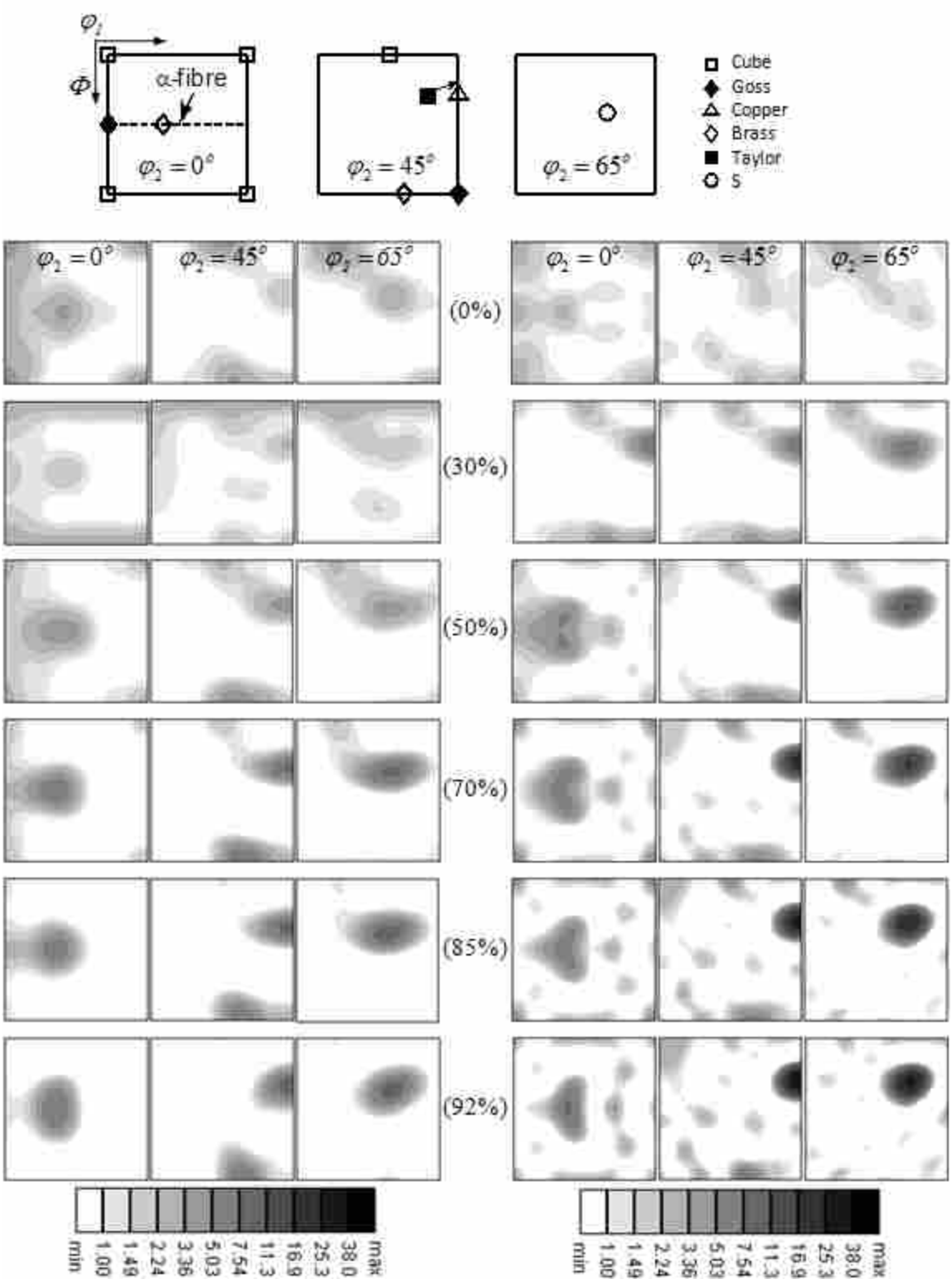

Fig. 7-16: ODF section plots demonstrate the development of texture components in the experimental (left column) and the simulated (right column) microstructures

orientations. Stability analysis of these orientations suggests that in the TLVP model the moststable end-orientation is the Taylor orientation. The divergence of Brass, Copper, and S are also largely negative, which causes a faster convergence of orientations around these locations, and consequently, the larger increase in the density of these orientations.

7.4 Statistical Analysis Results

Much recent work has shown that many deformed metals develop rather similar types of microstructures, and that these change in a similar way with increasing strain. If the relationships between some of these microstructural features were to obey simple laws, it would be easier to model microstructural development, and because of this, there has been significant interest in examining *similitude* and *scaling* of deformation microstructure. Some of the examples of scaling and similitude that can be identified in the microstructure of metals of the same type are addressed here. An inverse relationship between cell size and amount of applied strain is an example of scaling that is valid for most metals. Another example of scaling is the inverse relationship between the cell size and the square root of dislocation density inside the cells, which is often found during high temperature deformations of FCC metals.

The scaling and similitude that are used in the literature to compare properties of similar metals are basically linear relationships, used to approximate an unknown microstructure of a material by knowing the scaling factor and amount of similarity existing between the microstructures of the same materials. To examine the properties of a microstructure more comprehensively, in addition to texture analysis tools (utilized in the previous section), the 2-point correlation function is employed. Using the 2-point correlation function enables us to find the correlation relationships between the orientation and location of grains in the studied microstructure, and to find the statistical features that existed or developed by deformation in the

material. In this section, firstly, to confirm the data obtained from the texture analysis, volume fractions of ideal orientations are studied; and secondly, the 2-point correlation functions are employed to obtain the autocorrelation length and the maximum pair-correlation length of some ideal orientations, and also to recover the length of coherency in the experimental and the simulated microstructures.

7.4.1 Volume Fraction of Ideal Orientations

Volume fractions (VFs) of some ideal orientations are measured from experimental and simulated ODFs. To find the volume fraction of a particular ideal orientation, location of the orientation in the $FZ_{3C/4}$ is specified, neighboring orientations within 10 degrees of the ideal orientation are selected, and all grains having these orientations are chosen in the microstructure; then the volume fraction of these grains is determined. As it is obvious, for every orientation in the FZ_{3C}, there are three symmetrically-equivalent orientations (variants). Therefore, in finding the volume fraction of ideal orientations, variants of ideal orientations must be included – Table 7-4. Note that for Copper and Taylor components there are only two identical variants in the $FZ_{3C/4}$ as the third one is located at the position of either of the two invariants. Volume fractions of ideal orientations measured from experimental and simulated microstructures are illustrated as bar-graphs in Fig. 7-17.

One specific observation from VF-plots is that the amounts of Cube and Goss components are negligibly small as compared to other texture components, and their amount stays constant as the rolling deformation continues. This implies that Cube and Goss components are stable orientations and all orientations around them (within a range of 10 degrees) do not converge/diverge much from these points. VF of the Brass component, however, increases by

Table 7-4: Ideal orientations of rolled FCC texture and their symmetrically-equivalent variants in the $FZ_{3C/4}$

	Variant I			Variant II			Variant III		
	φ_1	Φ	φ_2	φ_1	Φ	φ_2	φ_1	Φ	φ_2
Cube	0	0	0	0	90	0	0	90	90
Goss (G)	0	45	90	0	45	0	90	90	45
Copper (C)	90	35	45	39	66	27			
Brass (Bs)	35	45	90	35	45	0	55	90	45
Taylor	90	27	45	41	71	20			
S	59	37	63	27	58	18	52	74	34

increasing the amount of cold rolling, but with a very low convergence rate. On the other hand, orientations around Copper, Taylor and S components converge faster, in both experimental and simulated microstructures, and VFs of these orientations are increased consistently for higher amounts of cold work. The rate of convergence of orientations in the simulated microstructure is much higher as compared to the experimental microstructure. This can be explained by grain interaction phenomena that occur in plastic deformation, as discussed in Section 4.5. In fact, when grains want to rotate, in reality, interaction forces from neighboring grains do not allow the studied grain to move freely. These interactions are ignored in the TLVP model, with the consequence that the orientation evolution simulated by this model is overestimated.

Absolute errors between VFs of experimental and simulated microstructures are also shown in Fig. 7-17 (c). It is seen that the largest contradiction between experimental and simulated texture results happens for the Taylor components. This is one of the obstacles of all Taylor-type models. In fact, the reason that, in the literature, this texture component is termed

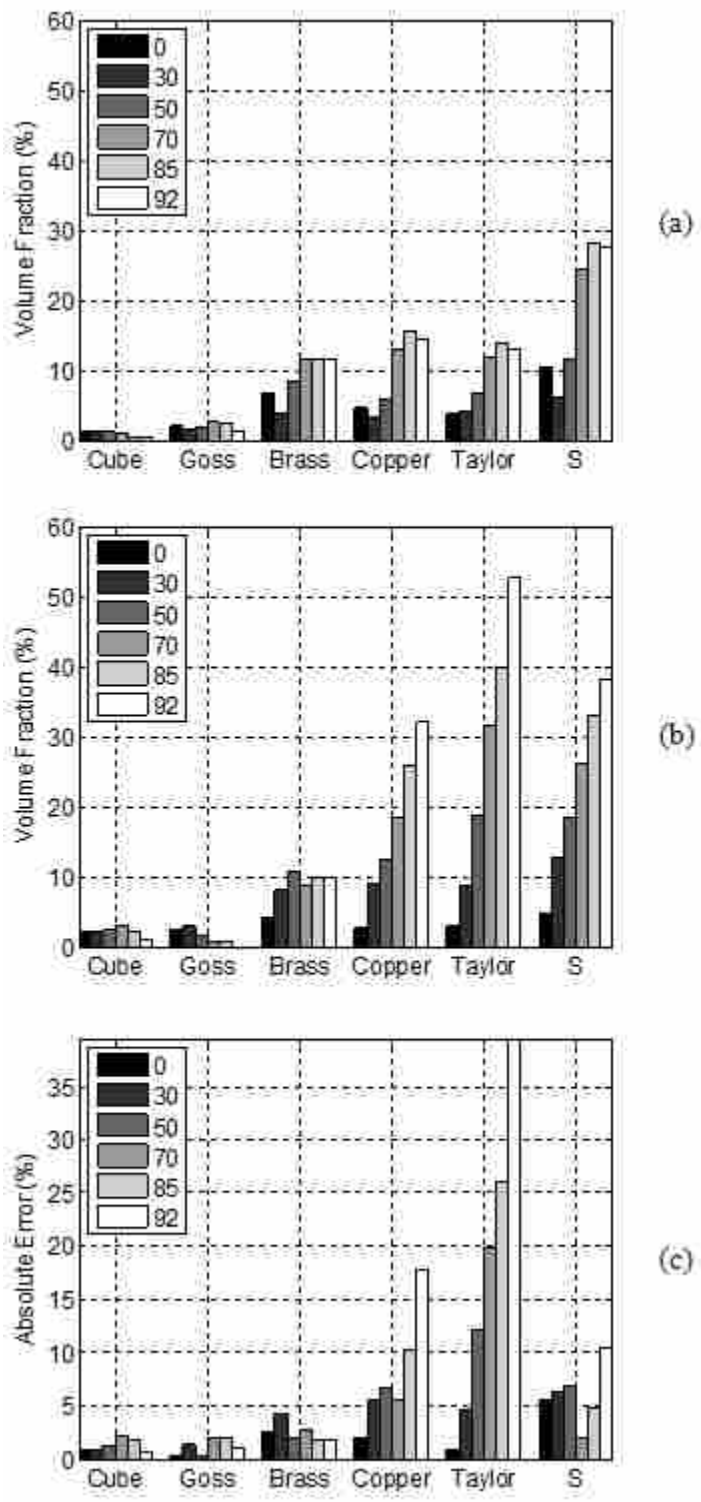

Fig. 7-17: Volume fractions of ideal orientations vs. different amounts of rolling reductions for (a) experimental microstructure, (b) simulated microstructure, and (c) absolute error between volume fractions measured from (a) and (b).

Taylor is that Taylor-type models overestimate the VF of this orientation. Copper and S components are also overestimated by the TLVP model. The results from pole figures, fibre plots, and ODF sections from previous sections also verified that the TLVP model that has been used in simulation of orientation changes in the DC model cannot give acceptable predictions of texture evolution of Copper and Taylor components. Thus, Cube, Goss, Brass and S components, that exhibit smaller simulation errors, are taken for further analysis with the 2-point statistics in the next section.

7.4.2 Two-Point Statistics

In this section, statistical functions are incorporated to examine the accuracy of the DC model. The 2-point correlation functions or pair correlation functions (PCFs) are used to obtain some of the statistical features of the microstructure –such as (i) autocorrelation and anti-correlation of ideal orientations, (ii) grain shape changes, and (iii) the coherence length.

7.4.2.1 Autocorrelation Relations

Pair correlation functions can be used to find the correlation relationships between two material points at distance r from each other. If autocorrelation is considered, these two points can be from the same grain or from two separate grains but having the same orientation. Correlations and anti-correlations may also happen for two separate grains with different orientations. For example, if grains that have Cube orientations and grains that have Goss orientations are selected in the microstructure, and PCFs are used to find the correlation relations of these grains, it can be seen that, for a specific length and direction of r, three types of relationship can be found (i) grains of Cube and Goss may like each other and a positive correlation may be found for these grains, (ii) they may have no tendency to appear together at

distance *r*; for this case, no correlation is observed between these two sets of grains (iii) they may like to repel each other at this distance and show an anti-correlation relation.

To study the autocorrelation relations, PCFs are used to examine the occurrence of grains with a similar crystallographic orientation. In another words, $f_2(g,g|r)$, which is identical to the 1-point correlation function or the ODF when *r* tends to zero, is used to study the autocorrelation relations. Fig. 7-18 shows a standard PCF plot that has been obtained by selecting grains with the S component (and its neighboring orientations within 5 degrees away). FFTs were used to manipulate PCFs. A similar method, explained in Section 5.2, was used to obtain and illustrate the PCF plot. Additionally, the PCF plot was centered so that the origin of the *r*-space $\Psi(r)$, is located in the middle of the plot.

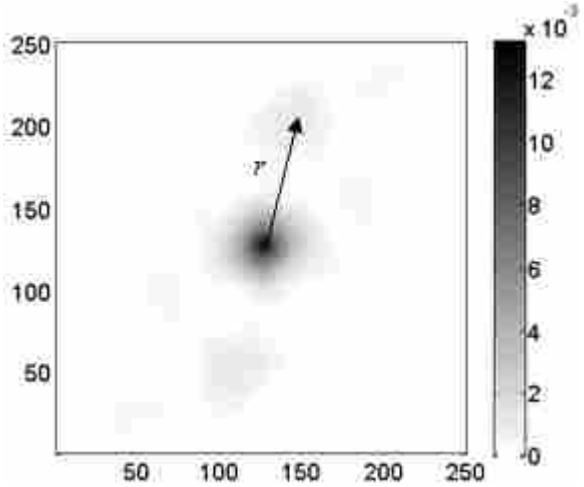

Fig. 7-18: A standard PCF plot representing the autocorrelation of grains having S orientation

As it was expected, the center of the plot has the highest intensity. This is because the probability of auto-correlating and landing small vectors *r* in the same grain is high; but, as the length of *r* is increased the chance to find points with similar S orientation is decreased. The

maximum intensity occurs when *r* approaches zero and shows the VF of S orientation in the microstructure.

The intensity in the PCF plot, Fig. 7-18, is very low, and sometimes (especially when studying the correlation of two different pairs of orientations is important) it is useful to renormalize the PCF. A method of renormalization is suggested by Gao (GAO *et al.* 2006). In this method, the original PCF is normalized by VFs of the paired material points as:

$$\tilde{f}_2(g,g'|r) = \frac{f_2(g,g'|r) - f(g)f(g')}{f(g)f(g')} \tag{7-4}$$

The advantage of this renormalization is that it emphasizes the magnitude of $f_2(g,g'|r)$ relative to $f(g)f(g')$, which is the un-correlated probability for the occurrence of orientation g and g' at large distances in microstructures. When $f(g)$ and $f(g')$ are both small, $f_2(g,g'|r)$ may be negligibly small; on the contrary, if $f(g)f(g')$ is large, $f_2(g,g'|r)$ will also tend to be large at certain *r*. Thus, the influence of the orientation distribution on the PCF can be eliminated by performing this renormalization. Fig. 7-19 shows the renormalized PCF plot.

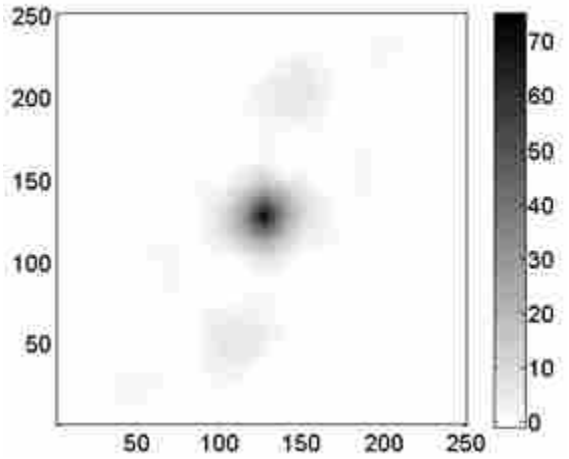

Fig. 7-19: A normalized PCF plot demonstrating autocorrelation of grains with S orientation

By comparing the original and the renormalized plots, it is seen that the maximum amount of autocorrelation in the normalized plot, 75, is roughly equivalent to the inverse of the maximum autocorrelation in the original plot, 0.0132. To explain this, based on the renormalization equation, when r is very small (for the case of maximum autocorrelation) $f_2(g,g|r)$ converges to $f(g)$, and the renormalized PCF is calculated as $\tilde{f}_2(g,g|r) = 1/f(g) - 1$. Similarly, as *r* increases, the chance of autocorrelation is decreased, $f_2(g,g|r)$ approaches zero, and the renormalized PCF consequently approaches -1, which is the lowest possible value of the normalized PCF.

Autocorrelation can be used to find the grain size distribution and the shape of grains in the microstructure. An example is shown in Fig. 7-20. Grains with S orientations in the ND section of experimental and simulated microstructures (with 50% rolling reduction) are selected for this study. Fig. 7-20 (a) shows the geometry of grains in both experimental and simulated microstructures. Appropriate PCF plots that show the autocorrelation of S orientations (including orientations within a 5 degree range) are demonstrated in subplot (b). Another renormalization is required to scale the range of *r* based on the average grain size of the undeformed sample. The range of correlation in subplots (b) is, therefore, shown as *r/d*, where *d* is the average grain size of 18.86 microns. It is expected that grains in a sample with 50% rolling reductions elongate along the RD and remain unchanged along the TD; thus, the length-to-width ratio for an ideal 50%-rolled material should be about 2. Autocorrelation curves were measured along the RD and TD directions, Fig. 7-20 (a). Additionally, the autocorrelation length, r_{ac}, was measured along each direction, where the normalized PCF becomes zero. The autocorrelation lengths for the experimental and simulated microstructures along the RD are 3.21 and 4.17, and along the TD are 1.81 and 2.05, respectively. Therefore, the length-to-width ratio measured from the two

microstructures is 1.77 and 2.03, respectively. This implies that the shape of grains in the simulated microstructure differs a little from the experiments, which can be explained by the grain subdivision phenomenon observed in experiments.

The autocorrelation length along preferred directions (i.e. RD or TD) may be important, but sometimes an averaged autocorrelation length might be of more interest. To obtain the distribution of PCFs in all directions in the r-space, a radial distribution function (RDF) was used. In this way, the r-space (in the 2D plane) is tessellated into equally-spaced discs with the same thickness. Therefore, to measure the radial autocorrelation length, a thickness of 5 microns was selected. Afterwards, all points inside every bin (disk) were selected, and the average value of autocorrelation (for every bin) was calculated. Because the area of the disc is increased as r increases, the averaged value of autocorrelation is finally normalized by dividing its value by the area of the disk. The resulting normalized RDF measured for the microstructure in Fig. 7-20, is shown in Fig. 7-21. The radial autocorrelation length is measured as 2.58 and 3.68 respectively for the experimental and simulated microstructures.

The radial autocorrelation length for the S orientation (including orientations within a 5 degree range) in all samples with different amounts of cold rolling was measured similarly. For every level of deformation, three sections of the material (RD, TD, and ND sections) were examined, and the average value of the radial autocorrelation length was obtained and plotted in Fig. 7-22. In addition, the average value of autocorrelation length along the RD and TD was also obtained.

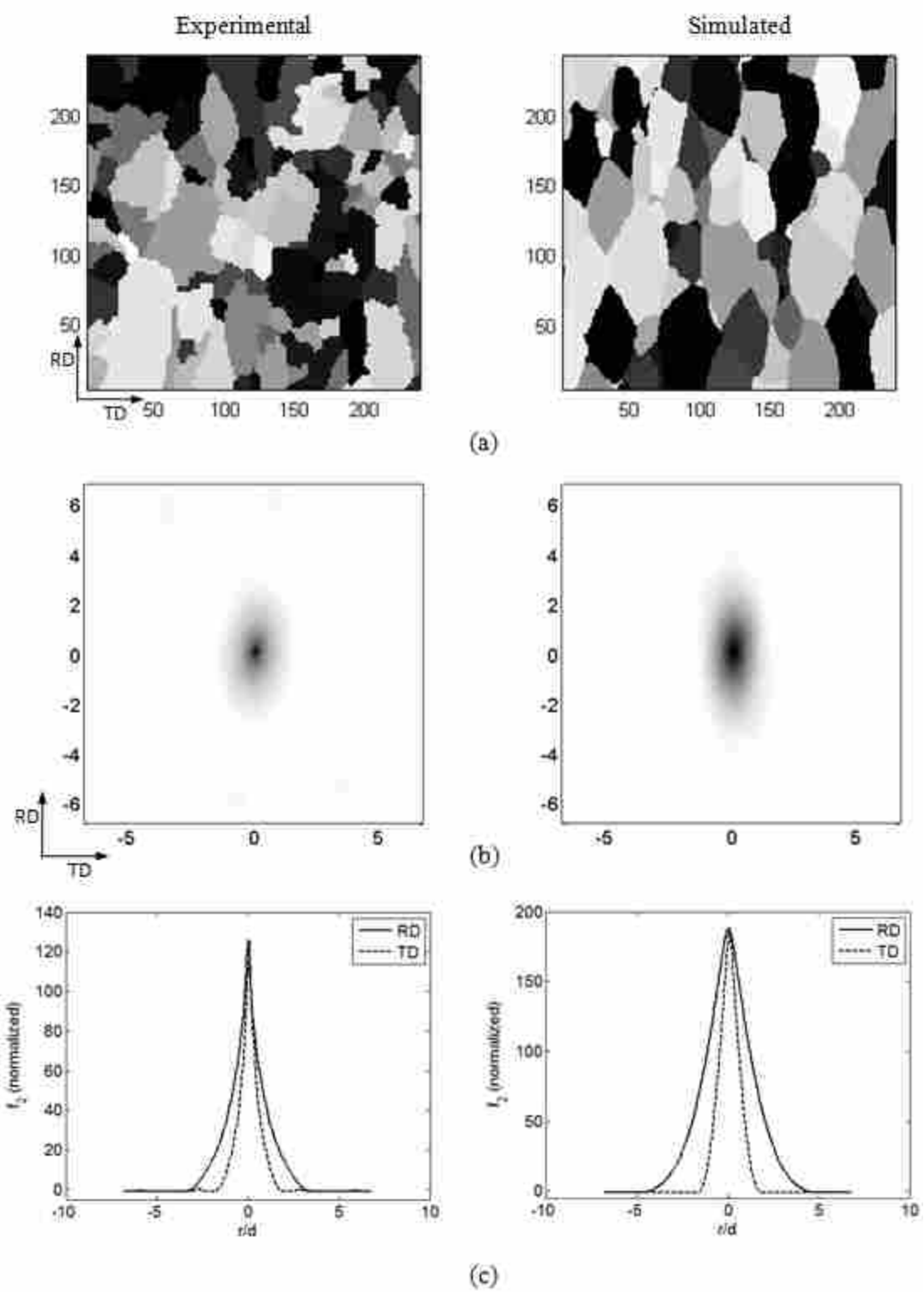

Fig. 7-20: (a) a 2-D schematic of the experimental and the simulated microstructures; (b) relevant autocorrelation plots for the S orientation in the 50% rolled ND sample; (c) related RD, TD, and radial autocorrelation curves

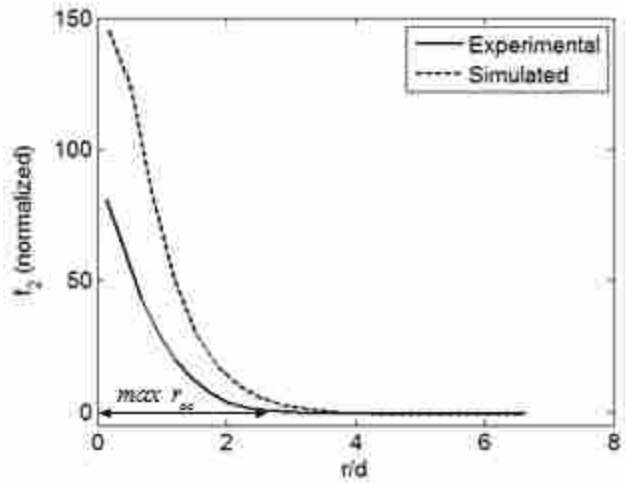

Fig. 7-21: The radial autocorrelation curves for the experimental and simulated microstructures. The autocorrelation of the S orientation was obtained in the 50% rolled ND sample.

Results depicted in Fig. 7-22 show that the RD autocorrelation length is increased by applying more deformation in both microstructures, while it stays nearly constant along the TD. The length of autocorrelation along the RD of the simulated microstructure, however, is increased with a larger rate as it is compared with the experimental one. This is explained by the fact that grains in the simulated microstructure are elongated along the RD by the rolling deformation. The autocorrelation length along the ND was not obtained because it can be predicted by the volume constancy principle. The comparison of the radial autocorrelations also show that the average size of elongated grains is consistently increased in the simulated microstructure, whereas in the experimental microstructure the size changes are not observed, presumably because of grain fragmentation. However, it is worth noting that the autocorrelation length is directly related to the maximum size of grains, but it does not give the exact value of the maximum grain size. For example, suppose that there are two grains with similar orientation that are placed in a very small distance. Then, if the autocorrelation of this microstructure is studied, because the distance between the two grains is small, the autocorrelation of these two grains

assumes that these two grains are, in fact, one big grain and the reported autocorrelation length will be the largest distance of the outer boundaries of these two grains.

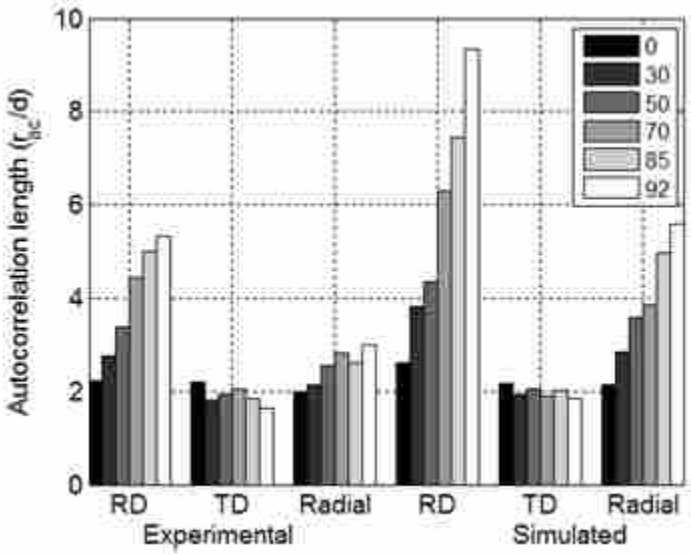

Fig. 7-22: The maximum autocorrelation length for the S orientation along RD, TD, and radial distribution for the experimental and simulated microstructures

RD, TD, and radial autocorrelation lengths for Cube and Brass were similarly measured and demonstrated in Fig. 7-23. Subplot (a) shows the autocorrelation lengths for the Cube orientation. It is seen that the RD autocorrelation length does not change with deformation in the experimental microstructure. Again, this can be perhaps answered by considering the grain fragmentation phenomenon. Another observation is that although the influence of the VF on PCFs was resolved by using the normalized PCFs, the VF shows an important influence on the autocorrelation length. For example the VF of S is relatively larger than those for the Cube and Brass orientations. Basically, when the VF is increased by increasing the level of deformation,

the chance of finding two grains with similar orientation at close distance is increased, and consequently the length of autocorrelation may be increased.

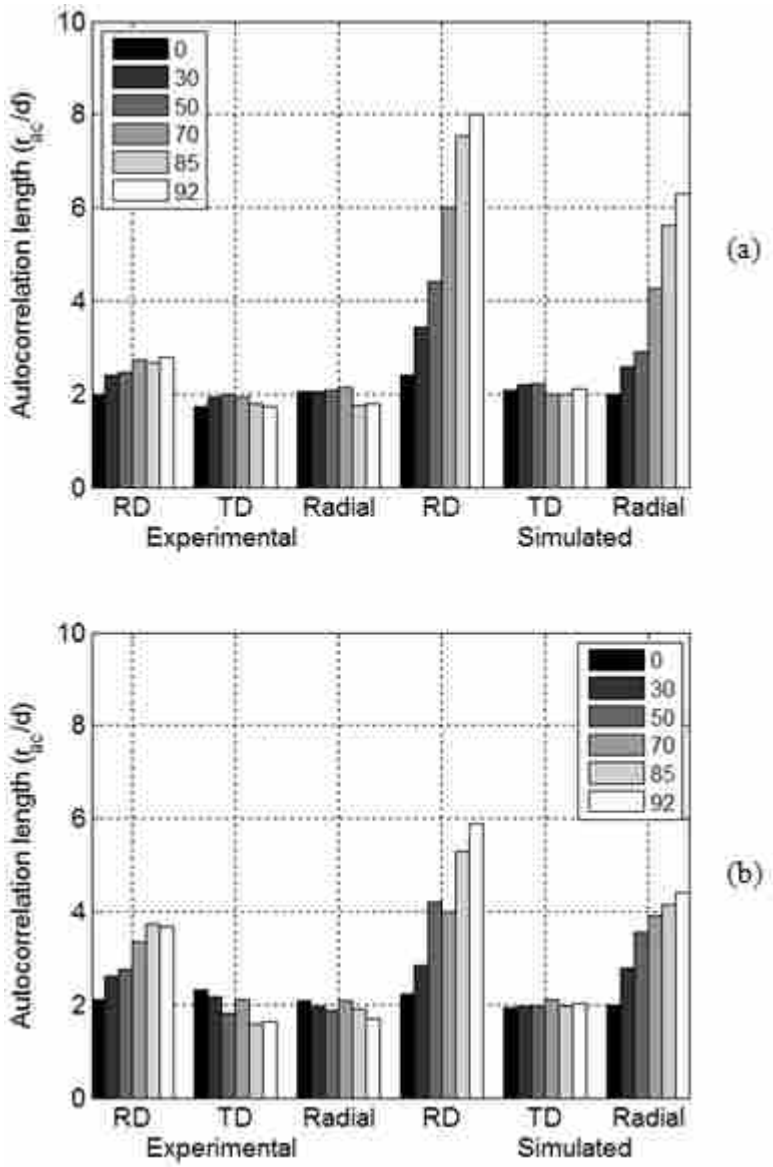

Fig. 7-23: The maximum autocorrelation length for (a) Cube and (b) Brass orientations along RD, TD, and radial distribution for simulated and experimental microstructures

General conclusions from comparisons of autocorrelation lengths of Cube, Brass, and S are that (i) grains with Cube orientation like to auto-correlate at shorter distances which implies that the Cube grains are generally smaller in size; (ii) the auto-correlation length of Cube in the experimental microstructure does not vary in different directions which means that Cube grains are equi-axed, and their shape does not change with deformation; (iii) RD autocorrelation length of the simulated microstructure is always larger than the one in the experimental microstructure. This implies that grains in the simulated microstructure can freely deform, but in experiments they are not allowed to; (iv) grains with the S orientation are expected to be more elongated in shape as their RD autocorrelation length is larger than those for Cube and Brass.

7.4.2.2 Pair-Correlation Relations

The correlation relations of grains with two different sets of orientations were also studied. Different pairs of ideal orientations with different ranges of neighboring orientations can be studied. If a range of 5 degrees from ideal orientations is selected, it was found that lesser correlation of pairs is obtained. Thus, a 10 degree range around studied orientations was selected. FFTs were used and the normalized PCFs obtained for pair-correlation analysis. To show how the pair correlation plots were obtained, a pair of Cube and S orientations was selected in the 50% reduced ND section of both experimental and simulated microstructures. Results are shown in Fig. 7-24. The pair correlation plots for both microstructures are presented in subplot (a). Some correlations are seen at particular locations. To examine the correlations along specific directions, the RD and TD pair-correlation curves are demonstrated in subplot (b). It is seen that the pair-correlation plot is not symmetrical, and there may be some correlations in one direction but not in the opposite side of that direction. Therefore, in this study, it was decided to only consider radial pair-correlation functions that show the distance at which a specific correlation is

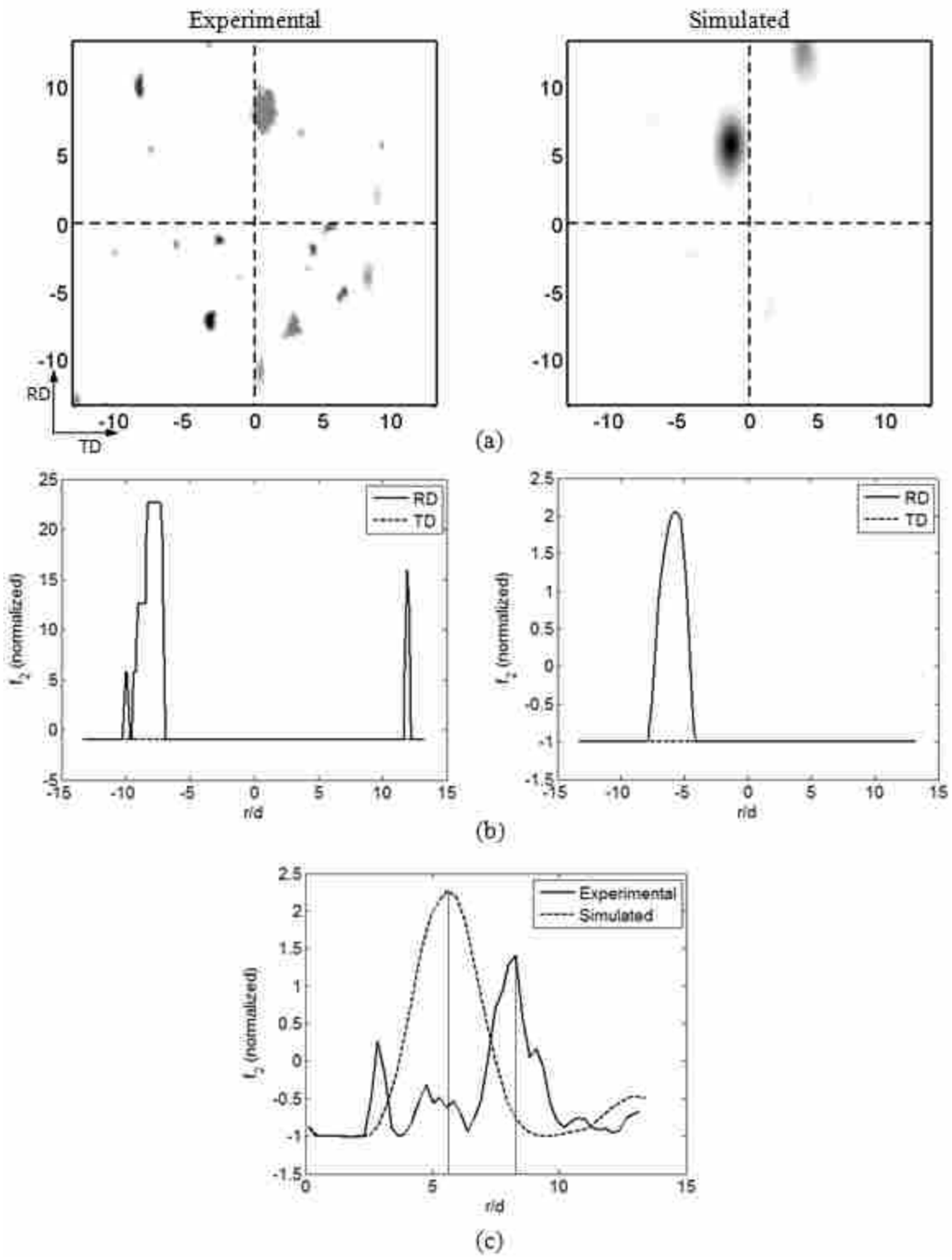

Fig. 7-24: An example of pair-correlation plots for the Cube-S pair in the 50% rolled ND section (a) pair correlation plots; (b) RD and TD pair-correlation curves; (c) radial pair-correlation curve

observed in the microstructure. Subplot (c) shows the radial pair-correlation curve calculated for both microstructures.

Similar to the autocorrelation length introduced in the previous section, a correlation length can be determined. This is the distance in which the maximum correlation of studied pair is observed. The maximum correlation length for the experimental and simulated microstructures is 8.29 and 5.61, respectively. In addition to the maximum correlation length, the amount of correlation is also important. For example, in subplot (c), correlation of the selected pair in both microstructures is positive which implies that the two sets of orientations "attract" each other and the chance of exploring these two orientations at the maximum correlation distance is high. On the other hand, if the correlation density is negative, anti-correlation is occurred and the two sets of orientations want to "repel" each other.

The radial pair-correlation plots for a Cube-S pair in three sections (ND, TD, and RD) and different levels of deformation are demonstrated in Figs. 7-25, 7-26, and 7-27. In these figures, because there is not enough material in the ND direction of the most heavily deformed simulated microstructure (as it is seen in the TD and RD section plots), only a short range correlation relation of up to 10 times *d* was studied. Short range correlations are seen in the TD and RD plots. Also, as the level of deformation is increased, the amount of correlation is decreased and, generally, negative values of correlation are found for heavily deformed microstructures. It is also seen that for the 50% rolled ND section, the experimental microstructure shows a correlation after 10 *d*, but correlations larger than half of the thickness of the 3D microstructure are not accurate and should not be considered in the analysis.

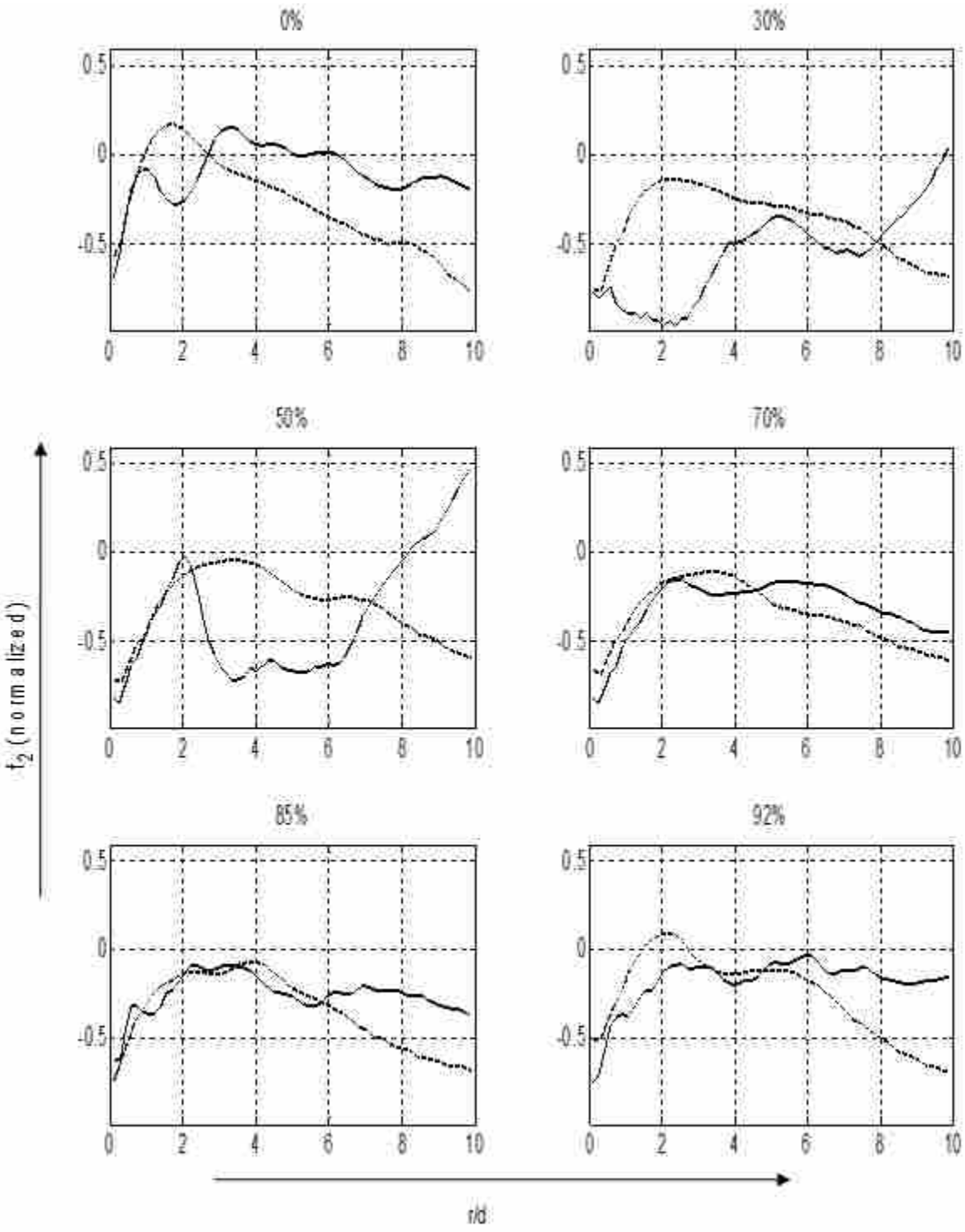

Fig. 7-25: Pair-correlation plots for the Cube-S pair along the ND section

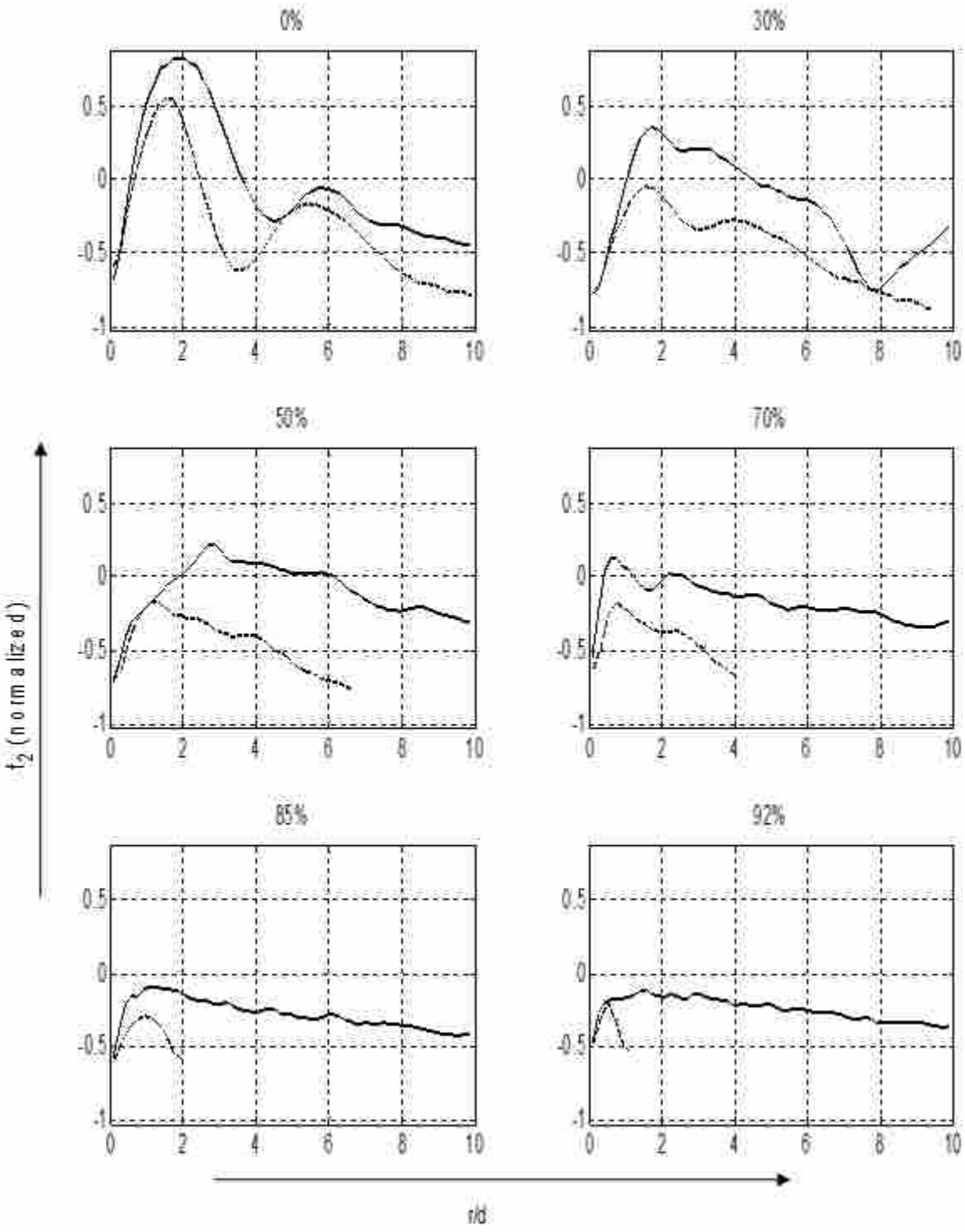

Fig. 7-26: Pair correlation plots for the Cube-S pair along the TD section

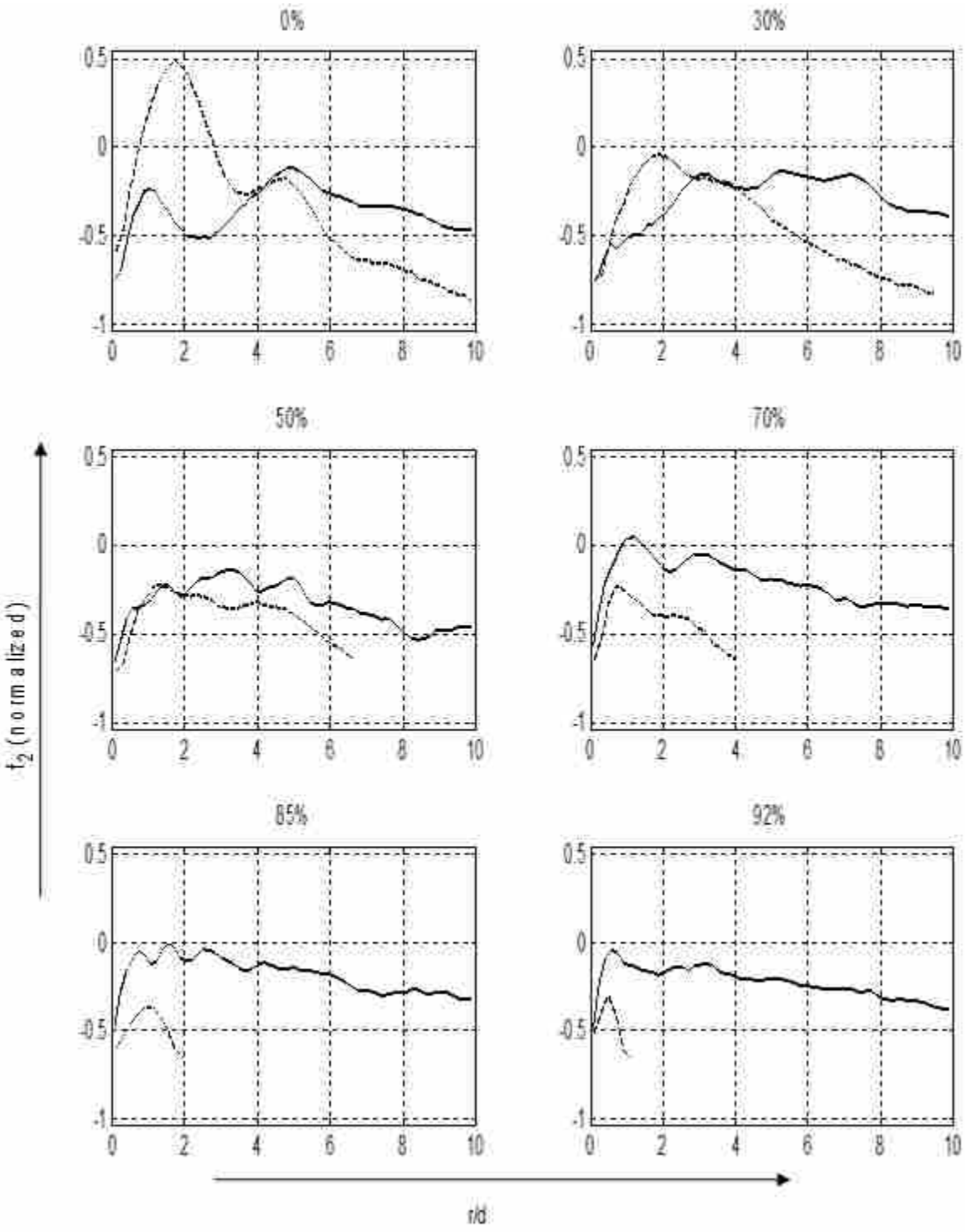

Fig. 7-27: Pair correlation plots for the Cube-S pair along the RD section

The maximum correlation distance for the Cube-S pair was measured in RD, TD, and ND sections, and the average value of the radial pair-correlation distance was obtained for different levels of deformation, Fig. 7-28.

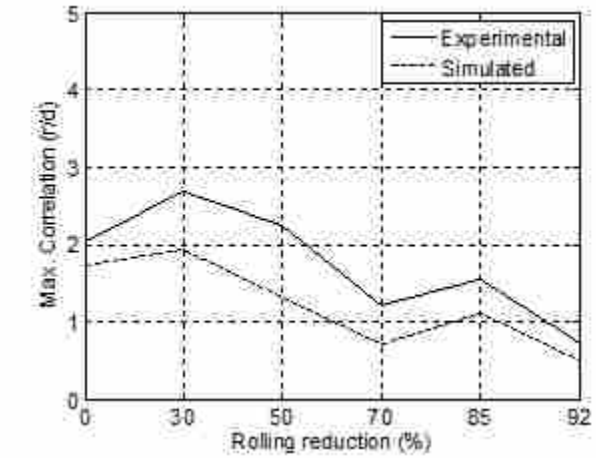

Fig. 7-28: The averaged maximum correlation distance for the Cube-S pair

According to Fig. 7-28, as the level of deformation is increased, the correlation length of grains with Cube and S orientations is decreased. This can be explained by the effects of the VF. Usually, by increasing the VF of S during deformation, as discussed before, the chance of finding S in the microstructure is increased, and therefore, the pair of Cube-S may correlate at shorter distances. It is also seen that the simulated microstructure underestimated the location of maximum correlation. This can also be addressed by the influences of the VF. In the texture analysis section, it was concluded that the VF of S predicted by the TLVP model is larger than that found in the experimental macrostructure. If the VF of the simulated macrostructure is larger, then the chance of finding S in the macrostructure is higher, and it correlates at shorter distance with Cube.

In addition to the Cube-S pair, other pairs of orientations were also studied. Results from the comparison of Cube-Goss, Cube-Brass, and Brass-S pairs are demonstrated in Fig. 7-29. Subplot (a) in this figure shows the averaged maximum correlation distance for the Cube-Goss pair. It is seen that the DC model could not accurately predict the correlation distance for this pair. One reason for this is that the VF of both Cube and Goss orientations are rather small, and consequently the possibility of finding a good correlation at a smaller range is low; thus, they will tend to positively correlate at larger distances. The correlation results of Cube-Brass and Brass-S are also shown in subplots (b) and (c). Because the VFs of both Brass and S are very large, it is seen in subplot (c) that the Brass-S pair correlates at a very small distance. Comparisons of the experimental and simulated microstructures also reveal that the correlation length for studied pairs in the simulated macrostructure is generally shorter as compared to the experiments. Additionally, it was found that the correlation length is decreased by increasing the levels of rolling deformation. Correlation relationships of other pairs of orientations (i.e. Cube-Copper, Cube-Taylor, etc.) can also be studied, but because these calculations are expensive and because the VF of Copper and Taylor varies a lot by the amount of deformation, these pairs were not considered.

The amount of correlation for different pairs was also studied. The mean absolute error of correlation intensities is shown in Fig. 7-30. To plot the mean absolute error, the correlation densities for the experimental and simulated microstructures were measured, and the differences between the absolute values of the experimental and simulated correlation densities were attained and reported.

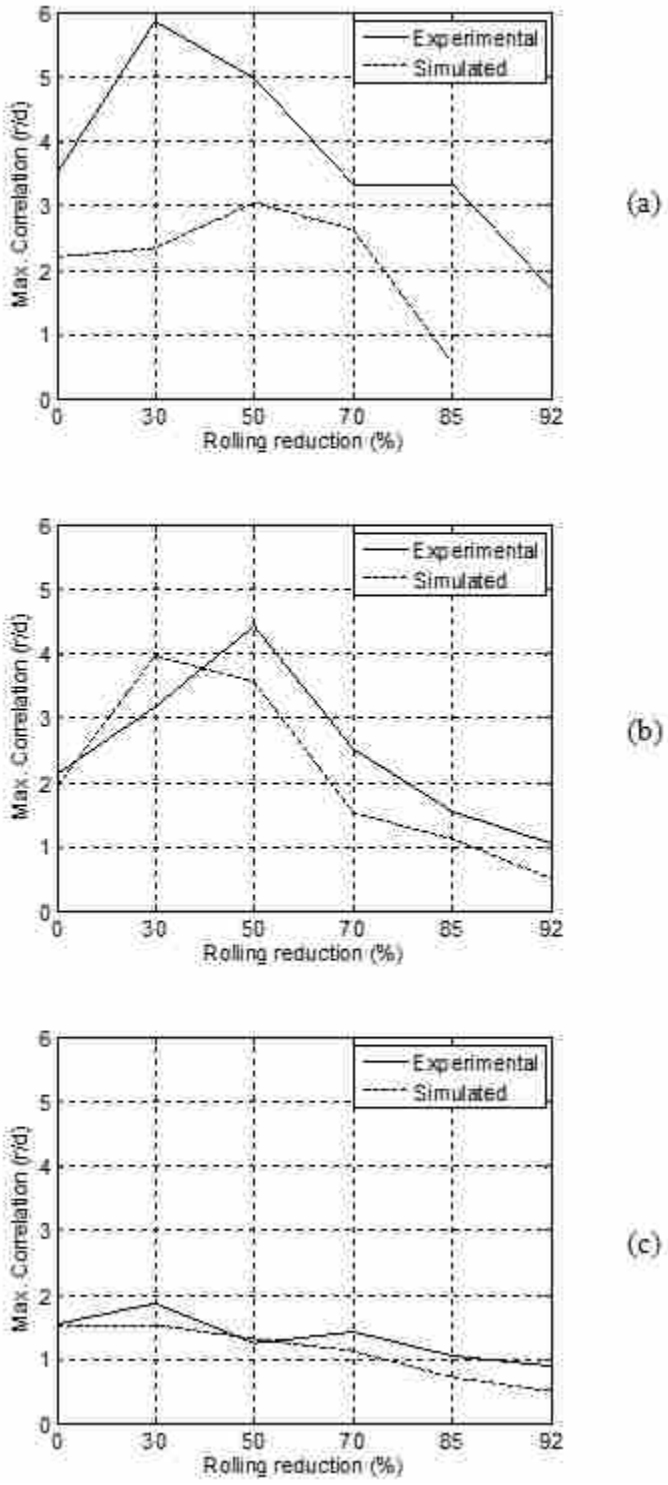

Fig. 7-29: Maximum correlation length for the following pairs: (a) Cube-Goss, (b) Cube-Brass, and (c) Brass-S

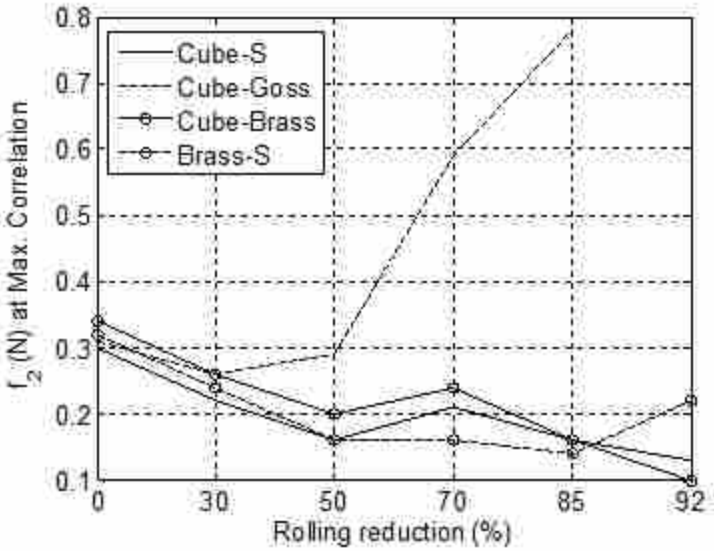

Fig. 7-30: Comparison of the mean absolute error of correlation densities by the amount of cold rolling for the following pairs: (a) Cube-Goss, (b) Cube-Brass, and (c) Brass-S

In general, it was found (i) that the difference between experimental and simulated correlation densities for the Cube-Goss pair is large; (ii) and that by increasing the amounts of deformation, the absolute error is also increased in most of the studied cases.

7.4.2.3 Recovery of the Coherence Length

The 2-point correlation functions, $f(g,g'|r)$ can be used to find the statistical effects of a point located at position x' (with orientation g') upon the properties of the point x (with orientation g), when they are separated by $r = x' - x$. For spherical representative volumes, the r-space $\Psi(r)$, can be expressed as a sphere with radius r_c, where r_c is called the coherence length. If randomly placed vectors of magnitude $|r| \le r_c$ are used to sample the microstructure, there will exist certain coherence or anti-coherence relationships between pairs of orientations. For vectors of magnitude $|r| \ge r_c$, however, these patterns of coherence or anti-coherence are no

longer observed, and the joint probability density is given by the product of probability densities for orientations g and g'. This lack of coherence, or decoupling, defines the coherence length:

$$f_2(g, g' \mid r) = f(g) f(g') \quad \forall \ |r| > r_c \tag{7-5}$$

To study the coherence limit, it is useful to form the average of the absolute value of the normalized PCF statistics, by holding the vector length in all directions constant: $|r_k| = r$. This leads to the magnitude of orientation coherence (either coherence or anti-coherence) at *r (GAO et al. 2006)*:

$$|F(r)| = \frac{\sum_{k=1}^{3} \sum_{i=1}^{N} \sum_{j=1}^{N} \left| \tilde{f}_2(N_i, N_j \mid r_k : |r_k| = r) \right|}{n}; \quad \forall \ n = N \times N - p \tag{7-6}$$

where N_i or N_j indicates the working bin in the tessellated $FZ_{3C/4}$, N is the number of bins in $FZ_{3C/4}$, and p is the number of two-point statistics where $f_2(N_i, N_j \mid r_k) = 0$. The coherence length in the RD or TD can also be obtained by considering $|r_k| = r_{RD}$ or $|r_k| = r_{TD}$ in the above equations.

The selection of bin size to tessellate the $FZ_{3C/4}$ is very important in the calculation time. In this research, a 10 degree bin size was used and a total of 729 bins were included in calculations. A pair of orientations is considered by selecting two orientations at a time. Thus, the normalized PCFs for the simulated and experimental microstructures were calculated $729 \times 729 = 531{,}441$ times. The total calculation time for every section (RD, TD, or ND) and for every level of strain was ~16 hours on a standard PC.

As an example of the RD, TD, and radial coherence plots for the 50% experimentally rolled macrostructure (ND plane) is illustrated in Fig. 7-31.

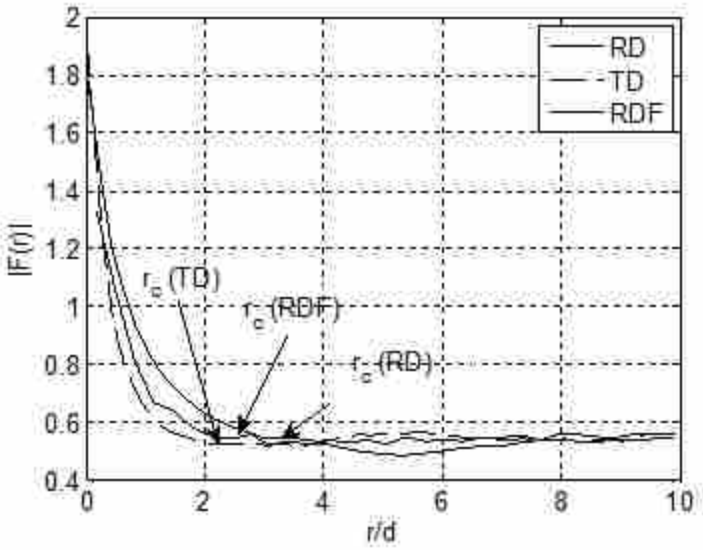

Fig. 7-31: The RD, TD and radial coherence length for the 50% rolled sample cut from the ND section of the experimental microstructure

Different coherence lengths were observed along the RD and TD. The maximum coherence length was defined where the steady region (with no coherence existence) commences. Along the RD the coherence length was 3.42 where as for the TD this was 2.24. Also, the radial coherence length was reported as 2.62 for this case.

The RD, TD, and radial coherence lengths for other sections of the material and at different amounts of strain were measured similarly. The averaged coherence length along RD, TD and radial distributions are shown in Fig. 7-32.

Results from comparison of coherence lengths show that (i) the RD coherence lengths are typically larger; (ii) the DC model can predict the location of the coherence length for smaller amounts of strain, but for reductions above 70% it cannot accurately predict the length of coherence.

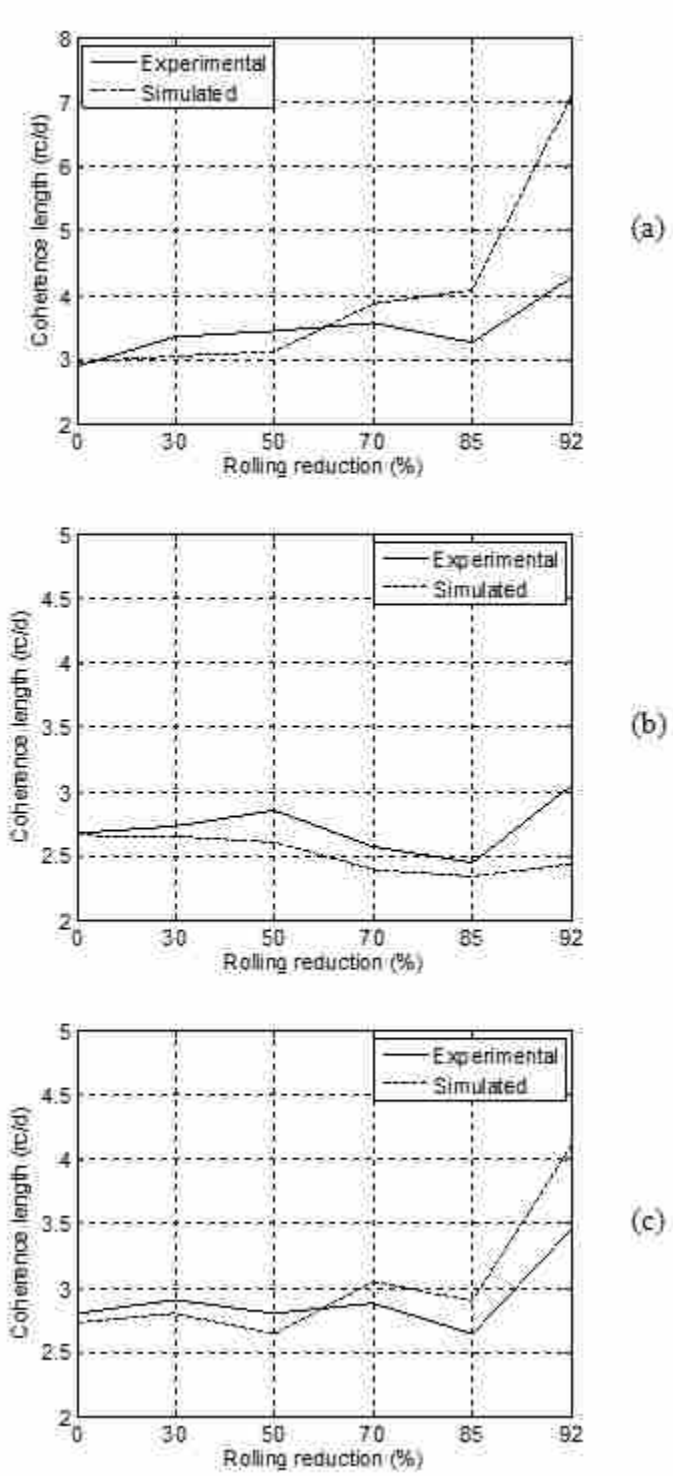

Fig. 7-32: The averaged coherence length along (a) RD, (b) TD, and (c) radial distributions of experimental and simulated microstructures

8 SUMMARY AND CONCLUSIONS

Study the texture analysis of polycrystalline materials (particularly FCC materials) has been the subject of many researches during the past sixty years. In texture analysis, only the orientation of crystallographic grains inside the microstructure is studied. As explained in Sections 2.2.1 and 4.2, orientation distribution function (ODF) is the statistical tool that has been used in the literature to examine the crystallographic texture of materials. Generally, in the process of texture evolution, the ODF is employed to monitor the evolution of orientations based upon the conservation of orientation principle –mostly in FEM models. In such FEM models, a preferred crystal plasticity model is used to incrementally update the location of orientations in the orientation space. Taylor-type models are the most well-used crystal plasticity models developed and utilized in FEM models. There are a few concerns, however, on using FEM models. The most serious problem is that in these models a Lagrangian description of motion is used, and consequently the shape and/or the size of the material volume element changes during the deformation process which leads to a severely distorted mesh at the end of the process. Therefore, at large levels of deformation a remeshing process must be adapted in FEM models. Additionally, the iterative process in FEM models is very expensive in calculation time – especially when a rate-dependent crystal plasticity model is considered. Results from statistical modeling, show that in addition to the texture evolution the evolution of mass particles of grains in the real space should also be considered in any microstructure analysis. Therefore, the

microstructure function, which is a function of position and orientation of grain, can be alternatively used in the examination of the microstructure. To resolve the problems with FEM models, an Eulerian formulation of the problem can be designated. In this way, the evolution of mass particles and orientation of crystallographic grains is studied in an Eulerian coordinate system. This is a unique methodology of examining the microstructure and no such model has been reported in the literature; thus, a new formulation of the problem in the Eulerian format was considered in this research.

The major purpose of this research was to establishing a new Eulerian model that predicts the microstructure evolution of materials under large plastic deformations. To examine the movement, distortion, and rotation of a crystallographic grain in a polycrystalline material, the location of its material particles in the mass space and the amount of rotation of its crystallographic orientation in the orientation space must be considered. Therefore, the microstructure function was used to monitor these changes in both mass and orientation spaces. Mass- and orientation-based continuity models that examine these changes of the grain were derived and validated throughout this research. In the following, the development process of these continuity models is discussed:

- Based upon the conservation of mass principle, the mass-based continuity (MC) model was developed in Eulerian framework.
- This MC model was used to simulate the evolution process of material particles of a two isotropic phase (TIP) material placed under a 2D plane-strain compression test.
- The framework of the MC model was additionally validated against a Lagrangian model with a direct calculation of particle motions. Results show that the accuracy of the MC model is enhanced by choosing a mesh of small size, i.e. 0.075 microns.

- The orientation-based continuity (OC) model was developed based upon the conservation of orientation principle in Eulerian format. To construct the space of orientations for this model, a Taylor-like viscoplastic (TLVP) crystal plasticity model was used to obtain the lattice velocity vectors in the cubic-orthorhombic orientation space, $FZ_{3C/4}$.
- To validate the Eulerian OC model, rolling deformation of a randomly textured aggregate including 1000 random orientations was simulated.
- A Lagrangian model was used for further examination of the OC model. Predicted pole figures and results obtained from the comparison of Lagrangian and Eulerian models confirmed that the bin size has an important effect on the accuracy of the OC model. As the size of the bins decreases, the accuracy of the model and the overall processing time were increased. Results suggested that a reasonable compromise condition is achieved when a 0.5 degree mesh size is chosen for tessellating the $FZ_{3C/4}$.
- Based on the definition of the MF, the MC and OC models were coupled to form the Eulerian double continuity (DC) model.
- It was found that for the case of ordinary DC model, most of bins in the mass and orientation spaces are empty throughout the entire deformation process; therefore, to avoid extensive and un-necessary calculations, an optimized DC model was developed. In the optimized DC model, instead of studying the evolution of the MF in both spaces, grains were studied individually. Further discussion of this method is found in Section 7.2.

- A genetic algorithm (GA) method was later employed to reconstruct a 3D macrostructure such that it becomes statistically equivalent to the experimental macrostructure. An error function that included errors from comparing the ODF and 2-point statistics of experimental and simulated microstructures was considered, and the GA process was terminated with a final error of ~4%, see Section 7.1.3.
- On the experimental part of the work, a polycrystalline high-purity nickel material was used to corroborate results from simulated the rolling process using the optimized DC model. Appropriate rolling testing was conducted, and the macrostructure of the cold rolled material with levels of 0, 30, 50, 70, 85, and 92% reductions were obtained.
- Lastly, the optimized DC model was used to simulate the rolling process and predict a final 3D microstructure for different levels of deformation.

In comparison of experimental and simulated results, textural and statistical analyses were carried out to obtain the accuracy of the DC model in the prediction of the final texture/microstructure. On the texture analysis, stability of ideal orientations was examined. Additionally, pole figures, fibre plots, and ODF section plots were provided. As a general conclusion from the texture analysis of experimental and simulated microstructures, it was found that, in overall, by increasing the amounts of cold rolling: (i) the densities of Cube and Goss do not change and good predictions were obtained by the proposed model, (ii) densities of Brass, Copper, Taylor, and S are increased and the precision of the TLVP model is decreased. The largest differences were found for Copper, Taylor, and S orientations. The TLVP model overestimates the densities of these orientations. Reasons for the deficiencies of the TLVP model

are explained by the stability analysis of these orientations. Basically, it was found that in the TLVP model the most stable end-orientation is the Taylor orientation. The divergence of Brass, Copper, and S are also largely negative, which causes a faster convergence of orientations towards these orientations and a faster accumulation of density of these orientations.

On the statistical analysis of the microstructures, volume fractions of ideal orientations were obtained. Analysis of the volume fraction of these orientations confirmed the texture results. Moreover, the autocorrelation length of Cube, Brass and S were studied. General conclusions from comparisons of autocorrelation lengths of Cube, Brass, and S are that (i) grains with Cube orientation cohere only at shorter distances, which implies that the Cube grains are generally smaller in size; (iii) RD autocorrelation length of the simulated microstructure is always larger than the one found in the experimental microstructure. This suggests that grains in the simulated microstructure can freely deform, but in the physical conditions of actual deformation they are not allowed to; (iv) grains with the S orientation are expected to be more elongated in shape as their RD autocorrelation length is larger than those for Cube and Brass. Pair-correlation relations of Cube-Goss, Cube-Brass, Cube-S, and Brass-S were also studied. In general, from the studied pair-correlation relations it was found (i) that the difference between experimental and simulated correlation lengths for the Cube-Goss pair is quite large, while the correlation length of the Brass-S pair is relatively small. This can be understood by the amount of VFs of orientations in each pair. VFs of Cube and Goss are very small as compared to the larger VFs of Brass and S. Having larger amounts of VF increases the possibility of finding that specific orientation in the macrostructure, and increases the chance of occurrence of large VF orientations at a shorter correlation range; and (ii) by increasing the amounts of deformation, the pair-correlation distance is decreased. Lastly, the relationship of correlation length and the

amount of cold rolling was studied. It was found that the length of coherency varies with the selected bin size of the orientation space, and that the DC model can predict the location of the coherence length for smaller amounts of strain, but for reductions above ~70% it cannot accurately predict the length of coherence. This may be answered by considering the effects from the nature of experimental testing. The main issue with the experimental rolling results was that at large levels of deformation, cell-blocks and dislocation bands are developed. As a result, subdivision of grains will occur in the experimental macrostructure and change the orientation of subgrains. The grain fragmentation phenomenon was not considered in this research and obviously most of the calculation errors can be explained by physical phenomena not considered in the DC model. Perhaps, in the feature and by further improvements in FEM models, the DC model can be incorporated with these FEM models to give a better prediction of microstructure evolution.

As a final conclusion, after comparisons of textural and statistical results from the experimental and simulated microstructures, it is necessary to again mention that although many factors (e.g. interactions of grains, subdivision of grains, frictional and additional forces in rolling, and etc.) were not considered in the DC model, this model was not only able to satisfactorily predict the location of coherency and correlation of studied orientations in the simulated microstructure, but also perform the calculations in a shorter time as compared to Lagrangian models. The main advantage of the Eulerian DC model over Lagrangian models was that, based on the TLVP model, it was required to calculate the orientation velocity field only once. The obtained velocity field can be used for examination of all types of FCC materials by considering a scaling factor to adjust the slip hardening parameters as explained in Section 3.2.3.

Another benefit of using the DC model was that FFTs can be employed for faster computation the 2-point statistics required for the statistical analysis.

Finally, for the future work, it is recommended: (i) that other types of crystal plasticity models, more specifically the statistical modeling with including the localization effects, are employed and the advantages and limitations of these models on the microstructure predictions are studied; (ii) that other types of materials (e.g. FCC, BCC, or HCP materials) or other types of deformation processes are considered to examine the accuracy of the MC model on the prediction of more complicated deformed microstructures; (iii) that improve the Eulerian-based MC model with coupling this model with other models to include physical phenomena and other statistical futures of the microstructure that in reality exist in the microstructure of polycrystalline materials.

REFRENCES

ADAMS, B. L., and D. P. FIELD, 1991 A statistical theroy of creep in polycrystalline materials. Acta Metallurgica et Materialia **39:** 2405-2417.

ADAMS, B. L., X. GAO and S. R. KALIDINDI, 2005a Finite approximations to the second-order properties closure in single phase polycrystals. Acta Materialia **53:** 3563-3577.

ADAMS, B. L., A. HENRIE, B. HENRIE, M. LYONS, S. R. KALIDINDI *et al.*, 2001 Microstructure-sensitive design of a compliant beam. Journal of the Mechanics and Physics of Solids **49:** 1639-1663.

ADAMS, B. L., S. R. KALIDINDI and D. T. FULLWOOD, 2005b *Microstructure Sensitive Design for Performance Optimization*. BYU Academic Publishing.

ADAMS, B. L., M. LYONS and B. HENRIE, 2004 Microstructures by design: linear problems in elastic–plastic design. International Journal of Plasticity **20:** 1577–1602-1577–1602.

ADAMS, B. L., A. MOLINARI and G. R. CANOVA, 1989 A statistical formulation of viscoplastic behavior in heterogeneous polycrystals. Textures and Microstructures **11:** 57–71-57–71.

AHMADI, S., B. L. ADAMS and D. T. FULLWOOD, 2009 An Eulerian-Based Formulation for Studying the Evolution of the Microstructure under Plastic Deformations. Computers, Materials & Continua (CMC) **14:** 141-169.

ANAND, L., and S. R. KALIDINDI, 1994 The process of shear band formation in plane strain compression of fcc metals: Effects of crystallographic texture. Mechanics of Materials **17:** 223-223.

ARZAGHI, M., B. BEAUSIR and L. TOTH, 2009 Contribution of non-octahedral slip to texture evolution of fcc polycrystals in simple shear. Acta Materialia **57:** Acta Materialia.

ASARO, R. J., and A. NEEDLEMAN, 1985 Overview no. 42 Texture development and strain hardening in rate dependent polycrystals. Acta Metallurgica **33:** 923-953.

ASTM, 2003 Standard Test Methods for Tension Testing of Metallic Materials, pp. ASTM International, West Conshohocken, PA.

BACHU, V., and S. R. KALIDINDI, 1998 On the accuracy of the predictions of texture evolution by the finite element technique for fcc polycrystals. Materials Science and Engineering: A **257:** 108-117.

BEAUDOIN, A. J., H. MECKING and U. F. KOCKS, 1996 Development of localized orientation gradients in FCC polycrystals. Philosophical Magazine A **73:** 1503-1517.

BEAUSIR, B., L. S. TOTH and K. W. NEALE, 2007 Ideal orientations and persistence characteristics of hexagonal close packed crystals in simple shear. Acta Materialia **55:** 2695-2705.

BECKER, R., and S. PANCHANADEESWARAN, 1995 Effects of grain interactions on deformation and local texture in polycrystals. Acta Metallurgica et Materialia **43:** 2701-2719.

BERAN, M. J., 1968 *Statistical Continuum Theories*. John Wiley and Sons, Interscience, New York.

BERAN, M. J., and J. MOLYNEUX, 1966 Use of classical variational principles to determine bounds for the effective bulk modulus in heterogeneous media. Quarterly of Applied Mathematics **24:** 107-118.

BISHOP, J. F. W., and R. HILL, 1951 A theoretical derivation of the plastic properties of a polycrystalline faced-centered metal. Phil Mag **42:** 1298.

BRONKHORST, C. A., S. R. KALIDINDI and L. ANAND, 1992 Polycrystalline Plasticity and the Evolution of Crystallographic Texture in FCC Metals. Philosophical Transactions of the Royal Society: Physical and Engineering Sciences (1990-1995) **341:** 443-477.

BUNGE, H. J., 1993 *Texture analysis in materials science: Mathematical Methods*. Cuvillier Verlag.

BUNGE, H. J., and C. ESLING, 1984 Testure developement by plastic deformation. Scripta Metallurgica **18:** 191-195.

BUNGE, H. J., C. ESLING, E. DAHLEM and H. KLEIN, 1986 The Development of Deformation Textures Described by an Orientation Flow Field. Textures and Microstructures **6:** 181–200-181–200.

BUNGE, H. J., and R. A. SCHWARZER, 2001 Orientation Stereology—A New Branch in Texture Research. Advanced Engineering Materials **3:** 25-39.

CANOVA, G., U. F. KOCKS and J. J. JONAS, 1984 Acta Metallurgica **32:** 211.

CHEN, H. S., A. GODFREY, N. HANSEN, J. X. XIE and Q. LIU, 2008 Microstructure–grain orientation relationship in coarse grain nickel cold-rolled to large strain. Materials Science and Engineering: A **483-484:** 157-160.

CHOI, S. H., K. H. OH, J. H. CHO, K. CHUNG and F. BARLAT, 2000 Texture evolution of FCC sheet metals during deep drawing process. International Journal of Mechanical Sciences **42:** 1571-1592.

CLEMENT, A., 1982 Prediction of deformation texture using a physical principle of conservation. Materials Science and Engineering **55:** 203-210.

COULOMB, A. C. A. P., 1979 Eulerian Simulation of Deformation Textures. Scripta Metallurgica **13:** 899-901.

DEDERICHS, P. H., and R. ZELLER, 1973 Variational treatment of the elastic constants of disordered materials Zeitschrift für Physik A Hadrons and Nuclei.

DELANNAY, L., S. R. KALIDINDI and P. VAN HOUTTE, 2002 Quantitative prediction of textures in aluminium cold rolled to moderate strains. Materials Science and Engineering A **336:** 233-244.

DILLAMORE, I. L., and W. T. ROBERTS, 1964 Rolling textures in f.c.c. and b.c.c. metals. Acta Metallurgica **12:** 281-293.

FROMM, B. S., 2008 Incorporating grain size effects in Taylor crystal plasticity, pp.

FROMM, B. S., B. L. ADAMS, S. AHMADI and M. KNEZEVIC, 2009 Grain size and orientation distributions: Application to yielding of α-titanium. Acta Materialia **57:** 2339-2348.

FULLWOOD, D. T., S. AHMADI and B. L. ADAMS, 2009a Spectral formulation of statistical theory of viscoplasticity, pp. in *The International Symposium on Plasticity*, St. Thomas, Virgin Islands.

FULLWOOD, D. T., S. R. KALIDINDI, B. L. ADAMS and S. AHMADI, 2009b A Discrete Fourier Transform Framework for Localization Relations. Computers, Materials & Continua **9:** 25-40.

FULLWOOD, D. T., S. R. KALIDINDI, S. R. NIEZGODA, A. FAST and N. HAMPSON, 2008 Gradient-based microstructure reconstructions from distributions using fast Fourier transforms. Materials Science and Engineering: A **494:** 68-72.

FULLWOOD, D. T., S. R. NIEZGODA, B. L. ADAMS and S. R. KALIDINDI, 2009c Microstructure sensitive design for performance optimization. Progress in Materials Science.

GAMBIN, W., and F. BARLAT, 1997 Modeling of deformation texture development based on rate independent crystal plasticity. International Journal of Plasticity **13:** 75–86.

GAO, X., C. P. PRZYBYLA and B. L. ADAMS, 2006 Methodology for recovering and analyzing two-point pair correlation functions in polycrystalline materials. Metallurgical and Materials Transactions A **37:** 2379-2387.

GARMESTANI, H., S. LIN, B. L. ADAMS and S. AHZI, 2001 Statistical continuum theory for large plastic deformation of polycrystalline materials. Journal of the Mechanics and Physics of Solids **49:** 589-607.

GILORMINI, P., L. S. TOTH and J. J. JONAS, 1990 An Analytic Method for the Prediction of ODFS with Application to the Shear of FCC Polycrystals. Proceedings: Mathematical and Physical Sciences **430:** 489–507-489–507.

GODFREY, A., D. JUUL JENSEN and N. HANSEN, 1998 Slip pattern, microstructure and local crystallography in an aluminuim single crystal of copper orientaion {112}<111>. Acta Materialia **46:** 835-848.

HANSEN, N., and D. J. JENSEN, 1999 Development of microstructure in FCC metals during cold work. Philosophical Transactions: Mathematical, Physical and Engineering Sciences **357:** 1447–1469.

HANSEN, N., H. NAAMAN, R. TALREJA and D. JUUL JENSEN, 1987 Development of Deformation Textures in Polycrystalline Copper Experiments and Model Predictions. Textures and Microstructures **7:** 149-170.

HICKS, N. J., 1965 *Notes on differential geometry*. Van Nostrand Reinhold Company.

HIELSCHER, R., and H. SCHAEBEN, 2008 A novel pole figure inversion method: specification of the MTEX algorithm. Journal of Applied Crystallography **41:** 1024-1037.

HIRSCH, J., and K. LUCKE, 1988a Mechanism of deformation and development of rolling textures in polycrystalline f.c.c. metals—II. Simulation and interpretation of experiments on the basis of Taylor-type theories. Acta Metallurgica **36:** 2883-2904.

HIRSCH, J., and K. LUCKE, 1988b Mechanism of deformation and development of rolling textures in polycrystalline f.c.c. metals - I. Description of rolling texture development in homogeneous CuZn alloys. Acta Metallurgica **36:** 2863-2882.

HIRSCH, J., and K. LUCKE, 1988c Mechanism of deformation and development of rolling textures in polycrystalline of experiments on the basis of Taylor-type theories. Acta Materialia **36:** 2883-2904.

HIRSCH, J., K. LUCKE and M. HATHERLY, 1988 Mechanism of deformation and development of rolling textures in polycrystalline f.c.c. Metals—III. The influence of slip inhomogeneities and twinning. Acta Metallurgica **36:** 2905-2927.

HONNEFF, H., and H. MECKING, 1978, pp. 265 in *Proc. 5th Int. Conf. on Textures of Materials, ICOTOM 5*.

HORTON, D., C. B. THOMSON and V. RANDLE, 1995 Aspects of twinning and grain growth in high purity and commercially pure nickel. Materials Science and Engineering A **203:** 408-414.

HOSFORD, W. F., and R. M. CADDELL, 2007 *Metal Forming: Mechanics and Metallurgy*. Cambridge University Press.

HU, H., and R. S. CLINE, 1966 Deformation textures of metals. In: Margolin H, editor. Recrystallization, grain growth and textures. Metals Park: American Society for Metals**:** 295–367.

HUGHES, D. A., and N. HANSEN, 1993 Microstructural evolution in nickel during rolling from intermediate to large strains. Metallurgical Transactions A **24:** 2022-2037.

HUGHES, D. A., and N. HANSEN, 1995 High angle boundaries and orientation distributions at large strains. Scripta Metallurgica et Materialia **33:** 315-321.

HUGHES, D. A., and N. HANSEN, 2000 Microstructure and strength of nickel at large strains. Acta Materialia **48:** 2985–3004.

HUMPHREYS, F. J., and M. HATHERLY, 2004 *Recrystallization and related annealing*. Elsevier.

HUTCHINSON, J. W., 1976 Bounds and Self-Consistent Estimates for Creep of Polycrystalline Materials. Proceedings of the Royal Society of London. Series A, Mathematical and Physical Sciences (1934-1990) **348:** 101-127.

IRGENS, F., 2008 *Continuum Mechanics*. Springer-Verlag Berlin Heidelberg.

JONAS, J. J., and J. BACZMANSKI, 1996 Texture development during the torsion testing of ?-iron and two IF steels. Acta Materialia **44:** 4273-4288.

KALIDINDI, S. R., 2001 Modeling anisotropic strain hardening and deformation textures in low stacking fault energy fcc metals. International Journal of Plasticity **17:** 837-860.

KALIDINDI, S. R., and L. ANAND, 1992 An approximate procedure for predicting the evolution of crystallographic texture in bulk deformation processing of fcc metals. International Journal of Mechanical Sciences **34:** 309-329.

KALIDINDI, S. R., and L. ANAND, 1994 Macroscopic shape change and evolution of crystallographic texture in pre-textured FCC metals. Journal of the Mechanics and Physics of Solids **42:** 459-490.

KALIDINDI, S. R., M. BINCI, J. R. HOUSKAMP, M. LYONS, D. T. FULLWOOD *et al.*, 2004 Microstructure sensitive design of an orthotropic plate subjected to tensile load. International Journal of Plasticity **20:** 1561-1575.

KALIDINDI, S. R., C. A. BRONKHORST and L. ANAND, 1992 Crystallographic texture evolution in bulk deformation processing of fcc metals. Journal of the Mechanics and Physics of Solids **40:** 537-569.

KALIDINDI, S. R., H. DUVVURU and M. KNEZEVIC, 2006 Spectral calibration of crystal plasticity models. Acta Materialia **54:** 1795-1804.

KALLEND, J. S., and G. J. DAVIES, 1972 The Development of Texture in Copper and Copper-Zinc Alloys, pp. 51–69 in *Texture*.

KNEZEVIC, M., S. R. KALIDINDI and D. T. FULLWOOD, 2008 Computationally efficient database and spectral interpolation for fully plastic Taylor-type crystal plasticity calculations of face-centered cubic polycrystals. International Journal of Plasticity **24:** 1264-1276.

KREISS, H. O., and J. LORENZ, 2004 Initial Boundary Value Problems and NavierStokes Equations, pp. Society for Industrial and Applied Mathematics.

KRONER, E., 1967 Elastic moduli of perfectly disordered composite materials. Journal of the Mechanics and Physics of Solids **15:** 319–329-319–329.

KRONER, E., 1977 Bounds for effective elastic moduli of disordered materials. Journal of the Mechanics and Physics of Solids **25:** 137–155-137–155.

KRONER, E., 1986 *Statistical modeling*. Elsevier Science Publishers.

KUMAR, A., and P. R. DAWSON, 1998 Modeling crystallographic texture evolution with finite elements over non-Eulerian orientation spaces. Compur Methods in Applied Mechancis and Engineering **153:** 259-302.

KUMAR, A., and P. R. DAWSON, 2009 Dynamics of texture evolution in face-centered cubic polycrystals. Journal of the Mechanics and Physics of Solids **57:** 422-445.

LAI, M. W., D. RUBIN and E. KREMPL, 1993 Introduction to Continuum Mechanics, pp. Butterworth-Heinemann Ltd.

LAI, W. M., E. KREMPL and D. RUBIN, 2009 *Introduction to continuum mechanics*. Butterworth Heinemann.

LEBENSOHN, R. A., 1999 Modelling the role of local correlations in polycrystal plasticity using viscoplastic self-consistent schemes. Modelling and Simulation in Materials Science and Engineering **7:** 739.

LEBENSOHN, R. A., and T. LEFFERS, 1999 The rules for the lattice rotation accompanying slip as derived from a self-consistent model. Textures and Microstructures **31:** 217–230.

LEBENSOHN, R. A., C. N. TOMÉ and P. P. CASTAÑEDA, 2007 Self-consistent modelling of the mechanical behaviour of viscoplastic polycrystals incorporating intragranular field fluctuations. Philosophical Magazine **87:** 4287-4322.

LEBENSOHN, R. A., P. A. TURNER, J. W. SIGNORELLI, G. R. CANOVA and C. N. TOME, 1998 Calculation of intergranular stresses based on a large-strain viscoplastic self-consistent polycrystal model. Modelling and Simulation in Materials Science and Engineering **6:** 447.

LEFFERS, T., 1968 Computer simulation of the plastic deformation in face-centred cubic polycrystals and the rolling texture derived. physica Status Solidi (B): Basic Research **25:** 337-344.

LEFFERS, T., 1979 A modified Sachs approach to the plastic deformation of polycrystals as a realistic alternative to the Taylor model. In: Haasen P et al., editors. Strength of metals and alloys. Oxford: Pergamon Press**:** 769-774.

LEFFERS, T., 2001 A model for rolling deformation with grain subdivision. Part I: The initial stage. International Journal of Plasticity **17:** 469-489.

LEFFERS, T., 2006 Computer simulation of the plastic deformation in face-centred cubic polycrystals and the rolling texture derived. physica Status Solidi (B): Basic Research **25:** 337-344.

LEFFERS, T., and R. K. RAY, 2009 The brass-type texture and its deviation from the copper-type texture. Progress in Materials Science **54:** 351-396.

LENARD, J. G., 2007 *Primer on Flat Rolling*. Elsevier.

LI, D. S., and H. GARMESTANI, 2004 Prediction of Texture Coefficients Evolution During Bulk Deformation, pp. 131 in *Processing and fabrication of advanced materials XII: proceedings of a symposium organized by ASM International, Materials Park, Ohio, USA, 13-15 October 2003, Pittsburgh, Pennsylvania, USA*. ASM International.

LI, D. S., H. GARMESTANI and B. L. ADAMS, 2005 A texture evolution model in cubic-orthotropic polycrystalline system. International Journal of Plasticity **21:** 1591-1617.

LI, D. S., H. GARMESTANI and S. SCHOENFELD, 2003 Evolution of crystal orientation distribution coefficients during plastic deformation. Scripta Materialia **49:** 867–872-867–872.

LIN, S., H. GARMESTANI and B. L. ADAMS, 2000 The evolution of probability functions in an inelasticly deforming two-phase medium. International Journal of Solids and Structures **37:** 423-434.

LYONS, M., and B. L. ADAMS, 2004 Gradient-based non-linear microstructure design. Journal of the Mechanics and Physics of Solids **52:** 2569-2586.

MIKA, D. P., and P. R. DAWSON, 1998 Effects of grain interaction on deformation in polycrystals. Materials Science & Engineering A **257:** 62-76.

MIKA, D. P., and P. R. DAWSON, 1999 Polycrystal plasticity modeling of intracrystalline boundary textures. Acta Materialia **47:** 1355-1369.

MITCHELL, M., 1996 *An Introduction to Genetic Algorithms*. The MIT Press.

MOLINARI, A., 1999 Extensions of the self-consistent tangent model. Modelling and Simulation in Materials Science and Engineering **7:** 683.

MOLINARI, A., S. AHZI and R. KOUDDANE, 1997 On the self-consistent modeling of elastic-plastic behavior of polycrystals. Mechanics of Materials **26:** 43-62.

MOLINARI, A., G. R. CANOVA and S. AHZI, 1987 A self consistent approach of the large deformation polycrystal viscoplasticity. Acta Metallurgica **35:** 2983–2994-2983–2994.

MORAWIEC, A., 2004 *Orientations and rotations: computations in crystallographic textures*. Springer-Verlag Berlin Heidelberg.

MORAWIEC, A., and D. P. FIELD, 1996 Rodrigues parameterization for orientation and misorientation distributions. Philosophical Magazine A **73:** 1113-1130.

MORAWIEC, A., K. WIERZBANOWSKI, J. JURA and J. BACZMANSKI, 1991 Prediction of deformation texture in polycrystals. Philosophical Magazine A **64:** 1251-1263.

NAIR, S., 2009 *Intorduction to continuum mechanics*. Cambridge University Press.

OIM-TSL, 2007 *OIM Analysis (version 5.2)*. developed by TSL-EDAX at: http://www.tsl-oim.com/.

PARK, N. K., and B. A. PARKER, 1989 The development of the deformed microstructure in commercially pure nickel☆. Materials Science and Engineering: A **113:** 431-439.

PEDERSEN, O. B., and T. LEFFERS, 1987 Constitutive relations and their physical basis. proceedings of the 8th Risø International Symposium on Metallurgy and Meterials Science**:** 147-172.

RAY, R. K., 1995 Rolling textures of pure nickel, nickel-iron and nickel-cobalt alloys. Acta Metallurgica et Materialia **43:** 3861-3872.

REDDY, J. N., 2008 *An introduction to continuum mechanics*. Cambridge University Press.

RITZ, H., and P. R. DAWSON, 2009 Sensitivity to grain discretization of the simulated crystal stress distributions in FCC polycrystals. Modelling and Simulation in Materials Science and Engineering **17:** 015001.

SACHS, G., 1928 Zur Ableitung einer Fliessbedingung. Zeichschrift der Verein deutscher Ingenieur **72:** 734-736.

SARMA, G. B., and P. R. DAWSON, 1996 Texture predictions using a polycrystal plasticity model incorporating neighbor interactions. International Journal of Plasticity **12:** 1023-1054.

SAVOIE, J., Y. ZHOU, J. J. JONAS and S. MACEWEN, 1996 Textures induced by tension and deep drawing in aluminum sheets. Acta Materialia **44:** 587-605.

SCHUTZ, B. F., 1985 *A first course in general relativity*. Cambridge University Press.

TAYLOR, G. I., 1938 Plastic strain in metals. J. Inst. Metal **72:** 307-325.

TOME, C. N., 1999 Self-consistent polycrystal models: a directional compliance criterion to describe grain interactions. Modelling and Simulation in Materials Science and Engineering **7:** 723-738.

TOTH, L. S., P. GILORMINI and J. J. JONAS, 1988 Effect of rate sensitivity on the stability of torsion textures Acta Metallurgica **36:** 3077-3091.

TOTH, L. S., J. J. JONAS, D. DANIEL and R. K. RAY, 1990 Development of ferrite rolling textures in low and extra low carbon steels. Metallurgical and Materials Transactions A **21:** 2985-3000.

VAN HOUTTE, P., 1978 Simulation of the rolling and shear texture of brass by the Taylor theory adapted for mechanical twinning. Acta Metallurgica **26:** 591-604.

VAN HOUTTE, P., L. DELANNAY and S. R. KALIDINDI, 2002 Comparison of two grain interaction models for polycrystal plasticity and deformation texture prediction. International Journal of Plasticity **18:** 359–377-359–377.

VAN HOUTTE, P., L. DELANNAY and I. SAMAJDAR, 1999 Quantitative prediction of cold rolling textures in low-carbon steel by means of the LAMEL model. Textures andMicrostructures **31:** 109-149.

VAN HOUTTE, P., S. LI, M. SEEFELDT and L. DELANNAY, 2005 Deformation texture prediction: from the Taylor model to the advanced Lamel model. International journal of plasticity **21:** 589–624.

VANHOUTTE, P., A. KANJARLA, A. VAN BAEL, M. SEEFELDT and L. DELANNAY, 2006 Multiscale modelling of the plastic anisotropy and deformation texture of polycrystalline materials. European Journal of Mechanics - A/Solids **25:** 634-648.

WANG, H., P. D. WU, C. N. TOMÉ and Y. HUANG, 2010 A finite strain elastic–viscoplastic self-consistent model for polycrystalline materials. Journal of the Mechanics and Physics of Solids **58:** 594-612.

WASSERMANN, G., 1963 Der Einfluss mechanischer Zwillingsbildung auf die Entstehung der Walztexturen kubisch flächenzentrierter Metalle. Z Metallkde **54:** 61-65.

WIERZBANOWSKI, K., S. AHZI, A. HIHI and M. BERVEILLER, 1986 Rolling Textures Predicted by the Elasto–Plastic Self-Consistent Model. Crystal Research and Technology **21:** 395–406-395–406.

ZHOU, Y., J. J. JONAS and K. W. NEALE, 1996 Behaviour of initial texture components during the plane strain drawing of fcc sheet metals. Acta Materialia **44:** 607–619-607–619.

ZHOU, Y., L. S. TOTH and K. W. NEALE, 1992 On the stability of the ideal orientations of rolling textures for F.C.C. polycrystals. Acta Metallurgica et Materialia **40:** 3179-3193.

APPENDIX A CONTINUITY EQUATION IN THE MASS SPACE

Based upon the conservation of mass principle, a continuity equation in the real space is presented here. We are interested to formulate the continuity equation in the Eulerian coordinate system, thus a spatial description of the material time derivative of a function, $D\phi/Dt$, can be shown as (LAI *et al.* 1993):

$$\frac{D\phi}{Dt} = \left(\frac{\partial \phi}{\partial t}\right)_{X=const} = \left(\frac{\partial \phi}{\partial t}\right)_{x=const} + \left(\frac{\partial x_i}{\partial t}\right)_{X=const} \frac{\partial \phi}{\partial x_i} = \left(\frac{\partial \phi}{\partial t}\right)_{x=const} + v_i \frac{\partial \phi}{\partial x_i} \tag{A-1}$$

where x represents the position of a material point at time t with regard to a spatial (or Eulerian) coordinate system, and X denotes the position of that material point at the beginning of the process ($t=0$). The velocity of material point moving in the microstructure is shown as v.

Now if we take an arbitrary volume denoted by Ω, and assume that the bounding closed surface of this region be continuous and denoted by Γ, using the spatial description of the material time derivative, it can be shown that the time derivative of the volume integral over the mass density $\rho(x,t)$ is given by:

$$\frac{D}{Dt}\int_{\Omega} \rho dx = \frac{d}{dt}\int_{\Omega} \rho dx + \oint_{\Gamma} \rho v.\hat{n} ds \tag{A-2}$$

The principle of conservation of mass for a material region requires that the amount of mass over the entire region does not change with the passage of time; therefore the material derivative of mass density over this region must be zero and we have:

$$\frac{d}{dt}\int_{\Omega}\rho dx = -\oint_{\Gamma}\rho v.\hat{n}ds \tag{A-3}$$

This equation is known as the control-volume formulation of the conservation of mass principle. Converting the surface integral to a volume integral by means of the divergence theorem, we obtain:

$$\int_{\Omega}\left[\frac{\partial\rho}{\partial t} + div(\rho v)\right]dx = 0 \tag{A-4}$$

Since this equation must be valid for any arbitrary volume in the mass space, the integral is vanished, and the local form of the conservation of mass principle can be formulated as:

$$\frac{\partial\rho}{\partial t} + div(\rho v) = 0 \tag{A-5}$$

This equation, called the continuity equation, expresses local conservation of mass at any point in a continuous medium.

APPENDIX B FORWARD-BACKWARD FINITE DIFFERENCE SCHEME

The finite difference method that is used in computation of partial derivatives presented in continuity equations is explained by a simple example here. Suppose that we have a one-dimensional MF, as in Table B-1. The MF is taken to be 0 for phase 1 and 1 for phase 2. Furthermore, we suppose that a positive velocity is applied and it deforms the MF such that it moves the MF one bin to the right. Then, for instance for the mass-based continuity equation, Eq. (5-5) is simplified to $\Delta M = -v(x)\left(dM(x)/dx\right)\Delta t$. By assuming that $\Delta t = 1$ and that $\Delta x = 1$, for a positive velocity everywhere in the domain we have $v = 1$; Thus the only undetermined term is the partial derivatives for which a forward or backward FDM can be used. As we know the forward FDM adopted for the MF has the form $M_i' = \left(M_{i+1} - M_i\right)/\Delta x$, and the backward difference has this form: $M_i' = \left(M_i - M_{i-1}\right)/\Delta x$. Therefore, to find the final MF based upon this simplified iteration scheme we will have: $M_f = M_i - vM'\Delta t$. Table B-1 shows the final MF calculated by the forward and backward differences for a positive velocity. The final MF calculated by the forward difference gives improper values for the MF and it cannot be used for positive velocities; however, the MF predicted by the forward FDM shows that phase 2 is moving to the right under positive velocities.

Table B-1: An example of applying forward/backward differences for positive velocities

M_i	0	0	1	1	1	0	0
dM/dx (forward)	0	1	0	0	-1	0	
M_f (forward)	0	-1	1	1	2	0	
dM/dx (backward)		0	1	0	0	-1	0
M_f (backward)		0	0	1	1	1	0

Similarly it can be shown that the forward difference method can be used for negative velocities.

APPENDIX C CONTINUITY EQUATION IN THE ORIENTATION SPACE

In this section, the continuity equation for orientations is formulated. The continuity equation for orientations is expressed as:

$$\frac{\partial f}{\partial t} + div(fw) = 0 \tag{C-1}$$

where f is the ODF and w is the velocity vector in the orientation space. The idea here is to find the divergence term in the Euler angle workspace. The EAS is taken as a Riemannian manifold and the divergence is obtained. In a Riemannian manifold, the covariant derivative can be used to find the differentiation of a vector field, with t^i components, on the manifold (HICKS 1965; SCHUTZ 1985):

$$t^i_{;j} = \frac{\partial t_i}{\partial x_j} + \Gamma^i_{jk} t^k \tag{C-2}$$

where Γ^i_{jk} are the Christoffel symbols having a unique canonical connection, called the Levi-Civita connection, with the coordinate systems on the manifold (MORAWIEC 2004):

$$\Gamma^i_{jk} = \frac{1}{2} g^{im} \left(\frac{\partial g_{km}}{\partial x^j} + \frac{\partial g_{im}}{\partial x^k} - \frac{\partial g_{jk}}{\partial x^m} \right) \tag{C-3}$$

In this equation, g^{ij} is the covariant form of the metric tensor, g_{ij}, and its components are defined by $g^{ij}g_{jk} = \delta^{i}{}_{k}$ where $\delta^{i}{}_{k}$ is the Kronecker delta taking 1 if $i=k$, and 0 otherwise.

For Euler angles the components of the metric tensor and its covariant tensor, g^{ij}, are:

$$g_{ij} = \frac{1}{4c}\left(\delta_{ij} + 2\delta_{1(i}\delta_{j)3}\cos\Phi\right)$$
$$g^{ij} = \frac{4c}{\sin^2\Phi}\left(\delta^{ij} - 2\delta^{1(i}\delta^{j)3}\cos\Phi - \delta^{i2}\delta^{j2}\cos^2\Phi\right) \tag{C-4}$$

where $c = \pi^{4/3}$ and $\delta_{i(j}\delta_{k)l} = \frac{1}{2}\left(\delta_{ij}\delta_{kl} + \delta_{ik}\delta_{jl}\right)$. Similarly $\delta^{i(j}\delta^{k)l} = \frac{1}{2}\left(\delta^{ij}\delta^{kl} + \delta^{ik}\delta^{jl}\right)$. The Christoffel symbols are:

$$\Gamma^{i}_{jk} = \frac{1}{\sin\Phi}\left(\left(\delta^{i1}\cos\Phi - \delta^{i3}\right)\delta_{1(j}\delta_{k)2} + \left(\delta^{i3}\cos\Phi - \delta^{i1}\right)\delta_{2(k}\delta_{j)3}\right) + \delta^{i2}\delta_{1(j}\delta_{k)3}\sin\Phi \tag{C-5}$$

Representing the orientation flow field as $J = fw$, one can find the divergence term in Eq. (C-1) based upon the definition of the covariant derivative: $div(J) = J^{i}{}_{;i}$. Using Eq. (C-2) the divergence can be shown in the form of Christoffel symbols in the EAS:

$$div(J) = J^{i}{}_{;i} = \frac{\partial J^{i}}{\partial g_{j}} + \Gamma^{i}{}_{ij}J^{j} \tag{C-6}$$

where $g_i = g(\varphi_1, \Phi, \varphi_2)$ denotes the correspondence Euler angles in the EAS and should not be confused by the metric tensor. It is found that among all Christoffel symbols of the form $\Gamma^{i}{}_{ij}$ only the following terms are not zero: $\Gamma^{1}{}_{12} = \Gamma^{3}{}_{32} = 1/2\cot\Phi$. Now the final form of the divergence operator will be:

$$div(J) = \frac{\partial J^i}{\partial g_j} + (\Gamma^1{}_{12} + \Gamma^3{}_{32})J^2 = \frac{\partial J^i}{\partial g_i} + (\cot\Phi)J^2 \tag{C-7}$$

We can now place the divergence operator into the continuity equation:

$$\frac{\partial f}{\partial t} = -\frac{\partial J^i}{\partial g_j} - (\cot\Phi)J^2 \tag{C-8}$$

The final form of the continuity equation in the Euler Angle space can then be obtained by replacing the orientation flow field $J^i = fw_i$:

$$\frac{\partial f}{\partial t} = -f\frac{\partial w_i}{\partial g_i} - w_i\frac{\partial f}{\partial g_i} - f\cot\Phi w_2 \tag{C-9}$$

which represents the conservation of orientation principle in Eulerian framework.